Rock Mass Characterization Using Ground Penetrating Radar (GPR), Rotary-Percussion Drilling Performance, and Indentation Test

by

© Zijian Li

A Dissertation submitted to the School of Graduate Studies
in partial fulfillment of the requirements for the degree of

Doctor of Philosophy

Department of Process Engineering
Faculty of Engineering and Applied Science
Memorial University of Newfoundland

May 2023

St. John's Newfoundland and Labrador

Abstract

This thesis aims to develop a comprehensive rock characterization method for the rock's mechanical and Electromagnetic (EM) properties. In the mining industry's exploration and excavation stage, the rock properties' characterization plays a vital role. The precise mapping of the subsurface geometry and the characterization of the spatial lithology distribution is crucial for establishing the mining development plan.

However, several problems regarding rock characterization in both EM and mechanical scope remain to be investigated. For subsurface geology mapping, shielded mono-hole Ground Penetrating Radar (GPR) has been a helpful tool. The limitation of the borehole GPR was identified in our previous study in that the groundwater significantly impacts its signal quality. The precise GPR data interpretation depends on the detailed EM properties (especially the dielectric permittivity) characterization of the target rock formation. A rapid and economical method to obtain the dielectric permittivity of the rock is required to be developed to provide solid proof for the subsurface geology mapping through GPR data interpretation. The accuracy was verified to be satisfactory for the field trial application. The invention of a new fluid system was proposed to eliminate the groundwater problem in the borehole GPR survey, which is required to possess appropriate EM properties and the ability to replace the groundwater in the borehole during the GPR survey. For the rock mechanical properties characterization, the in-situ unconfined compressive strength (UCS) plays an important role, and its measurement has always been problematic in field operation. For the highly fractured formation, the highly developed fractures and joints system in the rock mass limit the selection of the applicable rock samples for the UCS test because there is a strict requirement on the sample size. An alternative method that lowers the sample size requirement and presents reliable UCS result needs to be investigated.

Regarding the rock EM properties characterization, A quick and economic measurement method of the dielectric permittivity was proposed, which presented acceptable accuracy, straightforward operation procedures, and low requirement of the test rock sample. A series of field tests proved the ability of the mono-hole shielded antenna to map the subsurface geometry with the borehole filled with air. The impact of the wellbore groundwater on the borehole GPR imaging quality was illustrated in detail in both theory and experiment. Then a practical solution was proposed by substituting the groundwater in the borehole with a newly developed fluid. The effectiveness of that fluid was proved through numerical simulation, lab tests, and field trials. These three innovations helped identify and remove the obstacles that hinder the application of the shielded mono-hole GPR for subsurface imaging.

A Data Acquisition System (DAQ) was developed for the rock mechanical property characterization to collect the real-time Logging While Drilling (LWD) data of the Rotary-Percussion Drilling in the mining field. An analytical model was developed to predict the in-situ UCS and gold grade of the ore formation based on the real-time LWD data, which directly reveals the spatial distribution of the lithology and provides valuable information for the gold mine excavation and development. A series of indentation laboratory tests were conducted on the NQ size rock core as an alternative lab test to the traditional UCS test. Two analytical models were developed to predict the UCS value from the indentation test result. In the indentation test, the required sample size is much smaller than the traditional method, which indicates that it is more suitable for highly fractured formation. Its sample size requirement and the experiment's Standard of Procedures (SOP) were presented, proving its feasibility in determining the rock formation's intact UCS. Then, a Discrete Element Method (DEM) simulation was carried out to elaborate the sample preparation layout and optimize the sample preparation procedure. After calibration against the lab test result, through the DEM simulation, the indentation test was optimized where the minimum required size of the rock sample was obtained. It is also proposed that the particle size of the DEM rock model is a fundamental influence parameter on the rock failure model and the stress-strain response during its compressional failure process.

Overall, this study provides practical solutions to rock characterization in EM and mechanical scopes and facilitates subsurface imaging and stability and safety evaluation.

Acknowledgements

Words cannot express my gratitude to my professor Dr. Stephen Butt. I could not have undertaken this journey without him, who generously provided knowledge and expertise. Your immense knowledge and great experience have encouraged me throughout my academic research and daily life.

This endeavor would not have been possible without my committee members, Dr. Charles Hurich and Dr. Sam Nakhla. Your invaluable patience and feedback are vital in inspiring me to form comprehensive and objective research.

I would like to extend my sincere thanks to DTL team members, who so generously took time out of their schedules to participate in my research and make this project possible. Thanks Dr. Yingjian Xiao, Dr. Hongyuan Qiu, Dr. Ramin Rafiei, Mr. Prajit Premraj, and other dear DTL members.

Additionally, this endeavor would not have been possible without the generous support from the Novamera team. I am also grateful for the opportunity of being a member of the SMD project, which granted me extensive academic knowledge and marvelous industry experience.

The most important is my gratitude to my parents. I can never repay you for your support in any form, and I will never be able to express how much I love you in any language.

Table of Contents

List of Figures

List of Tables

Nomenclature

ASTM	American Society for Testing Materials
BPM	Bond Particle Model
BTS	Brazilian Tensile Strength
BTS	Brazilian Tensile Strength
BTS	Brazilian Tensile Strength
CGS	Canadian Geotechnical Society
CMP	Common Midpoint
CoV	Coefficient of Variation
FCC	Federal Communications Commission
DE	Drilling efficiency coefficient
DEM	Distinct Element Model
DI	Drillability Index
FDTD	Finite-Difference Time-Domain
FEM	Finite Element Model
GPR	Ground Penetrating Radar
HRC	Rockwell Hardness on C- Scale
ICDD	International Centre for Diffraction Data
IHI	Indentation Hardness Index
IM	Indentation Modulus
ISRM	International Society for Rock Mechanics
LWD	Logging-While-Drilling
MLA	Mineral Liberation Analyzer
MSCL	Multiple Sensor Core Logger

MWD	Measure-While-Drilling
NDT	Non-Destructive Test
NVM	Narrow Vein Mining
OBM	Oil-Based Mud
PAH	Polycyclic Aromatic Hydrocarbons
PCA	Principal Component Analysis
PFC2D	Particle flow code in two dimensions
PI	Percussion Index
RDP	Relative Dielectric Permittivity
RES	Resolution of a dimension
RLM	Rock-Like Material
RMR	Rock Mass Rating
ROP	Rate of Penetration
RQD	Rock Quality Designation
SAGD	Steam-Assisted Gravity Drainage
SBM	Synthetic-Based Mud
SEM	Scanning Electron Microscopy
SG	Specific Gravity
SOP	Standard Operating Procedure
TBM	Tunnel Boring Machine
TEM	Transient Electromagnetic
UCS	Unconfined Compressive Strength
UWB	Ultra Wide-band
UXO	Unexploded Explosive Ordnance
WBM	Water-Based Mud

WOB	Weight on Bit
XRD	X-Ray Diffraction

1. Chapter 1: Introduction

1.1 Background

Narow veins are characterized as having widths of less than 3 meters, with the inclusion of widths of up to 6 meters in some cases (Dominy et al., 2020). Narrow vein deposits are responsible for the production of a major portion of the world's silver as well as significant quantities of gold, tin, copper, lead, and zinc. Narrow veins are a significant resource for metals all over the world; nevertheless, it is often difficult to extract metals from them due to the geologically complex character of the veins (Dominy et al., 1997). The obligation placed on the operator is to produce ore with as little dilution as possible while adhering to the parameters of economically viable production and maintaining a safe working environment. The geologist and the engineer both place a high value on their ability to accurately anticipate the orebody geometry, vein location, vein persistence, and the nature of grade distribution.

In the Sustainable Mining by Drilling (SMD), the recovery of a steeply sloping (~65 degree dipping angle from horizontal) narrow gold vein (~ 2m thick) is the primary target. Due to its high deviation angle, geometry are difficult to mine profitably for surface mining. Underground mining, on the other hand, typically requires the construction of a significant amount of subterranean infrastructure prior to the extraction of veins (Altun, 2010). This makes it difficult to mine narrow-vein, steeply sloping deposits. To develop the narrow vein in the SMD project, the development of innovative Narrow Vein Mining (NVM) procedure technologies.

The main concept of the proposed NVM development method is mining by drilling. The mining operation is broken down into two missions: the first involves drilling pilot holes and precisely charting the vein, and the second involves expanding the pilot holes to predefined diameters in order to retrieve the ore. In the beginning of the development, directional pilot hole is drilled through diamond coring drilling in the middle of the vein. The pilot hole then serves as the channel of the borehole GPR for the subsurface survey. The survey result guides the interpretation of the vein-host rock subsurface geology and the plan of the well trajectory of the next stage. In the second stage, the directional large diameter boring drilling takes place based on the downhole imaging result, in which the entire ore vein is extracted. In this type of mining, the ore vein is broken up into smaller pieces before being shipped off to be processed. All of the ore is recovered as drill cuttings, which eliminates the need to use explosives (and associated emissions) to fragment the ore and the need to crush the ore as a first step in mineral processing. Furthermore, since all of the ore is recovered using surface operations, there is no requirement for underground ventilation.

1.2 Research Motivation and objectives

The characterization of the rock properties plays a vital role in the development of the narrow vein mineral resources in the SMD project. The precise mapping of the subsurface geometry and rock EM properties characterization provide reference for the boundary determination and the well trajectory plan. On the other hand, and the characterization of the rock mechanical properties spatial distribution is crucial for establishing the mining by drilling plan.

There are still gaps, however, remaining in the rock EM and mechanical properties characterization. In the field application, the capability of the shielded mono-hole Ground Penetrating Radar (GPR) to conduct subsuface imaging in a groundwater-filled wellbore has not been widely discussed. The accuracy of the real-time acquisition of the in-situ rock mechanical properties still requires the optimization. The lab experiment to measure the rock UCS strength consumes a large amount of intact rock core sample, which is set a strict demand on the rock sample collection, especially in the mining zone with highly developed joints and fractures.

Borehole GPR is a widely used tool for subsurface imaging for archeology, hydrology, geology, and other engineering applications. Traditional, however, the omnidirectional antenna configuration is used in the survey. However, the 3D mapping of the subsurface geology is only available when the cross-borehole layout is used, which requires multiple boreholes to be drilled and higher-cost GPR surveys. This study investigates the feasibility of the shielded mono-hole GPR for the borehole survey through a series of field trials. The lithology discontinuity between the vein and the host rock was revealed in these field trials. The capability of the 1GHz shielded GPR was proved for the borehole 3D mapping with the air-filled borehole condition.

The interpretation and quantitative 3D geometry modeling of the borehole GPR result require precise determination of the rock EM properties. At the same time, the dielectric permittivity is the most crucial parameter for applying the borehole GPR among these three parameters. It is because the dielectric permittivity of the rock is directly correlated to the EM wave transmission velocity in the subsurface rock media. Thus, it accurately calculates the distance between the borehole and the lithology discontinuity reflection. The traditional method to obtain the EM wave velocity and the dielectric permittivity from GPR data requires the evident existence of a point reflector in the field for hyperbola fitting (Shihab, & Al-Nuaimy, 2005). or particular GPR unit to perform a Common Midpoint (CMP) survey (Jacob, & Urban, 2016). In the SMD project field operation, however, the point which is usually not available in the area. On the other hand, the laboratory method has a higher cost and strict demand for experiment equipment and test expertise, which is unsuitable for mining operations. In this study, an economic test method to measure the dielectric permittivity of the rock will be presented, which is not sensitive to the equipment and sample size condition and provides acceptable precision for the field application.

In the borehole GPR survey, it is discovered in our field trial in the target mining zone that the existence of groundwater in the borehole causes a significant impact on the borehole GPR data quality. The main reason is the dielectric permittivity difference between water and the rock, resulting in a rebound EM wave in the borehole. Then, the rebound of the EM wave serves as a noise, which damages the signal quality significantly, and increases the ambiguity in the GPR result interpretation. This problem limits the application of the borehole GPR on a large scale because, in most boreholes, groundwater is inevitable. Although methods like spatial filtering, time-division duplex and adaptive beamforming were proposed to mitigate the impact of the multi-path effects of the EM wave transimission, (Chang, 2011; Colone, & Lombardo, 2006 and Lazaro et al., 2014). In the field trial data, however, the amplitude of the noise induced by the groundwater overwhelms the target signal and the signal-to-noise ratio is very low. Thus, the conventional methods to eliminate the influence of the multi path effect are not applicable in this project.

This study delivers a practical solution to the poor borehole GPR data quality caused by groundwater. A new fluid recipe is developed. The new fluid stays in the bottomhole and replaces the groundwater in the wellbore during the borehole GPR survey. The new fluid enhances the borehole GPR imaging quality through reducing the rebroucing wave within the groundwater filled wellbore, because its EM properties are appropriate in this situation.

Traditional methods to measure the in-situ properties of the rock are based on borehole operations. In order to obtain an image of the cavities and cracks present in intact rock, borehole radar and auto-scanning laser systems have been deployed (Haeni et al., 2002; Liu et al., 2008). However, in order to put the measurement tools in the hole before the test, there must first be stable holes that are already present, which results in increased downtime and disturbances (Schunnesson, 1996). Besides the borehole methods, LWD techniques is widely use in the engineering of petroleum and mining operations, and it is suitable with a variety of drilling procedures. The LWD method is favored for its inexpensive cost, as well as its ability to acquire data in real time without incurring any downtime. However, the data directly collected by the LWD system is the drilling parameters (rotary speed, weight on bit, etc.), and the rock in-situ parameters need to be derived from the direct data. Thus models are established to predict the rock in-situ UCS and gold grade based on the LWD recorded drilling parameters. PCA (Principal Component Analysis) is introduced to build the prediction model of gold grade using the real-time LWD data. The result was obtained after the model training and cross-validation. The gold grade prediction model based on PCA analysis captured the trend of the gold grade and showed potential in the gold grade prediction.

The traditional method to obtain rock strength requires destructive tests on many rock samples with refined shapes, which puts a strict demand on the rock sample supplement. In practice, obtaining the rock core is expensive since core drilling is required. For the highly fractured formation, the sample preparation for the UCS test can be troublesome or impossible because the traditional UCS uniaxial test has strict requirements on the sample size. The rock cores break after the destructive test and cannot be utilized in further research. Moreover, highly developed fractures and joints in the rock mass limit the selection of the applicable rock samples for the test because there is a requirement on the size of the sample. The indentation test was introduced as an alternative lab experiment in this study. The analytic model is developed using the indentation test result to predict the UCS value, and the accuracy will be examined. The rock model will be generated and calibrated using the DEM simulation against the indentation test result. The SOP of the indentation test will be optimized by obtaining the minimum sample size required. Then the rock failure process during the indentation test will be analyzed in detail with the advantage of the DEM simulation.

1.3 Thesis Outline

This thesis consists of 9 chapters. Chapter 1 Introduces the background and motivation of this study. It introduces the requirement of the mining industry fieldwork requirement and illustrates the necessity of improving the rock characterization for both EM and mechanical properties.

Chapter 2 presents a comprehensive literature review of rock characterization for EM and mechanical properties. The literature review is divided into five parts corresponding to the following five manuscripts. The area of the literature review covers the application of GPR for subsurface imaging, the measurement and the utilization of the material dielectric permittivity in multidisciplinary research, the impact of groundwater on the borehole GPR data quality, the determination of the rock in-situ properties through rotary-percussion drilling logging data, and the rock mechanical properties prediction through the indentation test.

Chapter 3 presents supplement methodologies information which were not detailed given in each manuscript. This thesis consists of 5 manuscripts, from Chapter 4 to Chapter 8.

Chapter 4 proposed a new rock dielectric permittivity measurement method based on GPR reflection. This method is specifically designed for the NQ size rock core, which is the standard rock core size in Canada. This method is straightforward, practical for field work, and provides acceptable accuracy. The dielectric permittivity of host rock (mafic) and the ore (quartz) were measured using this method. By comparing to the literature result, the accuracy was verified. Through FDTD simulation, recommendations for the experiment design optimization were presented.

Chapter 5 presented a series of field trials where the shielded 1GHz GPR was used for borehole imaging. The downhole survey obtained the boundary between the quartz and mafic, and the directional ability of the GPR system was proven.

Chapter 6 discussed the impact of groundwater on the borehole GPR imaging and the development of the recipe of the new imaging fluid. This imaging fluid possesses appropriate EM properties for the borehole GPR and aimed to replace the groundwater in the borehole during the survey. The EM properties of the imaging fluid was measured and its ability to enhance the borehole GPR survey signal quality was validated through lab tests and field trials.

Chapter 7 presents an attempt to predict the in-situ strength and the gold grade of the rock using the real-time drilling performance data. Analytical models were developed to correlate the drilling performance data and the ROP, in-situ stress and the gold grade.

Chapter 8 discusses the indentation test as a method to estimate the strength of the rock. A series of lab tests were conducted, and analytical models were built to predict UCS from the indentation test results. Recommendations were made on the sample preparation procedures. DEM simulations were conducted, and the ball size was suggested to be vital in the rock model calibration for rock crush failure tests.

Chapter 9 summarized the conclusion and highlights of each manuscript and proposed further recommendations.

1.4 Research Contribution Summary

In the study of the rock EM and mechanical properties characterization, the research work of this thesis attempts to make a contribution by considering these elements:

1. This dissertation studies rock characterization of EM properties and mechanical properties to help the SMD project.
2. The availability of a mono-borehole GPR system to conduct directional imaging of subsurface targets is verified.
3. A practical and economical method to estimate the EM wave velocity and the RDP of the NQ size rock core is proposed.
4. An imaging fluid is developed to mitigate groundwater's impact on the borehole GPR signal quality.
5. Models are developed to predict the in-situ strength and the gold grade of the mining field using the rotary-percussion drilling performance data
6. Correlations are presented in order to predict UCS and disk cutter drilling efficiency through IT results. The optimum sample preparation procedures were put forward.

Chapter 2: Literature Review

2.1 Application of GPR for subsurface structure imaging

GPR is widely used in the survey of transportation infrastructure since it is a Non-Destructive Test (NDT) method. Several international organizations have released guidelines on how to employ GPR in transportation infrastructure appropriately. The equipment and field procedures for GPR subsurface exploration and processing techniques used to interpret GPR data are summarized in a standard guide, ASTM D6432-19, which was created by the American Society for Testing and Materials (ASTM, 2019). Osumi and Ueno (1988) presented the imaging of buried objects with high azimuth and range resolution using a wideband microwave holographic technique. Kovacs and Morey (1983) valuated the efficiency of detecting cavities under the concrete pavement using a dual antenna layout GPR system. Maser et al. (1991) measured the thicknesses of highway asphalt layer using surface GPR, and the accuracy of the asphalt thickness measurement was ±7.6mm.

In the environmental and geology area, Lunt et al. (2005) used 100 MHz surface GPR antennas, GPR reflection travel time data were utilized to monitor soil water content over broad regions and under varying hydrological circumstances. Neal and Roberts (2000) proposed that GPR can precisely image the stratigraphy and internal sedimentary structure of UK coastal barriers, spits, and strand plains above and below a fresh groundwater table. Beres (1995) utilized three-dimensional (3D) GPR to establish the boundaries between various sedimentary facies, the height of the ground water table, and the major flow direction of the ancient, braided river system.

Borehole GPR, a specific GPR operation mode, can discover and analyze deeper geological features with high resolution due to two critical qualities. First, its antennae are situated in a borehole that may be close to or rather deep to the objectives. Second, the detection reduces the impact of the conductive near-surface weathering layer. The conventional borehole GPR’s transmitter and receiver are both omnidirectional. As a result, only the depth and radial distance from the drill may be measured for geological targets. Because the azimuth of the target is unclear, multiborehole measurements or other data are necessary for 3-D interpretation. To remedy this issue, directional BR technology was developed (Liu and Sato, 2006).

Van Dongen et al. (2002) designed a directional GPR system with an electric dipole and a curved reflective shield. The antenna radiation pattern and the three-dimensional imaging method was presented. Van Waard et al. (2004) performed laboratory and field tests using the impulse directional borehole radar to detect Unexploded Explosive Ordnance (UXO). Sato and Takayama (2007) employed borehole radar for subsurface measurements in a vertical granite borehole and estimated the subsurface fracture azimuth orientations. Liu et al. (2019) proposed a direction-of-arrival (DOA) estimation algorithm based on linear prediction and a 3D imaging algorithm for the directional borehole GPR and verified its real-time processing capability using the fracture model simulation data. Borchert et al. (2009) developed a directional GPR system which has three separate receiver antenna and three separate A/D converter, which enables parallel signal recording of three channels. Ebihara et al. (2010) introduced a directional borehole GPR system based on the e coaxial-fed circular dipole antenna. Wang et al. (2021) proposed Root-MUSIC algorithm to enhance the accuracy of the directional borehole radar consists of one transmitting antenna in and four receiving antennas distributed at equal angles in a ring.

In the previous study on the directional borehole GPR, the directionality is usually achieved by the setup of multiple receiver antennae. The signal is generally below 200MHz to ensure a large penetration depth. In this study, the application of directional shield is used for the directional survey, which has a simpler system layout and fits better in small diameter borehole survey.

2.2 Rock dielectric permittivity and EM wave velocity

Several fields are interested in measuring the dielectric permittivity of the mineral matrix in granular solids. In civil engineering, Robert (1998) developed a dielectric measurement device between 50 MHz and 1 GHz. The dielectric permittivity of concrete aggregate is determined as a function of hydration level and chloride content.

For geophysical and hydrological applications, Bano (2004) estimated the water content and detected the dry aeolian-dune boundary based on the dielectric permittivity characterization. Monnier and Kinnard (2013) used the GPR survey to evaluate the variation of EM waves in the subsurface, and proved the degradation of the rock glacier permafrost. West et al. (2007) presented a method for measuring the dielectric properties of ice cores from a temperate glacier to quantitatively study the effect of intercrystalline unfrozen water and air content on the dielectric permittivity of ice.

In remote sensing, Jiang and Wu (2004) developed an empirical ice permittivity model to identify ice and liquid water in ground and space remote sensing. Guo et al. (2019) used numerical experiments to calculate the dielectric permittivity of materials with different microgeometries and varying amounts of internal interfaces to improve the accuracy of fluid-saturated rock surveys.

For the study of lithology and geology, Robinson and Friedman (2003) presented an experimental method for measuring the permittivity of rock. The method treated the rock as a porous medium and measured the different permittivities of the rock immersed in fluids. The dielectric permittivity of the rock was then calculated by interpolation. Bobrov et al. (2015) studied the variation of the complex relative permittivity of the quartz powder with different water saturation. Seleznev et al. (2019) presented a method to estimate the porosity of water-filled rocks based on permittivity measurements. Morte and Hascakir (2019) applied the mixing rules

The measurement of the EM wave velocity, and thus the permittivity of the formation rock, plays a critical role in several GPR signal processing operations, such as proper amplitude restoration (gain), depth conversion, and subsurface material characterization. (Forte et al., 2014). When calculating the wave velocity from the GPR field survey data, the determination of the dielectric permittivity would be a feasible solution.

In the field application of GPR, the velocity and Relative Dielectric Permittivity (RDP) of the rock media are typically determined by a CMP survey. Jacob & Hermance (2004) evaluated and compared the accuracy of the CMP method and the hyperbola fit under different field conditions. Nakashima et al. (2001) analyzed the effect of GPR signal quality enhancement using the CMP method and predicted the groundwater level using multiple reflectors. Hyperbola fitting analysis is another commonly used method for EM wave velocity prediction. Dou et al. (2016) introduced a real-time hyperbola detection and fitting method for GPR data processing by applying the novel clustering algorithm C3 in the machine learning algorithm.

However, the CMP and hyperbola fitting methods require specific requirements in terms of equipment and geometry. The CMP method requires a specific layout of the GPR antenna, which places requirements on the borehole geometry and the GPR equipment. Forte and Pipan (2017) reviewed the application of multi-offset GPR. They suggested that coherent noise suppression and velocity analysis are critical features in the GPR field applications. When using the hyperbola fitting, it is necessary to identify circular reflectors from the field geometry at certain depths. He et al. (2009) reviewed the background and development of rebar detection in concrete using GPR, where the hyperbola fitting method serves as the foundation. The developments of polarization in rebar detection, diameter detection, corrosion detection, and other automatic methods are also discussed.

In addition, the CMP and hyperbola fitting methods are not suitable for accurate determination of EM wave velocity and RDP for certain depth ranges. These two methods calculate the average velocity and RDP at a certain depth range. Several high quality geological reflectors at different depths are required for accurate regional velocity and RDP measurements. Based on previous field trial experience, the high quality reflectors for these two methods are not available in the exploration zone. The limited space in the borehole also limited the application of the CMP method. Therefore, the development of a new method to measure the velocity and RDP of the rock is important for mine recovery. The YAKUMO array GPR system was reported to successfully detect the discontinuities (Kikuta et al., 2019). This approximation is generally realistic in the case of a homogeneous environment, such as a granitic block or salt formation. However, it provides only a rough estimate for multilayered terrains with variable porosity or lithology changes.

Previous research has discussed the laboratory method for EM velocity and RDP measurements. Numerous techniques have been applied, including the transmission/reflection (T/R) method, the open-ended coaxial line method, the free space method, and the resonant cavity perturbation (RCP) method. Waldron (1960) introduced the perturbation formula considering the frequency shift as the basis for laboratory measurement of the dielectric permittivity of a material.

Based on the conventional RCP method, Sheen (2007) introduced the calibration considering the quality factor increase due to the introduction of the lossless dielectric sample. The corrected formula was developed and the accuracy of the result was improved. Ghodgaonkar et al. (1989) developed free-space measurement equipment, a pair of spot-focusing horn lens antennas, a network analyzer, and a computer for measuring the dielectric permittivity of solid materials. Nicolson and Ross (1993) presented a method for measuring the complex permittivity of homogeneous materials. The sample is placed in a microwave transient electromagnetic (TEM) device and excited. Baker-Jarvis et al. (1990) proposed an improved technique for measuring the RDP of solid materials based on the transmission/reflection method, taking into account the effect of poor frequency-sample length coupling. Klein et al. (1993) presented a standard test method for measuring the permittivity of various materials with arbitrary conductivity based on the RCP theory. Zheng et al. (2005) presented an improved method for RDP measurement based on Lichtenecker's mixture formulas and RCP theory, but modified with polyethylene dilution. This new method is suitable for dry rock measurement and has high accuracy and low sample requirement. Leão et al. (2015) used the RCP theory based on Lichtenecker's mixture model and measured the effective permittivity of soils at 50 MHz frequency.

In summary, among the field methods, hyperbola fitting requires a point shape reflector in the target subsurface region (Dou, 2016), and the CMP method is carried out through a special borehole GPR array (Jacob & Hermance, 2004). However, in the field practice of the SMD project, the appropriate point shape reflector has not been identified, and the borehole geometry and production plan do not support the GPR design for CMP. Therefore, the traditional field method of hyperbola fitting and the CMP method are not suitable for the SMD project.

Among the laboratory methods, the equipment for the RCP method is often customized for a small number of materials (within a certain range of EM properties and sample size) (Chen et al., 2004 and Costa et al., 2017). For the T/R based methods, the sample condition requirement is strict and the test result is sensitive to sample preparation and equipment (Von Hippel, 1958; Chen et al., 2004 and García-Baños et al., 2005). Thus, this approach can be impractical and expensive for the mining project where a large number of rock samples need to be tested and the EM properties change with depth and lithology variation.

To meet the need of rock EM properties characterization, this study presents a more practical method with low equipment and sample requirements based on the T/R method using a small-scale surface GPR unit. This method is designed for the measurement of NQ size core and suitable for the measurement of large amount of sample. The accuracy is not as high as the laboratory methods, but acceptable for the requirement of the project.

2.3 The borehole GPR signal quality problem and the impact of groundwater

It is essential to have knowledge of the spatio-temporal variation of subsurface features and processes in order to provide answers to various topics such as geological, environmental, civil and mining engineering. Borehole GPR has been identified as one of the most promising tools among the potential methods that could be used to obtain information from specific depths. This is due to the fact that it allows extended imaging of the features and structures surrounding the boreholes when they are at the desired depth. Huisman et al (2003) presented an overview of the application of borehole GPR to determine soil water content.

Thus, borehole GPR has become a practical tool for oil and gas engineering. Miorali et al. (2011) proposed that borehole GPR can be used as a permanent sensor for the applied oilfield Steam-Assisted Gravity Drainage (SAGD). Based on laboratory experiments, Oloumi et al. (2015) introduced that ultra-wideband (UWB) borehole GPR can be used for oil production well perforation.

In environmental and engineering, Binley et al. (2002) used borehole GPR to predict the transfer of agricultural contaminants through the vadose zone based on the correlation between groundwater saturation and soil dielectric permittivity. Robinson et al. (2008) suggested that geophysics could contribute to the development of hydrology in the theme of synergistically advancing process-based watershed research by using electrical and magnetic methods to measure geological structure and identify flow paths. Hiscock and Bense (2021) introduced how borehole GPR can help develop hydrology, groundwater distribution, and water pollution.

In the application of geological and mining exploration technologies, Trickett et al. (2000) reported the application of borehole GPR to image the gold reef in the deep mining environment with a penetration depth of 95 m and a resolution within 1 m using a 60 MHz antenna. Francke (2012) reviewed the progress of commercialized GPR applications in surface mineral resource evaluation and technological advances, such as flexible collinear antennas and the integration of live differential GPS positioning. Davis and Annan (1989) reviewed the application of GPR in bedrock mapping, fracture and lithological discontinuities, and groundwater contamination detection. Neal (2004) presented that understanding GPR theory and GPR data post-processing and interpretation methods is important for its field application. He reviewed the current limitations of GPR data quality enhancement.

Although there is a wide range of borehole GPR applications, its ability to image the target features is limited by several conditions. While technical antenna settings, such as center frequency and antenna configurations, determine the ability to resolve the subsurface, the signal response and penetration depth were further affected by environmental conditions, such as water and clay content, texture, and rock density. Tosti et al. (2013) presented an application of GPR to evaluate clay content in subasphalt compacted soils. GPR units with different frequency ranges were used and compared, and the results were promising for detecting clay content, which affects the bearing capacity of sub-asphalt layers. Grote et al. (2010) reported the application of GPR to determine the spatial distribution of soil water content based on its relationship with sampling depth, season, vegetation, and soil texture. The data quality of different antenna center frequencies is compared.

Among the variables that can affect the GPR signal, the effect of fluids inside and outside the borehole is one of the most prominent characteristics affecting image quality. According to Jol (2008), water is generally considered to attenuate GPR wave propagation due to its high RDP. According to Cassidy (2007), the increased conductivity of water causes a higher attenuation of the EM wave energy. Then, the spatial/temporal variation in GPR signal attenuation can be used to interpret the potential contaminated area hydrological interpretations and evaluate the contaminant properties, saturation index and biodegradation processes. Thus, the high RDP and conductivity of the groundwater are the two main reasons for its impact on the borehole GPR imaging quality.

According to Vogt (2004), who investigated the impact of conductive groundwater on the accuracy of borehole GPR imaging, the distance between the antenna and the borehole should be reduced to reduce the influence of water. Huo et al. (2018) reported the problem of groundwater in the wellbore on borehole GPR, and proposed three effective signal processing methods to suppress the reflected guided waves (RGWs). The noise detected in this research is not the same as in our study. The reason is expected to be that the GPR frequency is much lower than ours.

In the drilling engineering, the drilling fluid (mud) is generally categorized as Water-Based Mud (WBM) and Oil-Based Mud (OBM). Parizad & Shahbazi (2016) modified the EM properties of the WBM using SnO2 nanoparticles and KCl salt.

Patil et al. experimentally measured and summarized the relationship between the EM properties (electrical resistivity and dielectric permittivity) of OBM and influence parameters (frequency, temperature, oil and salt content and oil/water ratio). Jannin et al. (2014) proposed that the OBM complex permittivity has on two main influence factors: brine volumetric fraction and weighting material volumetric fraction. Both the electrical conductivity and the dielectric permittivity of the WBM are significantly higher than what is required for compatibility with borehole GPR. The traditional OBM has an adequate dielectric permittivity and a lower electrical conductivity than WBM; nevertheless, due to regulatory restrictions, its application in subsurface imaging is limited because of the toxicity of its additives. Because the newly produced imaging fluid has characteristics such as acceptable adequate dielectric permittivity, low conductivity, and very low toxicity, it is now possible to use it for a wide variety of applications in field surveys.

2.4 Determination of the formation properties from LWD measured rotary percussion drilling data

Laboratory tests are one of the most accurate methods for rock characterization; despite that, it is time-consuming and cost-consuming. The laboratory tests, however, only give a rough idea about the rock mass properties in the field if the rock samples are not collected from a relatively large area or too few. Hoek (1977) reviewed the result of rock mechanical laboratory tests, such as UCS and shear strength. Also, empirical methods are applied in rock characterization. Rock Quality Designation (RQD) (Deere, 1988), Rock Mass Rating (RMR) (Bieniawski, 1988), and Q system (Barton and Lien, 1974) are indirect parameters for rock classification obtained from the rock mechanical properties. These methods are relatively reliable and have gained popularity for decades. However, they cannot present in-situ rock properties but only a general assessment.

Several borehole-based methods have been developed to investigate rock's in-situ properties. Borehole radar and auto-scanning laser systems have been utilized to image the cavities and fractures in intact rock (Haeni et al., 2002; Liu et al., 2008). However, existing stable holes are needed to put the measuring tools in the hole before the test, which leads to higher downtime and disturbances (Schunnesson, 1996).

MWD and LWD techniques were introduced into mining engineering in open pit bench drilling in the 1970s (Segui and Higgins, 2002). It has been widely used in petroleum and mining engineering and is compatible with different drilling techniques. The LWD technique is favored for its low cost and real-time data acquisition with no downtime. However, the operators, rig control systems, bit wear, measurement errors, and other factors also influence the data. Thus, the influence of the system factors should be removed to make the rock properties independent in the data analysis (Schunnesson, 1996). Several approaches have been tested, including theoretical models for rock drilling, statistical methods, and, more recently, advanced data processing tools.

PCA (Principal Component Analysis) is a dimension reduction technique used in statistics and machine learning. It takes a set of variables that are correlated and transforms them into a set of variables that are linearly uncorrelated. These variables, called principal components, capture most of the variance that was present in the original data. This method helps find patterns in the data, reduces noise, and simplifies the data set for further analysis or modeling. Visualization, feature extraction, and noise reduction are typical applications of PCA (Jolliffe & Cadima, 2016; Metsalu & Vilo, 2015).

In this study, empirical models to predict the rock in-situ properties (UCS and gold grade) was developed based on the direct measured rotary percussion drilling parameters of the LWD system. These models provided a time and cost economic method to increase the efficiency of the rock in-situ properties.

2.5 Rock mechanical characterization through indentation test

Predicting the mechanical properties of the rock from drilling rates would help engineers control changing formation characteristics. These Mechanical properties of the rock, such as UCS, significantly impact the design of rock engineering projects, as Santarelli et al. (1996) suggested. Mateus et al. (2007) proposed that UCS is usually considered one of the most critical parameters in the wellbore stability evaluation. Singh et al. (2012) summarized that there are two standard experiment procedures established to measure the UCS developed by ASTM (American Society for Testing materials) (2013) and ISRM (International Society of Rock mechanics) (2018). Kahraman et al. (2000) reported that the drillability index, which is similar to the indentation index, can be used to estimate the ROP of the roller cone bit.

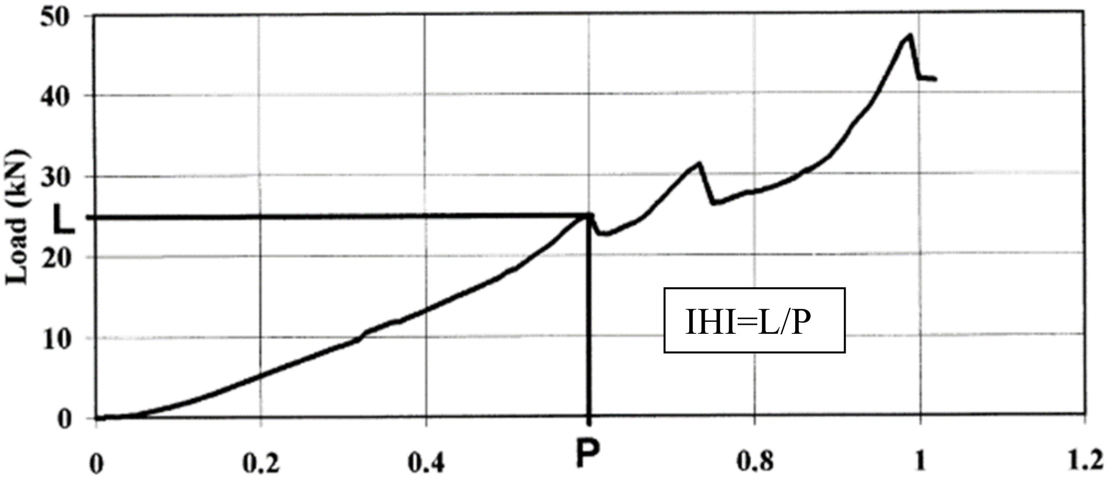

Figure 2-1 The indentation hardness index (IHI) calculation (Szwedziki, 1998). L represents the load (kN) and P represents the Displacement (mm). The IHI is calculated as the slope of the Load-Displacement curve

Swain and Lawn (1976) added that rocks are complex structures and are opaque, so any test on them is restricted to before and after external visualization studies. It is reported that the indentation test result of rock is related to the drilling property and crushing behavior. The indentation hardness test is an indirect method and can be used to correlate with the unconfined compressive strength as they have a linear relationship for specific rock types from the previous studies and experimental work carried out by Szwedziki et al. (1998). Kahraman et al. (2012) investigated the relationship between indentation–load curve and rock properties to develop prediction models for drilling. A standard IHI test was suggested by Szwedzicki (1998) that predicted UCS from the IHI.

$$UCS = 3.1\, IHI^{1.09} \tag{2-1}$$

Where, UCS is the unconfined compression strength in MPa; IHI is the Indentation Hardness Index from Indentation tests in kN/mm. IHI is defined as the slope of the Load/Penetration curve between the starting point and the max load point.

In addition to the IHI, another parameter: Drillability Index (DI), can also be obtained from the

Figure 2-2 Indentation testing using metal indenter on the point load apparatus (Kahraman et al., 2012)

indentation test (Kahraman et al., 2000). The DI calculation is different from the IHI: it is the slope at the 0.5 peak load on the Load/Displacement curve.

Kahraman et al. (2000) summarized the ROP prediction equations for conical and spherical bit tooth, respectively.

For conical bit-tooth,

$$ROP = 3.02\frac{NW}{\alpha D} \tag{2-2}$$

For spherical bit-tooth,

$$ROP = 3.35\frac{NW}{\alpha D} \tag{2-3}$$

Where, ROP is the penetration rate (m/h); N is the rotational speed (rpm); W is the thrust (kN); α is the drillability index (kN/mm), and D is the bit diameter (cm).

The procedure for the indentation test involves using a servo-controlled loading frame. This system can provide a load on the rock sample with a metal indenter attached to it with an apex angle of 60 degrees and a 5mm tip diameter. The indenter's tip diameter played a role as the larger diameters gave a higher indentation index. In comparison, the smaller diameters gave a comparatively lower value of the indentation index, according to Haftani et al. (2015). It is suggested by Kahraman et al. (2012) that the Indentation index of moderately complex rocks was in the range of 20-30 kN/mm, while harder rocks have a range from 40-50kN/mm in their IHI. The equation has a coefficient raised as a power to the indentation hardness index. This term is defined as the Indentation Test (IT) coefficient in this study.

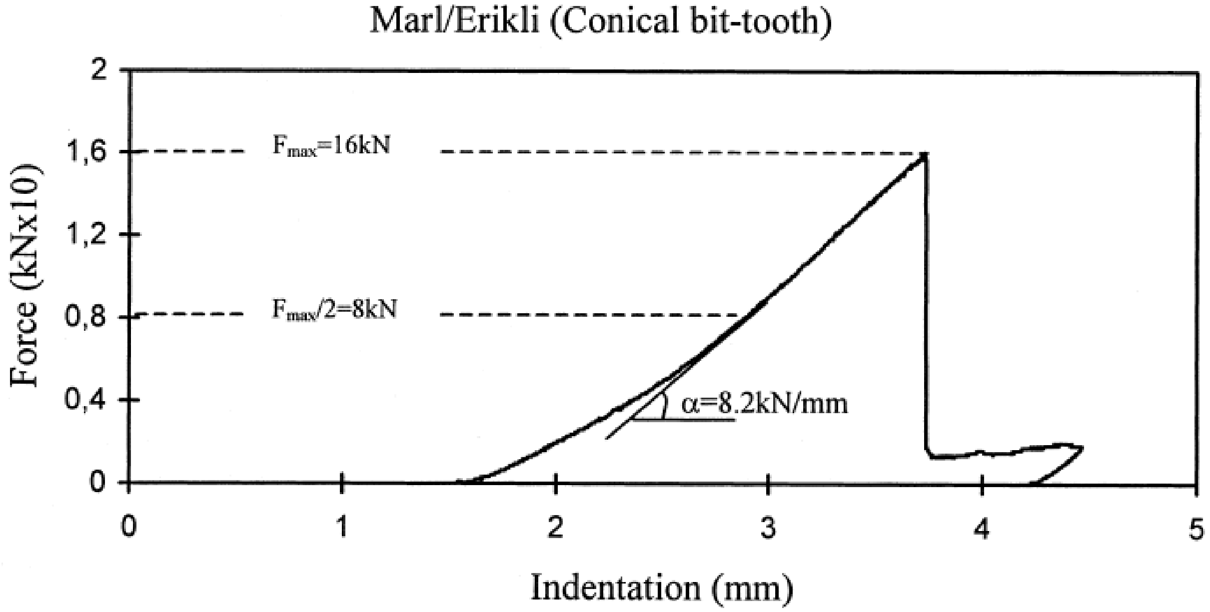

Figure 2-3 Calculation of the drillability index (DI) (Kahraman et al., 2000)

Figure 2-3 shows α is the apex angle, and R is the tip radius. The effect of the geometry of the indenter was studied by Thiercelin and Cook (1988) and Uboldi et al. (1999), and it turned out to be unneglectable because it influences the rock failure mechanisms and rock stress-strain responses. Huang et al. (1998) concluded experimentally that shear failure happens for smaller depths, and tensile failure occurs for higher penetration depths in the indented rock samples.

Mechanical excavation in the drilling process is done in two ways, i.e., shearing on soft to medium formations and indentation on medium to complex formations. Indenters break rock by applying force normal to the rock surface. In comparison, drag bits apply force parallel to the rock surface. Thus, roller cones, disc cutters, and percussion tools break rocks by indentation. Tan et al. (1998) reported that a crushed one is formed below the indenter-rock contact surface, the elastic deformation zone. The micro-cracks are generated and propagated into the deeper rock in this zone.

In addition to the laboratory experiment, the Finite Element Method (FEM) was also utilized in the rock indentation study, as studied by Carpinteri and Invernizzi (2005), Huang and Detournay (2013), and Paluszny et al. (2014). In addition to the FEM simulation, the Discrete Element Method (DEM) explores the fundamental failure processes that emerge from the rock indentation and the effective factors that influence failure mode. Zhang et al. (2018) applied the PFC2D software to analyze the influence of rock joint angle and rock strength on the fracture propagation pattern induced by rock indentation. Using PFC, Zhu et al. (2017) simulated UCS and Brazilian Tensile Strength (BTS) tests on the numerical rock model. By considering the rock indentation process and crack propagation with the pressured boundary condition, the micro-properties of the rock model are calibrated to match the macro-properties of the rock specimens. Li et al. (2016) conducted the indentation test of a Tunnel Boring Machine (TBM) wedge indenters on rock using PFC2D to analyze the fragmentation efficiency and penetration rate under different cases. The clustered assembly approach is introduced to simulate the grain-based brittle rock.

In the previous IT research, the sample preparation method has not been standardized, since each scholar uses his own sample preparation procedures. There are also several different forms of empirical models developed to predict UCS from IT result, which is obtained with different sample preparation and test procedures. In this study, the result of different sample preparation methods is evaluated and the optimized SOP is suggested. New model is proposed based on the recommended IT test SOP. In the DEM simulation, the influence of the particle size of the rock model on the rock IT test result is evaluated, which was not fully discussed.

Chapter 3: Methodologies

3.1 GPR subsurface imaging

The GPR unit Noggin 1000 MHz from Sensors & Software was used in this field trial. A 3D-printed housing covered the antenna. The gaps on the housing were sealed with silicon glue for waterproofing, as shown in Figure 5-4. PVC pipes were attached to the case using thread to adjust and maintain the tool face angle of the antenna. The other end of the cable is connected to a winch for the up-and-down travel of the antenna. A PVC pipe was hoisted on a wood shelf to guide the travel of the GPR antenna (Figure 3-1).

Two vertical holes were drilled in the test location. One hole was drilled with an offset of 1.8 from the hanging wall outcrop; the other was drilled right in the middle of the vein. The angle of the vein dip is approximately 70° (20° deviation from vertical). The coordination of hole #2 is (49.971807, -56.135571) or (295075.43, 5537166.21). The hole #1 coordination is (49.971803, -56.135502) or (295080.37E, 5537165.75N). The ROP and cutting logging data of two holes were given in Table 3-1 and Table 3-2.

Figure 3-1 Wood shelf for the GPR cable hoisting

Table 3-1 Hole #1 ROP and cutting analysis

Hole #1 ROP and cutting logging data						
Start Depth (m)	**End Depth(m)**	**Length (m)**	**time (s)**	**ROP (m/hour)**	**Comment**	**Comment**
0	1	1	72	50.00	Potential Hanging wall with High ROP	Large yellow mafic
1	2	1	120	30.00		Yellow and green mafic, very few quartz grains
2	3	1	142	25.35		Yellow and green mafic, very few quartz grains
3	4	1	179	20.11		Yellow and green mafic, a few quartz grains
4	5	1	115	31.30		Yellow and green mafic, large quartz grain start to be observed
5	6.25	1.25	150	30.00		Yellow mafic content decreases, green mafic content increases, quartz content decreases
6.25	7	0.75	234	11.54	Potential Vein with low ROP	Same as the above interval
7	7.5	0.5	144	12.50		Few yellow mafic and green mafic content increases, but quartz content does not change.
7.5	8	0.5	148	12.16		
8	8.5	0.5	187	9.63		Same as the above interval
8.5	9	0.5	234	7.69		
9	9.5	0.5	201	8.96		Mostly green mafic, few yellow mafic, quartz content decreases
9.5	10	0.5	420	4.29		
10	11	1	544	6.62		Same as the above interval

Table 3-2 Hole #2 ROP and cutting analysis

Hole #2 ROP and cutting logging data					
Start Depth (m)	**End Depth(m)**	**Length (m)**	**time (s)**	**ROP (m/hour)**	**Comment**
0	1	1	88	40.91	High clay content, high yellow mafic content, low quartz content
1	2	1	102	35.29	Clay content decrease, high yellow mafic content, low quartz content
2	3	1	165	21.82	Nearly pure quartz
3	3.5	0.5	70	25.71	Majority Quartz, some yellow mafic
3.5	4	0.5	124	14.52	
4	4.5	0.5	32	56.25	Half quartz, half yellow mafic
4.5	5	0.5	93	19.35	
5	5.8	0.8	176	16.36	Majority green mafic, some Quartz
5.8	6.8	1	141	25.53	Majority green mafic, some Quartz
6.8	7.8	1	214	16.82	Majority green mafic, very low Quartz
7.8	8.8	1	435	8.28	Majority green mafic, very low Quartz
8.8	9.8	1	748	4.81	Majority green mafic , very low Quartz

3.2 Quantitative mineral content determination through XRD and MLA tests.

The Mineral Liberation Analyzer (MLA) could automatically conduct mineralogy data acquisition equipment with a Scanning Electron Microscope (SEM) and an Energy dispersive X-ray (EDX) spectrometer (Gu, 2003). Back-Scattered Electron (BSE) technology is the basis of the MLA to obtain the

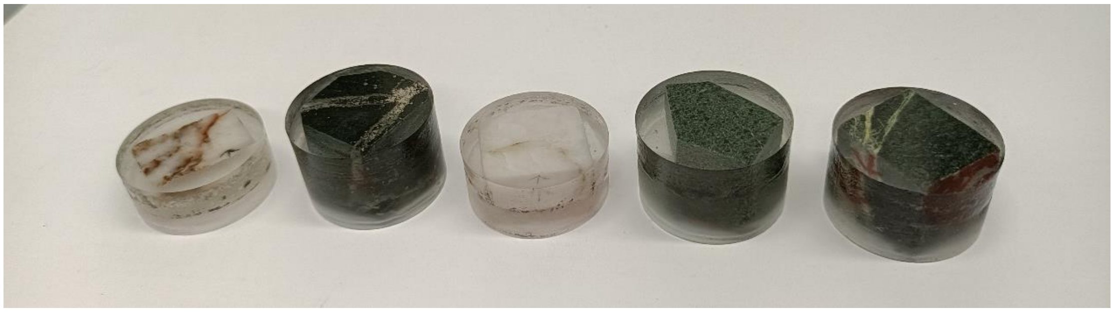

Figure 3-2 MLA rock sample prepared in the epoxy

image of the grain boundary and the discrimination of mineral contents. The minerals are then classified by comparing their characteristic X-ray spectra to the reference data (Sylvester, 2012).

The rock samples were small rock blocks cut from the rock core obtained from the field, containing the mafic (host rock) and quartz (ore). The samples were put in the plastic molds epoxy was filled in the mold. After an overnight curing time, the samples were polished to remove the epoxy on the rock sample and to make the sample surface smooth. Before the MLA test, the polished samples were coated with evaporated carbon which is conductive. (Povey-White, 2021). It is because that SEM requires the transfer of electrons between a sample and the microscope itself to avoid the rock sample water content evaporation (Goldstein, 1982). Mineral liberation analysis was conducted with an FEI MLA™ 650 field emission gun

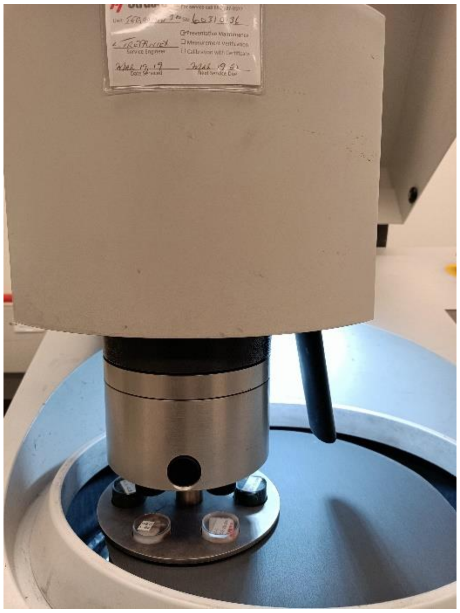

Figure 3-3 MLA sample on the polishing machine

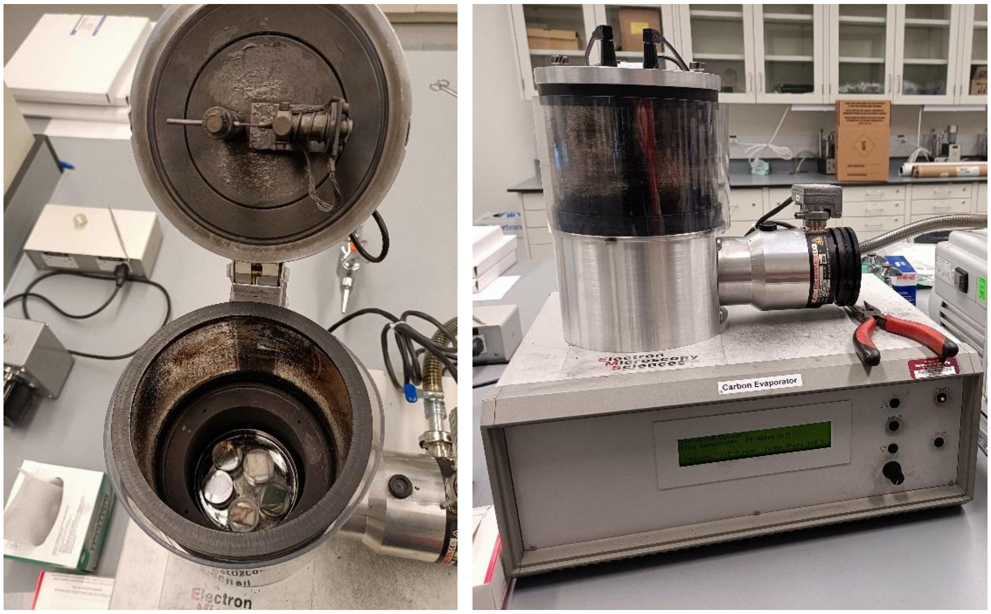

Figure 3-5 Carbon evaporator for the MLA sample carbon coating

(FEG) SEM with a voltage of 15 kV, spot size of 5.32, and a horizontal field width of 1 mm at a working distance of 13.5 mm and beam current of 10 nA. The software used wasMLA™3.1.4.683 (Grant, 2018).

Figure 3-4 Equipment for XRD sample crushing

Figure 3-6 Rigaku Ultima IV x-ray diffractometer for XRD test

X-ray diffraction analysis (XRD) is an NDT for identifying a material's crystallographic structure, primarily at the atomic or molecular level. A material is exposed to incoming X-rays in the process of XRD, and the intensity and scattering angles of the X-rays that escape the material are then measured. In recent years, XRD has gradually become one of the most widely used analytical techniques for rock samples' qualitative and quantitative characterization (Zhou et al., 2018).

This research measured the mineral content of the mafic (host rock) and quartz (ore) samples through XRD. The sample was cut from the rock core at the depth of interest, then crushed by the laboratory pulverizer. The laboratory pulverizer has four parts: the puck mill, the tungsten carbide grinding bowl, and the vibratory ring. The rock sample were crushed into powder. Then, the powder was used for the XRD test using the Rigaku Ultima IV x-ray diffractometer with a copper x-ray source and a scintillation counter detector. The XRD result was analyzed using JADE 2010 software (pattern processing, identification, and quantification) and the International Centre for Diffraction Data (ICDD) PDF2 powder diffraction databases.

3.3 Fabrication and test of the imaging fluid

The imaging fluid consists of three gradients: canola oil, API standard barite powder, and stearic acid. In 1974, the first canola oil was produced in Canada. Erucic acid and glucosinolate concentrations in rapeseed oil were reduced due to genetic changes. Canola oil biodiesel offers great performance attributes and contributes to an estimated 30% of the increasing global biodiesel market. Canola oil is a valuable and renewable raw material used to produce various industrial products (Wrigley et al., 2015). Because of its advantages of low conductivity, appropriate Relative Dielectric Permittivity (RDP), and low toxicity, canola oil is chosen as the fluid base of the imaging fluid.

Barite is the mineral form of barium sulfate ($BaSO_4$) that naturally exists. Its key characteristics are high specific gravity (4.5), very low solubility, non-toxicity, and chemical and physical inertness. The specific gravity of typical barite is generally between 4.1 and 4.2. Barite is mined underground or on the surface, then processed to obtain the correct size product and eliminate any undesirable contaminants. In this study, barite is applied to increase the density of the imaging fluid so that the imaging fluid can settle under groundwater.

Stearic acid is a member of the saturated fatty acid family, utilized as an excipient in several medicinal formulations. It is redeemed as a non-toxic and economical oil hardener. (Di Meo, 2019). Stearic acid is widely used to manufacture detergents and cosmetics products because it has a polar head group that can bond with metal cations, and a nonpolar chain provides solubility in organic solvents (Zhen et al., 2015). The molecular formula of the stearic acid is $CH_3(CH_2)_{16}COOH$, and its melting point is 70.8°C (Pan et al., 2013). The high melting point (higher than normal room temperature) is the main reason the stearic acid increases the viscosity of the imaging fluid at normal temperature and prevents the separation of the liquid and solid phases.

The optimum recipe of the imaging fluid is as follows: Canola oil: API barite powder: stearic acid =18: 9.1: 1 (by weight). The equipment of the imaging fluid is as follows: high-speed mixer, fluid container, mass weight, scoop (to take the material sample), a heating device (temperature controlling stove), oven gloves, thermometer, conductivity meter, and graduated cylinder.

The SOP for the imaging fluid manufacturing in the lab is given below:

1. Weight the material. The ideal receipt is: For 1L imaging fluid, there is 769g (0.854L) canola oil, 388g Barite, and 42.7g stearic acid. The SG of the mixture is 1.2.
2. Melt the stearic acid. Heat 20% of the canola oil with the stearic acid up to 100 degrees Celsius until the stearic acid melts.
3. Mixing cold oil and hot oil: Put the rest 80% room temperature oil in the metal container. Then add the hot oil and stearic acid mixture to the metal container. Mix the oil on the high-speed mixer until the oil is clear without any wax.
4. Mixing the barite: add barite into the metal container. The barite should be added using a sieve to slow down the process and to separate the barite powder. Mix the imaging fluid during the adding procedure.

Figure 3-7 Triple spindle stainless-steel high-speed mixer

5. Continue the mixing for at least 10 minutes.

After the mixing, the imaging fluid can be stored in a container at room temperature. Before using the imaging fluid (after a storage period), the imaging fluid should be stirred again for 10 minutes. By comparing these samples in Figure 3-8, it is found that the optimum recipe has better stability and barite suspension capability 20 hours after the imaging fluid was poured into water. It is noticed that in the recipe (a), barite and canola oil floated up to the water table since the barite concentration was not high enough to maintain the imaging fluid density. When testing recipe (b), the canola oil separated from the imaging fluid and floated up. It is because the stearic acid concentration was too low to provide enough viscosity. Trials were also conducted to test the viability of higher barite or stearic acid concentrations than the optimum recipe. It was found that higher barite concentrations increase the cost of the imaging fluid, requiring higher stearic acid concentration to increase the viscosity and maintain the imaging fluid stability. On the other hand, higher stearic acid concentrations induce the problem of low flowability.

Figure 3-9 Comparison of the stability under water between normal oil-based fluid and imaging fluid. Left: normal oil-based drilling fluid under water after 15mins. Right: novel imaging fluid under water after more than one month.

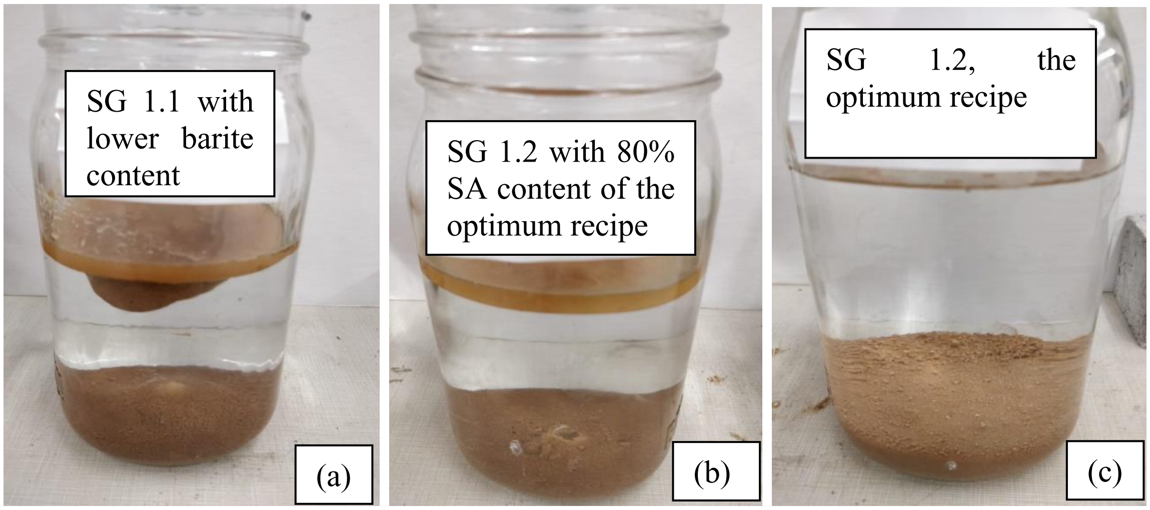

Figure 3-8 Comparison of the different imaging fluid recipes 20 hours after poured in water, at 20°C room temperature. (a): recipe with a lower Specific Gravity (SG) than the optimum recipe. (b): recipe with a 80% Stearic Acid (SA) content of the optimum recipe. (c): the optimum recipe

3.4 LWD field data acquisition and analysis of the rotary-percussion drilling

In this study, the Atlas Copco T40 FlexiROC rotary percussion drilling rig was used for the blasthole drilling. The diagram is given to illustrate the main components of the rig. The description of each component is given in Table 3-3.

The Logging-While-Drilling (LWD) system developed for the T40 blasthole rig consists of i) hydraulic and pneumatic pressure transducers that measure the various drilling parameters that are displayed on the drilling parameter console in the cab, ii) a cable sensor (string pot) that measures the travel of the hydraulic line carousel (which is linearly proportional to the penetration depth of the drill bit), iii) an electronic Data-Acquisition (DAQ) system to record the data from the various electronic sensors, and iv) electrical cables, pneumatic and hydraulic fittings to connect the sensors to the DAQ system. The proposed installation of these various LWD components is summarized in this section.

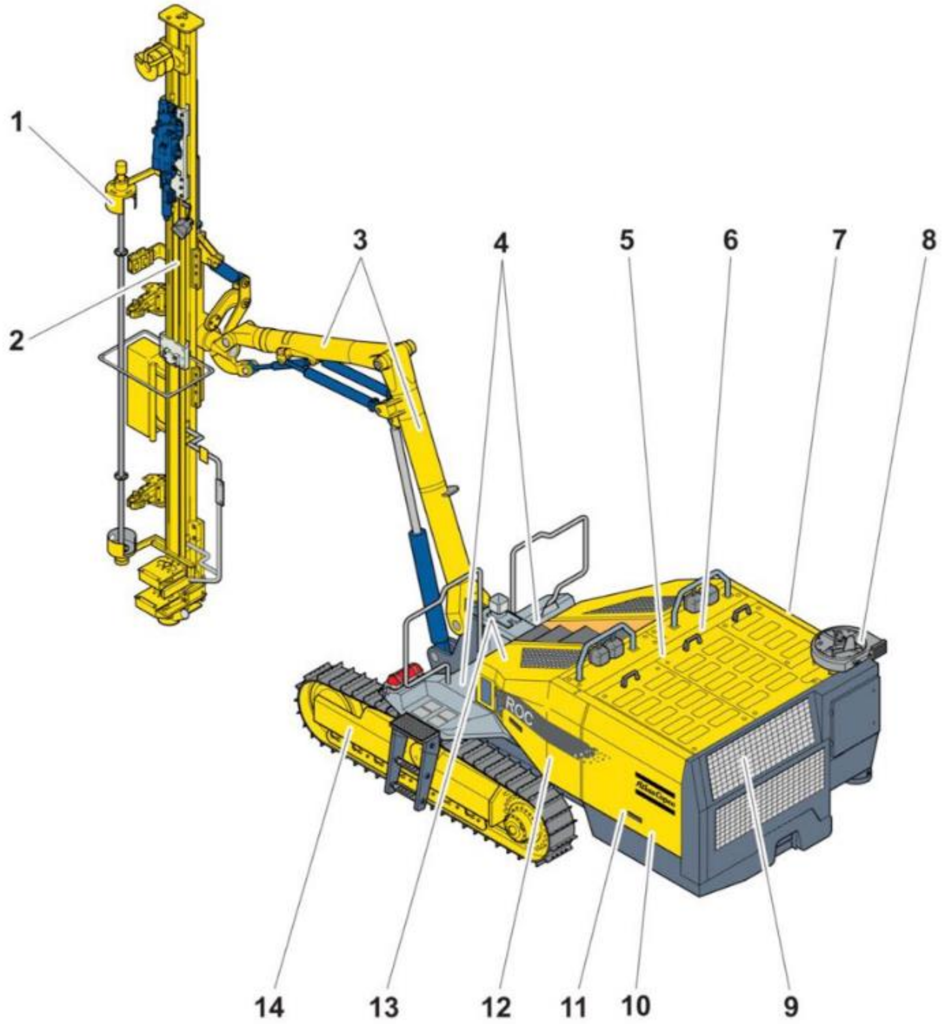

Figure 3-10 Principal components of Atlas Copco T40 FlexiROC

Table 3-3 Description of the Atlas Copco T40 FlexiROC principal components

NUMBER	COMPONENT
1	Rod handling equipment (RHS)
2	Feeder
3	Boom system
4	Operator platforms
5	Radiator
6	Hydraulic oil cooler
7	Hydraulic oil pumps Dust
8	Dust collector (DCT)
9	Diesel engine
10	Compressor
11	Hydraulic oil pumps
12	Electric cabinet
13	Radio receiver
14	Track frames

Mounting of depth sensor:

The depth sensor (string pot sensor) is mounted on the top plate (13.75” x 7”) located on the mast of the drill string, as shown in Figure 3-11 below.

The cable of the depth sensor will be attached to a spring that hooked into a pre-existing small hole on the hose drum.

The cable sensor ordered comes with a bracket that is welded to the top plate. It is welded in a position that properly aligns the cable. Local welding equipment is required for this bracket.

The three wire electrical cable from the string sensor will be spliced to a 14 AWG tech cable. This wire will then follow the bundle of wires already on the rig back to the cabin and the electrical panel.

Transducer mounting:

The five transducers will be tied into the system at the bulkhead outside of the rig's cabin. This is the bulkhead where the hoses run to the pressure gauges inside the cabin.

Figure 3-11 Top plate for mounting and the hose drum for cable connection, and the pressure hoses with labelling

The female hose connects to the male connector on the yellow panel in the form of a JIC-4 connection. The transducers have a 0.25 inch NPT connection. Therefore, the tees purchased will have a final configuration of 4MJ - 4FP - 4FJ. These were purchased from Atlantic Hoses and Fittings.

A tee will be inserted into the following pressure lines: GF1 (feed), GH1 (percussion/hammer), GDP5 (damper), GRR2 (rotation), and GA1 (air purge). Hose connections and labeling are shown in Figure 3-11.

Figure 3-12 Steel mount for DAQ system 24V supply inside A1 panel

Once the T-piece is inserted, a pressure snubber connects all hydraulic lines. The transducers are then connected to the snubbers. All electrical wiring is routed back to the electrical panel.

Mounting the DAQ system

The original plan was to mount the DAQ system in the cab. However, it was determined that it would be easier to mount the system next to the A1 Electrical panel on the right side of the T40 FlexiROC. The 8.6"L X 6.3" box containing the DAQ system is mounted on the steel bracket to the left of the A1 Electrical panel. This is presented in Figure 3-12.

Due to the small area of the existing steel plate, it may be necessary to weld another plate to the side of the fuel. Shallow holes will then be drilled into the plate for mounting. Drilling and welding equipment will be required on site for this attachment.

The DAQ system will be powered from the 24V terminal inside the A1 plate and grounded by connecting to the grounding wire inside the A1 plate. Power and ground wires are wired from the A1 panel to the DAQ system. These are wired through cable glands. All cables from sensors are wired into the DAQ system through cable glands. The whole LWD data recording process is shown in

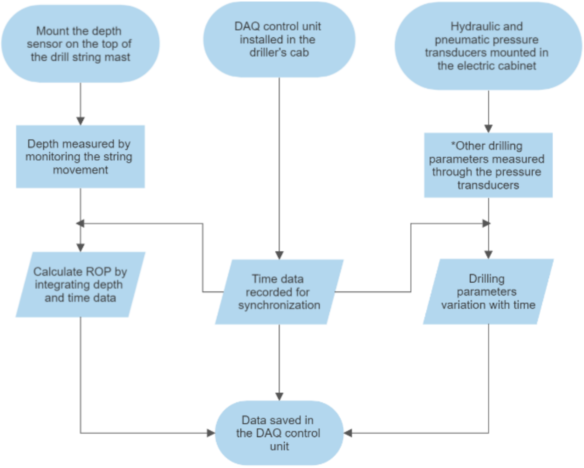

Figure 3-13 Flow chart of the drilling parameter collection through the DAQ system from the rotary percussion drill rig. *: Other drilling parameters indicate: Rotation pressure, feed pressure, percussion pressure, torque pressure, damping pressure and flushing air pressure

3.5 Indentation tests and disk cutter drilling lab experiments

For this study, granite and Rock-Like Material (RLM) blocks were prepared into core samples of a diameter of 2 inches from granite blocks. The mechanical properties were determined before the Indentation test and the result serves as a reference for the indentation test (Shah, 2020; Quan, 2021).

This synthetic type of RLM is a kind of concrete manufactured by researchers at Memorial University. The strength being categorized as medium is due to the solid mixture's lesser water content and greater cement content (Zhang, 2017). The recipe for the synthetic rock is specified below in Table 3-4.

Table 3-4: Recipe for Medium Strength rock. (Zhang, 2017)

Materials	Designed Quantities	Used Quantities
A: C: W	3: 1: 0.45	3: 1: 0.45
Aggregate	30 kg	31.436 kg
Cement	10 kg	10 kg
Water	4.5 kg = 4500ml	3.064 kg = 3064 ml
Water Reducer	N/A	N/A
Superplasticizer	Daracem 19= 60 ml	Daracem 19= 60 ml
Silica Fume	N/A	N/A

Table 3-5: Specifications of the servo-control loading frame.

Load capacity	Minimum speed	Maximum speed	Position accuracy	Load measurement accuracy	Strain measurement accuracy
kN	mm/min	mm/min	mm		
250	0.001	500	± 0.02	± 0.4%	± 0.05%

All of the rock indentation tests were performed by a servo-controlled loading frame. The instrument was an Instron 5585 series dual-column floor model weighing 2100lbs. The maximum capacity for tension or compression on the instrument is 250 kN and works on the principle of closed-loop servo control. The metallic indenters used in indentation are mounted on the top platen. The compression loading rate is chosen ahead of time, and the experiment runs for 3 minutes. The specification of the servo-controlled loading frame is given in Table 3-5.

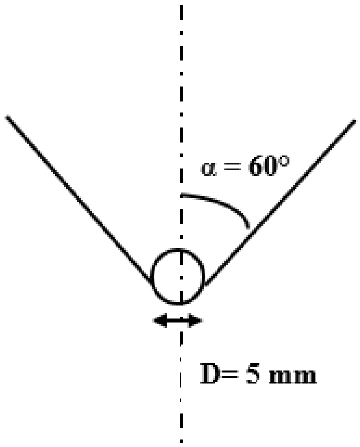

Figure 3-14 Geometry of indenter used in this study

Indentation test results depend on the shape and hardness of the metallic indenters influence the result of the indentation test. In this study, the indenters have a spherical tip; hence, changing their dimensions changes the geometry of the indenter. Two parameters that remained the same for both studies were (i) the hardness of the indenter and (ii) the apex angle (α), which is the angle between the cone of acceptance and the central axis passing through the indenter. The hardness of the indenter was 58HRC in the Rockwell hardness scale for metals following the point load apparatus from ASTM D5731-16 (ASTM, 2016), and the value of the apex angle was 60°. For example, the geometry of the indenter plays a significant role in rock fracture and its responses (Thiercelin and Cook, 1988; Uboldi et al., 1999).

The confinement around the rock cores was made with a metal strap, as shown in Figure 3-15. The two ends of the straps were connected by a nut and bolt assembly. Tightening the bolt brought the two ends of the straps together around the circumference of the rock core and thus acted as confinement.

For this project, a rock core had to be cut to meet the dimensional requirements of a length-to-diameter ratio of 1. Additionally, using a grinder, the ends of the core were flattened and made smooth. For rock indentation testing, a complex process using the ISRM draught was used (Szwedzicki, 1998). In a mold with a 4-inch diameter, concrete was poured around the core and allowed to cure for two days at ambient temperature. The mold's specific strength was in the range of 30-35MPa. The plastic mold containing the hardened concrete retaining the rock core was removed, and a specially made metal strap was wrapped around it. In this investigation, granite and a medium-strength rock-like substance were used as rocks.

Figure 3-15 Metal strap used for in this study

Chapter 4: Measurement of rock dielectric permittivity and EM (Electromagnetic) wave velocity

The research work of this chapter has been prepared for submission to the peer-reviewed journal.

4.1 Co-authorship Statement

Zijian Li: Laboratory Experiment, Data Processing, Numerical Simulation, and Writing Manuscript

Michael Marsh: Support on Laboratory Experiment

Ramin Rafiei: Support on Data Processing and Numerical Simulation

Dr. Stephen Butt: Supervision and Reviewing

4.2 Abstract

This study presented and validated a practical and rapid method to measure the EM wave velocity and the Relative Dielectric Permittivity (RDP) of NQ size rock cores using 2.3GHz shielded GPR by lab experiments. Through lab tests on homogeneous granite NQ size cores, the availability of this method was proven, and the GPR system layout was determined. Based on the NQ rock cores obtained from the diamond core drilling in the mining field, the EM wave velocity and the dielectric permittivity were measured for quartz and mafic volcanic samples. X-ray diffraction (XRD) and Mineral Liberation Analyzer (MLA) was conducted on the quartz ore and the mafic volcanic host rock to quantify their mineral composition. The RDP value obtained by the GPR system agreed well with the literature recommendation value. It showed better reliability and economic efficiency than the lab experiment system based on the open coaxial probe. The electrical conductivity and the magnetic susceptibility of the rock sample were measured, and their influence on the EM wave velocity was negligible, with quasi static assumption used in solving the Maxwell equation. It was determined that the RDP of the mafic volcanic group and the quartz group had a noticeable difference, which proved the practical foundation for distinguishing the vein (quartz) / host rock (mafic volcanic) using borehole GPR in the studied mining zone. Through Finite Difference Time Domain (FDTD) method simulation using gprMAX, the wave propagation path in the NQ size core was investigated. The

study on the optimum core length was expanded for the NQ size core, and the suggestion to choose the GPR antenna frequency was made.

4.3 Introduction

GPR is a Non-Destructive Technique (NDT) used to image the near-surface structure. GPR has been used to conduct remote surveys on subsurface structures (Pipan et al., 2000; Booth et al., 2016). Many effective radar surveys and results are being presented in a wide range of application fields., particularly for archaeological field surveys (Lazzari et al., 2018; Zhou et al., 2015), geophysics (Grasmueck et al., 2005; Jeannin et al., 2006), and civil engineering (De Chiara et al., 2014, Benedetto and Pajewski, 2015).

The accurate interpretation of the GPR field data, however, requires the determination of the velocity profile of the EM wave at different depths since the spatial distribution of the lithology may not be homogeneous. The EM wave velocity of rock is directly related to its dielectric permittivity. Because these characteristics affect GPR signal propagation, reflection, and data resolution, it is critical to investigate the EM wave velocity distribution in the test field. In field practice, hyperbola fitting and Common Mid-Point (CMP) measurements can be taken to determine the velocity of the formation. In the field trial of the research site, however, hyperbola reflection was not found in the borehole GPR survey. In addition, the CMP method is not suitable for our project since the CMP method requires a specifically designed GPR system. Thus, a practical and suitable method to measure EM wave velocity and the RDP of the rock in the test site.

In this study, a series of borehole GPR surveys were planned to be conducted at a gold mine site. The site is in the igneous rock zone. The ore formation is mainly quartz, while the host rock is mafic volcanic rock. The spatial lithology distribution in the test site is complicated since the alteration is observed in the host rock. Diamond coring is a common practice to obtain the rock core from the subsurface geology and to drill the borehole for the borehole GPR survey, and the NQ size core was obtained from the surface to 100m deep. Thus, the NQ size core can be used for the rock EM wave velocity and RDP measurement. The lithology alteration of the rock core was identified, and X-ray diffraction (XRD) and Mineral Liberation

Analyzer (MLA) were conducted on the quartz ore and the mafic volcanic host rock to quantify their mineral composition.

This study proposes a practical approach to measuring the dielectric permittivity of the rock. The 2.3 GHz, high-frequency GPR system was used to measure the EM wave velocity and then calculate the dielectric permittivity of the NQ size rock core retrieved from the diamond coring drilling. The test procedure is standardized through a series of lab tests to minimize the environment and system noise and enhance the signal quality. The optimal length of the NQ size rock core is determined from the laboratory experiment. Based on quartz ore and mafic volcanic host rock, ten different lithologies were further sorted, and 45 rock cores were tested. The dielectric result obtained from the GPR system was compared with the result obtained through the DAK-TL2 system and the value obtained from the previous studies. By comparing the experimental result with the RDP value measured in previous researches (Zheng et al., 2005; Campbell and Ulrichs, 1969; Igel and Kuntzer, 2013), the availability of this GPR method to measure the dielectric of the NQ size core was proven with confidence.

A series of numerical simulations were carried out with gprMAX, an open-source software that employs the finite difference time domain method (FDTD) for the electromagnetic simulation. FDTD is a time domain discretization method that is robust, accurate, flexible, and computationally efficient, making it ideal for GPR simulation (Warren et al., 2016). The wave propagation path of the EM wave in the NQ size core was described by the gprMAX simulation, and suggestions were provided for the optimization of this method.

4.4 The test field geometry and the rock sample lithology characterization

In the prospective gold mine site, the mineralization is generally associated with veins, which consist of multiple generations of parallel milky-white quartz. The crack-seal, comb textures, altered wall-rock fragments, and weakly preserved lamination were observed. Visible gold occurs as fine grains or small flecks of gold are observed within the massive quartz veins. The vein is hosted by massive fine-grained, mafic volcanic and gabbroic intrusive rocks, which are part of the Snooks Arm Group. The quartz vein is

Figure 4-1 Quartz Veining Associated with a Sheared Mafic dyke

up to 2m thick, with a dipping angle of 60 degrees. The spatial distribution of the lithology is not homogeneous, and alterations between different lithologies were observed (Li et al., 2019). The field observation of the rock sample is shown in Figure 4-1 and Figure 4-2.

Diamond coring drilling was conducted in the middle of the vein, following its dipping angle. Approximately 100m of NQ size core were obtained. The lithology can be categorized into two groups: the quartz group and the mafic group. The quartz group noticed stains on the quartz due to the alteration. Gabbro was the representative lithology for the mafic, sorted into the massive flow and the ash tuff. Frequent alteration in the mafic group was also observed. The core sample corresponding to different lithologies is shown in Figure 4-3.

Figure 4-2 The lithology of the rock cutting samples changes with depth: Surrounding rock of Mafic Massive Flow at 2m deep (a), quartz at 4.5m deep (gold ore) (b), and a small layer of Quartz/Altered at 7m deep (c), (Li et al., 2019).

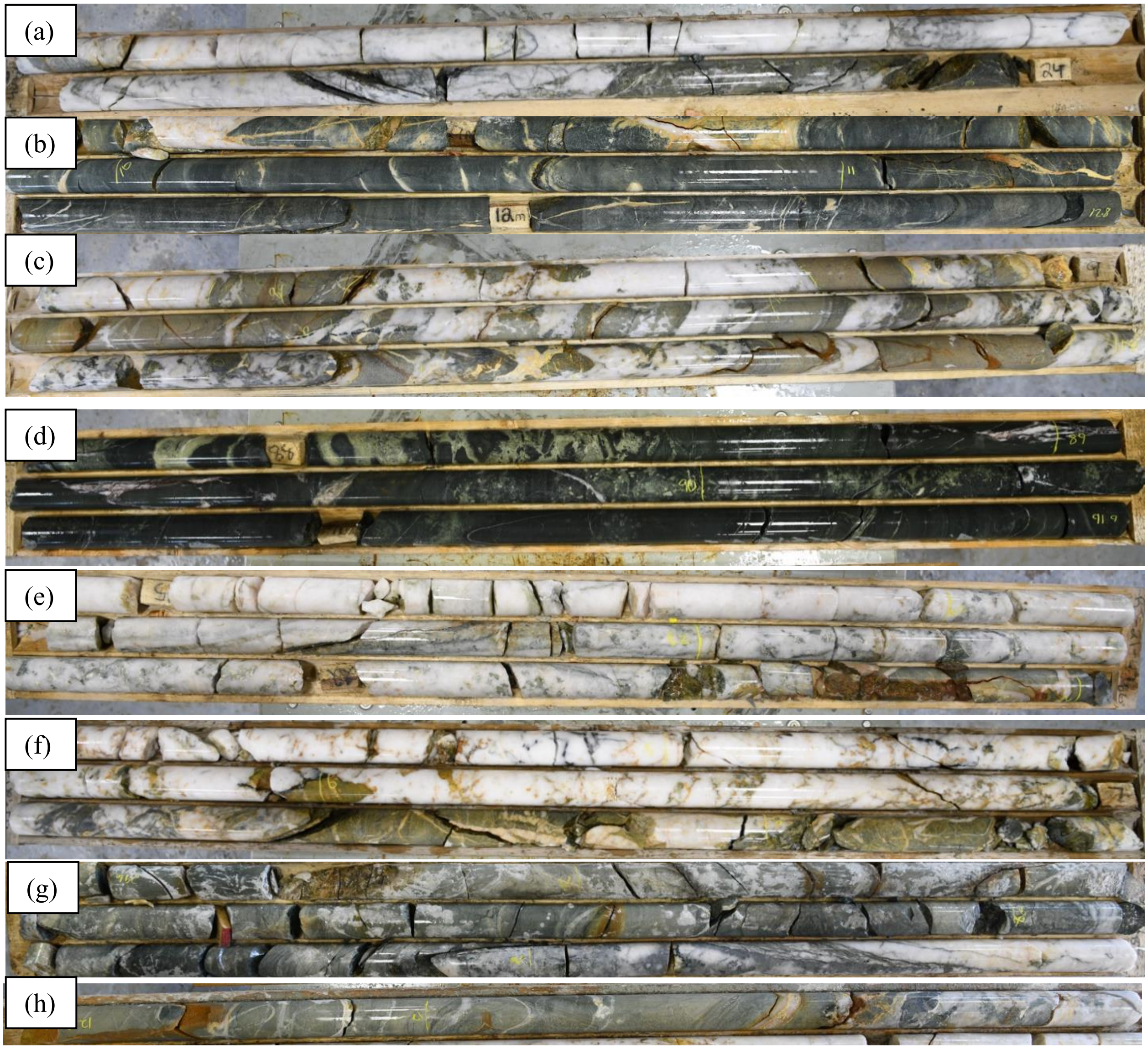

Figure 4-3 Lithology identification from the NQ size core sample. (a) vein. (b) Mafic ash tuff. (c) altered (d) Mafic Massive Flow - Altered/Mafic Massive Flow. (e) Vein/Altered. (f) Quartz/Altered. (g) Altered/Mafic Ash tuff - Altered/Vein. (h) Mafic Ash tuff/Altered.

XRD and MLA technology were used to quantitatively study the mineral composition of the rock sample. XRD is a technology used in materials science to quantify a specific material's crystallographic structure. The X-rays' intensities and scattering angles that escape are measured by exposing a material to incident X-rays. Then the mineral composition of the material can be calculated. The XRD technology has been successfully applied in civil and petroleum engineering to characterize the mafic and sedimentary rocks (Shau et al., 1990; Al-Jaroudi et al., 2007). Because XRD results are averaged for heterogeneous

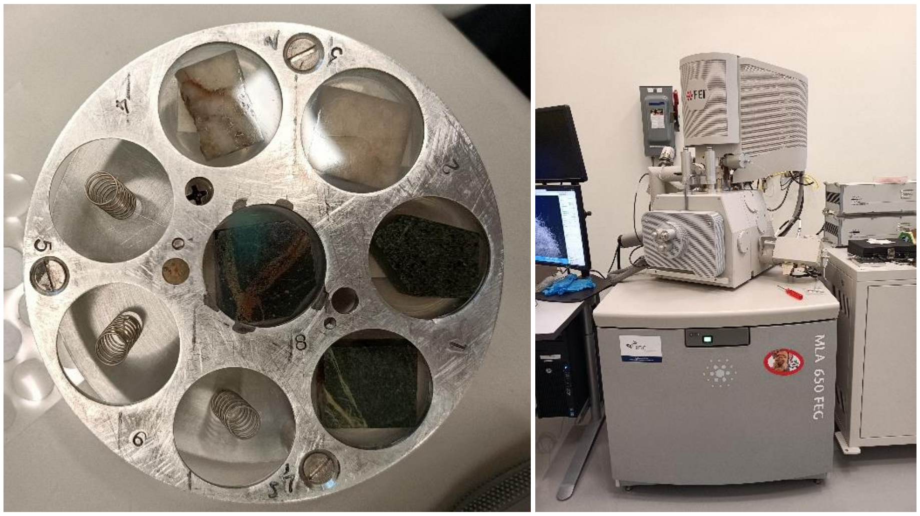

Figure 4-4 Left: Rock sample coated in epoxy mounted on the holder. Right: The MLA-SEM facility in the CREAIT laboratories at Memorial University in Newfoundland

materials, they may be ambiguous, as are inferences about stacking sequences. (Shau et al., 1990).

Based on Scanning Electron Microscopy (SEM) and Quantitative Evaluation of Minerals by Scanning Electron Microscopy (QEMSCAN) (Grant et al., 2016), MLA is commonly used to evaluate ore mineralogy and metallurgical products. The rock sample is put in a mold and filled with epoxy resin for sample preparation. The epoxy solution is required to cure before polishing and instrument analysis (Grant et al., 2018). Then the test sample is pre-processed and examined by the SEM equipment, as shown in Figure 4-4. The MLA device generates a false-color digital map of the mineral phases of the rock sample cross-section.

Figure 4-6 Mafic volcanic transition to massive quartz vein, 25.2m-29m. Red box marks the XRD and MLA sample location.

Figure 4-6 Light dark grey mafic massive flow, 87.6m-92m. Red box marks the XRD and MLA sample location.

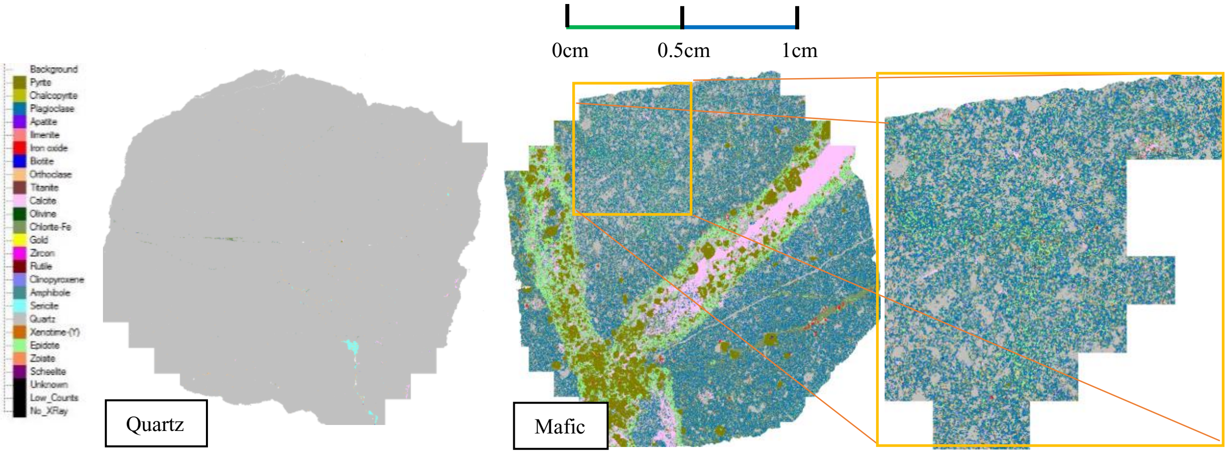

Figure 7 MLA cross-section mineral analysis of Quartz sample (From left to right: legend, quartz sample result, mafic volcanic sample result, and the subsection mafic volcanic sample result)

Then the weight ratio of each mineral is calculated from the area percent of the analyzed cross-section (Feely et al., 2019).

Two rock samples were selected for XRD and MLA tests; one is quartz, while the other is massive mafic flow. In Figure 4-6 and Figure 4-6, the rock core processed for XRD and MLA is marked in red squares. Although the number of samples tested is limited, the mineral component can still provide a significant reference for rock characterization in terms of lithology. In this study, the lithology and the mineral composition will be used as the reference for the rock characterization based on the relative dielectric permittivity (RDP) determination through the 2.3GHz GPR. The mineral content result is obtained by MLA and XRD results, respectively. Table 4-1 to Table 4-4 show the mineral content results for these two lithologies.

Table 4-1 MLA mineral content result: Mafic volcanic transition to massive quartz vein

Mineral		Wt.%
Total		100.00
Quartz	SiO_2	99.54
Orthoclase	$KAlSi_3O_8$	0.16
Sericite	$KAl[AlSi3O_{10}](OH)_2$	0.16
Calcite	$Ca(CO_3)$	0.05
Chlorite-Fe	$Fe(ClO_2)_2$	0.05
Amphibole	$A_{0–1}B_2C_5T_8O_{22}(OH, F, Cl)_2$	0.02
Note	For Amphibole, A = Na, K; B = Na, Zn, Li, Ca, Mn, Fe^2+, Mg; C = Mg, Fe^2+, Mn, Al, Fe^3+, Ti, Zn, Cr; and T = Si, Al, Ti.	
	For Epidote, A is usually calcium (Ca), though manganese (Mn) or cerium (Ce) is sometimes substituted, and B is generally aluminum (Al), with the main substitution being ferric iron (Fe^{+3}).	

Table 4-2 XRD mineral content result: Mafic volcanic transition to massive quartz vein

Phase ID	Chemical Formula	PDF-#	Wt% (ESD)
Quartz	SiO_2	98-000-0369	98.5 (1.1)
Zinnwaldite 2M1	$K(Fe, Al, Li)_3(Si, Al)_4O_{14}(OH)F$	98-000-0495	1.5 (0.1)

Table 4-3 XRD Result: Light dark grey mafic or massive altered volcanic flow

Phase ID	Chemical Formula	PDF-#	Wt% (ESD)
Quartz	SiO_2	98-000-0369	34.0 (1.9)
Zoisite	$Ca_2Al_3[Si_3O_{12}]OH$	98-000-0495	21.5 (3.3)
Muscovite 2M	$KAl2[Sr3Al]O_{10}(OH)_2$	98-000-0321	13.6 (2.6)
Kaolinite	$Al_4(OH)_8(Si_4O_{10})$	98-000-0261	10.2 (1.9)
Augite	$FeCa_4Si_8Mg_{2.96}O_{24}$	98-000-0102	8.0 (2.0)
Calcite	$Ca(CO_3)$	01-086-4272	7.3 (1.0)
Dolomite	$MgCa(CO_3)_2$	98-000-0200	3.7 (0.7)
Biotite	$K(Mg,Fe)_3Al[Si_3O_{10}]F_2$	98-000-0117	1.0 (0.5)
Vaterite	$Ca(CO_3)$	98-000-0451	0 5 (0 2)
Hedenbergite	$Ca(Fe^{2+}, Mg)Si_2O_6$	98-000-0239	0.2 (0.3)

Table 4-4 MLA mineral content result: Light dark grey mafic or massive altered volcanic flow

Mineral		Wt.%	Area%
Total	Formula	100.00	100.00
Plagioclase	$NaAlSi_3O_8 – CaAl_2Si_2O_8$	27.50	28.95
Quartz	SiO_2	24.05	25.90
Chlorite-Fe	$Fe(ClO_2)_2$	12.92	12.18
Amphibole	$A_{0–1}B_2C_5T_8O_{22}(OH, F, Cl)_2$	12.51	11.59
Orthoclase	$NaAlSi_3O_8$	8.25	9.11
Epidote	$A_2B_3(SiO_4)(Si_2O_7)O(OH)$	6.18	5.06
Clinopyroxene	$(Ca,Mg,Fe,Na)(Mg,Fe,Al)(Si,Al)_2O_6$	5.29	4.39
Titanite	$CaTiSiO_5$	2.16	1.76
Calcite	$CaCO_3$	0.71	0.74
Biotite	$K(Mg,Fe)_3AlSi_3O_{10}(F,OH)_2$	0.17	0.16
Iron oxide	Fe_2O_3	0.12	0.06
Apatite	$Ca_5(PO_4)_3(F, Cl, OH)$	0.07	0.06
Pyrite	FeS_2	0.06	0.03
Note:	For Amphibole, A = Na, K; B = Na, Zn, Li, Ca, Mn, Fe^2+, Mg; C = Mg, Fe^2+, Mn, Al, Fe^3+, Ti, Zn, Cr; and T = Si, Al, Ti.		
	For Epidote, A is usually calcium (Ca), though manganese (Mn) or cerium (Ce) is sometimes substituted, and B is generally aluminum (Al), with the main substitution being ferric iron (Fe^{+3}).		

By comparing the MLA and XRD results, it is noticed that the quartz sample has a very high concentration of pure quartz (99.54% from MLA and 98.5% from XRD). Although the weight percentage for each content is not the same for the mafic sample, it is confirmed that it has both feldspar/quartz and magnesium/iron content. The sample was identified as mafic in the field because of its dark color, though its high feldspar/quartz content should not be ignored.

XRD has the ability to discriminate minerals with different crystal structures with a high with high resolution (grain size of several nm) and fast analysis speed. More importantly, XRD quantitative analysis is the only reliable method for quantitative analysis of polymorphs where the chemical analysis methods are not sensitive. However, the detection limit is relatively high (0.1%-1% weight ratio). In addition, the mineral identification becomes difficult when the overlapping interference and lack of contrast of the peaks are detected in the diffraction pattern (Lou et al., 2020).

Although MLA possesses high resolution and precise quantitative mineral content characterization ability, it has several drawbacks. It is challenging for MLA to distinguish minerals with similar chemical compositions or similar crystal structures (crystal polymorphs). In addition, it is also reported that the lack of reference material influences the accuracy and confidentiality of the result (Sylvester, 2012).

In terms of the rock EM properties study, MLA shows a better performance because it presents a very sensitive and quantitative chemical content of the minerals comprising the rock. When we are looking into the crystal structure of the mineral grain, however, the MLA is less precise than the XRD, since MLA cannot separate minerals with the same chemical content in some circumstances. In the XRD result, both calcite (7.3%) and vaterite (0.5%) were presented, while only the calcite (0.71%) was observed in the MLA result. The reason should be that the calcite and vaterite have the same chemical content (CaCO3) but different crystal structure, thus the MLA cannot identify these two minerals according to current reference library. Moreover, the Muscuvite 2m (13.6%) characterized in XRD test was identified as Biotite (0.17%) in MLA for the same reason. It is noticed that the mineral type and content obtained by XRD and MLA do not exactly match. Despite the ambiguity in the crystal polymorphs discrimination of the MLA, it is because the XRD result interpretation was not totally precise, which requires thorough understanding of the minerology of the test site. In summary, MLA presents reliable quantitative mineral analysis for the rock sample in this study. Although the XRD result is not precise in terms of the mineral type and content, it can provide reference for the MLA to calibrate the mineral type (crystal polymorphs).

4.5 GPR laboratory test to measure the dielectric permittivity of the rock core

The objective of this study is to develop and validate a practical method for measuring the dielectric permittivity of the rock, since the dielectric permittivity determines the EM wave velocity of the rock media. For the subsurface GPR survey, the transformation of the time domain data to the distance domain requires the rock EM velocity. Then, the distance between the GPR antenna and the boundary of the vein is determined.

The average thickness of the vein in this project is approximately 2m, and the distance between the antenna and the vein is about 1m. The allowed error of the distance determination is 10cm in this project. Thus, the error of the measured EM wave velocity of this method should be within 10%.

In order to achieve the required accuracy, the GPR specifications should be carefully designed. The GPR's radial resolution mainly depends on the center frequency and the antenna's bandwidth. According to the Federal Communications Commission (FCC), the Ultrawideband (UWB) has a fractional bandwidth of higher than 0.2 (Kumar, 2021). The fractional bandwidth is described by:

$$BW_{frac} = \frac{f_h - f_l}{f_c} \times 100\% \tag{4-1}$$

Another term, bandwidth ratio is given as:

$$BW_{ratio} = \frac{f_h}{f_l} : 1 \tag{4-2}$$

Where, BW_{frac} is the fractional bandwidth, BW_{ratio} is the bandwidth ratio, f_l is the lower frequency of the operation band, f_h is the higher frequency of the operation band, and f_c is the center frequency of the operation band.

This study uses a shielded GPR unit with a center frequency of 2.3GHz. The maximum penetration depth is approximately 0.5m in dry concrete, indicating that the measurement's NQ core should be shorter than 0.5 m. The bandwidth spectrum of the GPR is given in Figure 4-7. According to equation 4-1, the lower and higher frequency of the operation band are 1.7GHz and 2.3GHz, respectively, and the fractional bandwidth of this GPR is 0.64, which can be categorized into the UWB GPR.

The experiment layout is identified in this research, where the antenna faces upward, with a holder used to isolate the antenna and the ground. The antenna is shielded to minimize the noise from reflectors other than the core. An open space is needed for the experiment where no reflectors were present within a 3m distance around the antenna. Applying this layout, as shown in Figure 4-8, minimizes the environment noise.

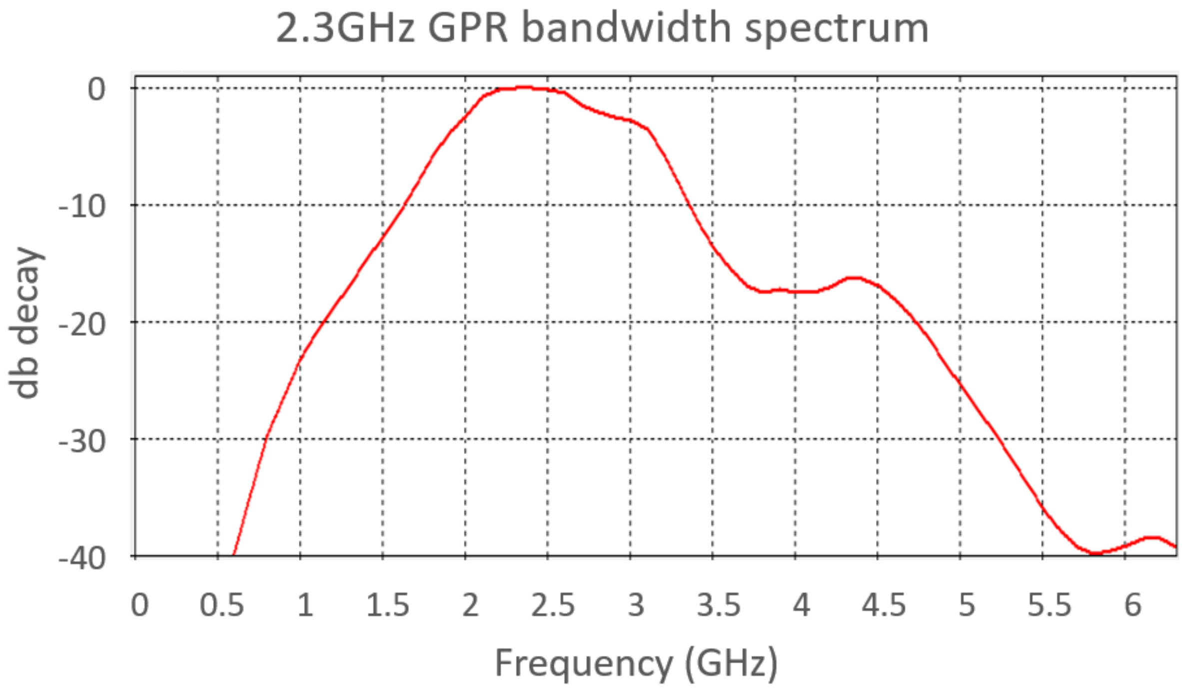

Figure 4-7 2.3GHz GPR bandwidth spectrum

The two-way travel time of the EM wave in the core can be obtained from the GPR reflection result. This equipment setup does not require a lab environment suitable for fieldwork. With the consideration of the antenna separation, the EM velocity of the core is calculated as follows:

$$v = \frac{\sqrt{4 \times L^2 + d^2}}{\Delta t} \tag{4-3}$$

Where, v is the EM wave velocity (m/ns), L is the core length (m), d is the antenna separation (40mm or 0.04m), and Δt is the two-way travel time (s). The symbols are shown in Figure 4-8.

Before the test on the core, the GPR system noise is recorded with the antenna on the ground, facing upward. It is noticed that the system noise obviously influences signal in the time window between 1ns and 10ns, as presented in Figure 4-9. The recorded system noise was subtracted from the raw data when processing the reflection data to enhance the signal-to-noise ratio. An example of the system noise canceling is shown in Figure 4-9.

The procedures for RDP measurement test using the GPR system based on the transmission/reflection (T/R) method is as follows. First, the core length is measured before the test. Then the core is put in the

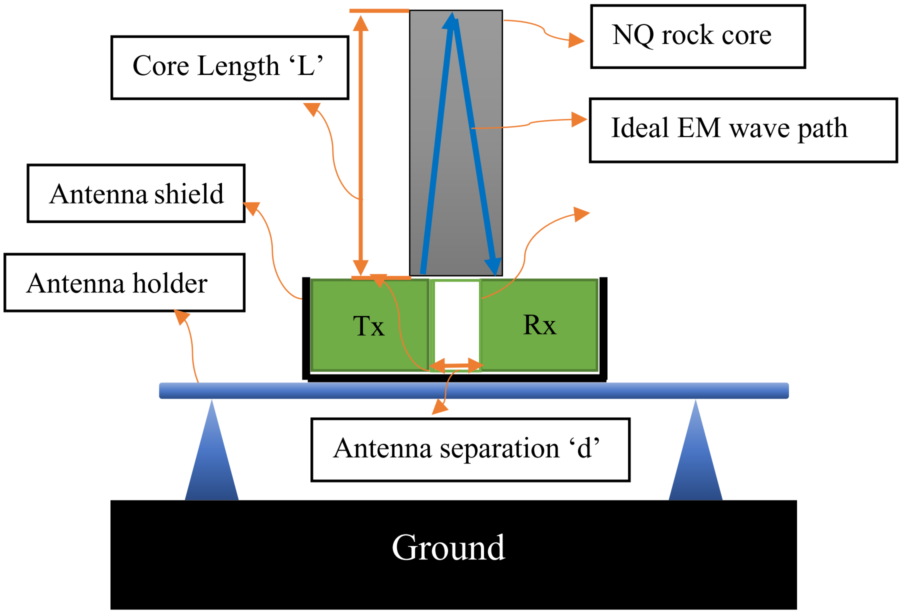

Figure 4-8 The GPR test layout for the NQ core dielectric measurement

middle of the GPR, between the transmitter and the receiver. The GPR record the signal at the time triggering mode (rather than the distance triggering mode). After thesytem noise cancelling, the two way travel time Δt is obtained from the GPR result interpretation. With the value of core length L and antenna separation d, the em wave velocity in the core is then calculated using equation 4-3, and the dielectric

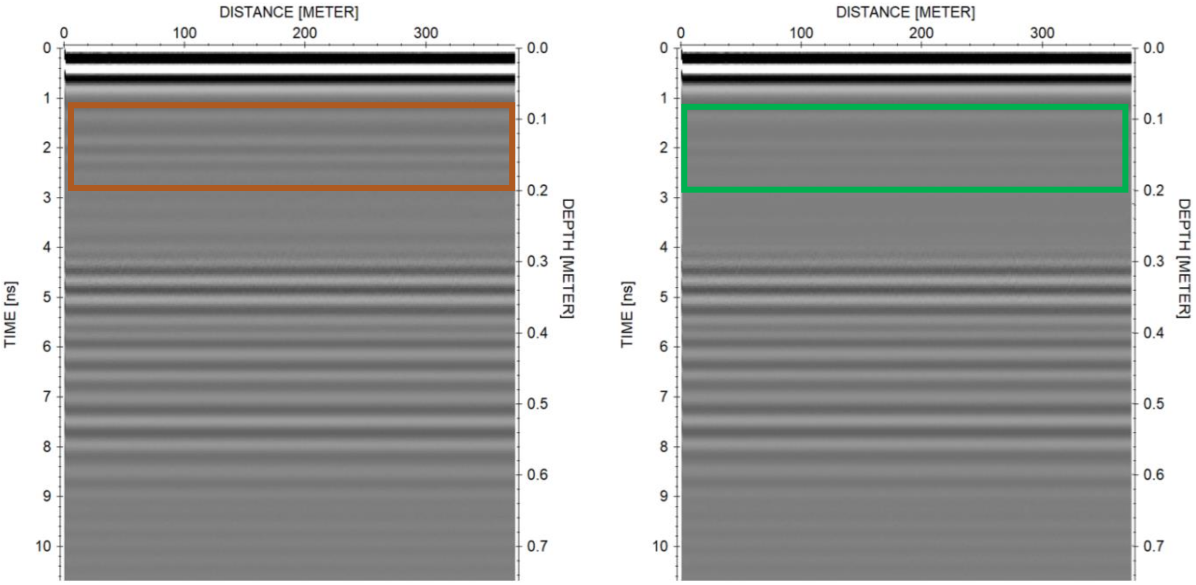

Figure 4-9 Left: GPR reflection result on a 30cm NQ rock core. The red square marks the system noise. Right: GPR reflection result after system noise cancelling. The green square marks the mitigated system noise after noise cancelling using the recorded system noise.

permittivity is calculated from equation 4-4.

In order to verify the accessibility of the test, a series of homogeneous granite NQ size cores were used in the test. The cores have different lengths. The reflection response from these cores will be compared to reveal the influence of the core length on the imaging quality. According to the test result, it is validated that the 2.3 GHz shielded GPR can measure the velocity and the dielectric permittivity of the homogeneous NQ core with lengths ranging between 10cm and 30cm. Measured from 7 granite samples, the EM wave velocity of the granite is determined as 0.13m/ns, with a standard deviation of 6.39 e^{-4}.

4.6 The test result of rock cores with different lithologies

NQ size cores picked up from different intervals are cut into flat cylinders for the test. For each core, measurement was conducted twice, with the core placed in different directions by flipping the core upside down. In our research scope (rock material), the influence of the electrical conductivity and the magnetic susceptibility on the dielectric constant can be ignored. The lithology of the core has been sorted into ten subcategories. Based on the RDP value, the lithologies can be sorted into the low dielectric (4-4.7) group and the high dielectric (6.5-8.6) group.

Table 4-5 RDP measurement result for quartz (green) and mafic (blue)

Lithology	**RDP**	**EM wave velocity (m/ns)**	**Lithology Group**
Altered/Vein	4.121	0.148	Quartz (Ore)
Quartz/Altered	4.473	0.142	
Vein/Altered	4.549	0.141	
Vein	4.705	0.140	
Mafic Ash tuff/Altered	6.554	0.117	Mafic (Host rock)
Mafic Ash tuff	6.782	0.116	
Altered	6.922	0.114	
Mafic Massive Flow	7.231	0.112	
Altered/Mafic Massive Flow	7.587	0.109	
Altered/Mafic Ash tuff	8.636	0.102	

In summary, the vein (quartz), altered vein (quartz), and vein (quartz) altered are categorized in the low dielectric group. The altered, Mafic (ash tuff and massive flow), and mafic altered fall into the high dielectric group. There are two different Altered/Vein samples, which fall into different groups. The result is summarized in Table 4-5. It is proven that the RDP effectively distinguishes the different lithologies in the zone under current development.

The RDP is derived from the EM wave velocity:

$$\varepsilon = \left(\frac{c}{v}\right)^2 \tag{4-4}$$

Where, ε is the RDP (dimensionless), v is the EM wave velocity in the rock media (m/ns), and c is the speed of light (~ 0.3m/ns).

The phase velocity of the EM wave in rock media is given by:

$$v_p = \frac{dz}{dt} = \frac{\omega}{\alpha} \tag{4-5}$$

α is a constant, given as:

$$\alpha = \omega\sqrt{\mu\varepsilon}\left[\frac{1}{2} + \frac{1}{2}\sqrt{1 + \frac{\sigma^2}{\omega^2\varepsilon^2}}\right]^{0.5} \tag{4-6}$$

Where, σ is the conductivity of the rock (S/m); ω is the wave frequency (Hz), and μ is the magnetic permeability (H/m).

For non-lossy materials, like most rock, the conductivity is low ($\sigma \ll \omega\varepsilon$). In this situation, if and are constants (independent of ω), then the EM wave velocity is independent of the frequency, and there is no dispersion. The calculation of α and v_p can be simplified as:

$$\alpha \approx \omega\sqrt{\mu\varepsilon} \tag{4-7}$$

$$v_p = \frac{\omega}{\alpha} \approx \frac{1}{\sqrt{\mu\varepsilon}} \tag{4-8}$$

The RDP of the rock cores was calculated based on the EM wave velocity derived from the GPR test result. The RDP of the rock sample was also measured by the equipment DAK-TL2 system, as shown in Figure 4-10. The DAK-TL2 system is built upon open coaxial probes and has electronics for automatic

Table 4-6 Comparison between the RDP result of 2.3GHz GPR vs. DAK-TL2 vs. Literature value

Sample	**Sample lithology**	**Conductivity (S/m)**	**Magnetic susceptibility (e^{-3} SI)**	**Velocity (m/ns)**	**GPR RDP result**	**Calibrated GPR RDP considering Magnetic and conductivity**	**Error**	**DAK-TL2 RDP result (measured at 2 GHz)**	**Literature RDP (gabbro)**	**Literature RDP (quartz)**
1	Vein	0.00781	0.0108	0.1518	3.906	3.877	0.0074	5.01		4-4.6
2	Mafic Ash tuff	0.00165	0.1621	0.1194	6.311	6.209	0.0164	4.94	7-7.95	
3	Quartz/Altered	0.00174	0.0488	0.1477	4.127	4.115	0.003	3.66		4-4.6
4	Vein	0.00206	0.0048	0.1323	5.141	5.122	0.0037	3.98		4-4.6
5	Mafic/Altered	0.00102	0.1218	0.1161	6.675	6.595	0.0122	2.98	7-7.95	
6	Mafic Massive Flo	0.00424	0.6593	0.1089	7.587	7.567	0.0026	5.15	7-7.95	
7	Vein	0.000718	0.0126	0.1495	4.026	3.992	0.0085	2.92		4-4.6
8	Quartz/Altered	0.00153	0.0157	0.1382	4.713	4.699	0.0029	3.39		4-4.6
9	ltered/Mafic Ash t	0.00735	0.0704	0.1074	7.808	7.776	0.0041	5.56	7-7.95	
10	Mafic Ash tuff	0.00458	0.2522	0.1114	7.255	7.128	0.0178	5.75	7-7.95	

thickness and force measurement. The reflection coefficient obtained at the probe flange, the probe dimensions (diameters, bead permittivity), and the sample thickness are used to derive the dielectric characteristics of the material being tested. It requires the tested material to have a limited thickness (0.1 to 10 mm) in sheet form to fit the equipment. Then, the RDP result measured by the DAK-TL2 system at 2GHz frequency was compared with the GPR measured result and the literature result, with ten samples with different lithologies. The literature result of the RDP of Gabbro (Zheng et al., 2005; Campbell and Ulrichs, 1969) and Quartz (Igel and Kuntzer, 2013) is used as a reference, although our lithology of the cores is not pure mafic or quartz. Thus, the Vein and Quartz/Altered are compared with the reference value of quartz and Mafic Ash tuff, Mafic Massive Flow, and Altered/Mafic Ash tuff compared with the reference value gabbro. The DAK-TL2 result underestimated the RDP of most of the cores (other than sample No.1),

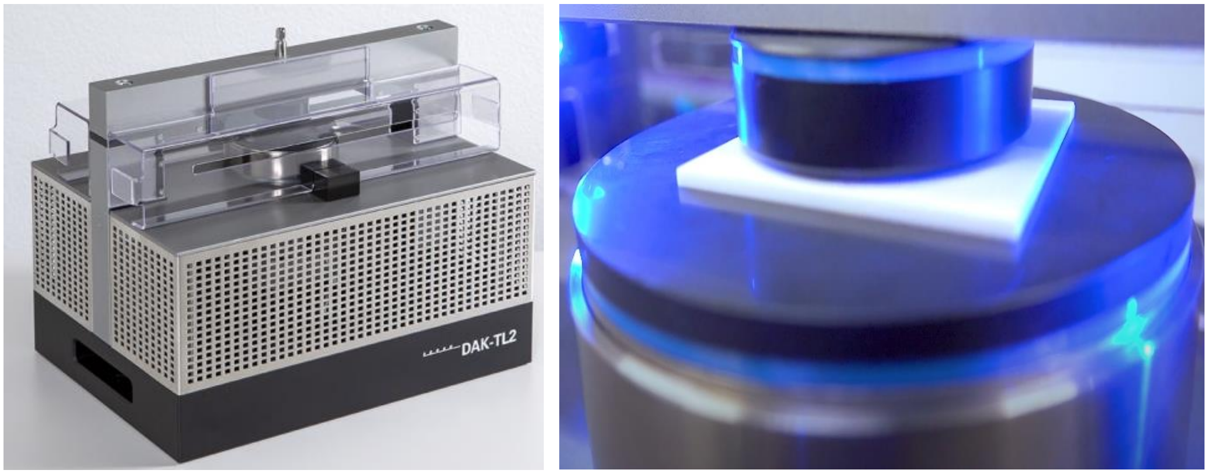

Figure 4-10 Left: DTK-TL2 device. Right: DAK-TL2 calibration for solid material dielectric permittivity measurement

and the 2.3GHz GPR obtained a reasonable result close to the reference value.

The electrical conductivity and the magnetic susceptibility were also measured. In addition, the conductivity of each sample is measured by the KT-20 system, and the magnetic susceptibility is measured with the Multiple Sensor Core Logger (MSCL) in the Earth Science Department of Memorial University of Newfoundland. Based on this information, the calculated RDP through GPR is calibrated. Then, the RDP result was calibrated by considering the influence of electrical conductivity and magnetic susceptibility since the metal content (iron and magnesium, etc.) in the mafic sample is high. The calculation shows that the error due to ignoring the electrical conductivity and the magnetic susceptibility is lower than 2% for all these lithologies, and the average error is 0.79%. It is concluded that the influence of conductivity and magnetic susceptibility on the RDP calculation can be neglected. The dielectric, conductivity, and magnetic susceptibility for ten different lithologies are listed in Table 4-5.

4.7 gprMAX simulation for the test setup optimization

The gprMAX is an FDTD simulation software that simulates EM wave propagation using Yee's algorithm to solve Maxwell's EM field equations. The gprMAX simulation aims to expand the antenna design and the NQ size rock sample length and determine the optimum rock sample length and the recommended antenna separation. Due to the limitation of the lab experiment, only six different lengths of the rock sample were used to validate the Standard Operating Procedure (SOP), and the antenna separation was fixed at 40mm. The material of the core is nonconductive, nonmagnetic quartz, with an RDP of 4.5. The core length ranges from 6cm to 40cm. An example of the gprMAX simulation result is shown in Figure 4-11, where the gprMAX simulation result for 6 NQ size quartz cores with different lengths is compared. It is noticed that for the 5cm length core, the direct arrival and the target reflection are mixed, making identifying the target reflection very difficult. When the core length increases to 10cm, the target reflection is overlapped with the direct arrival and other interfering reflections, but the location of the target reflection becomes recognizable. For the NQ core length from 15cm to 30cm, the target reflection wave from the other side of the core separated from the direct arrival, making the data interpretation less ambiguous.

However, as the core length increases, other reflections will mix with the target reflection since the EM wave path becomes more complicated.

Table 4-7 Summary of the gprMAX simulation result on NQ quartz cores

NQ Core Length	Two-way travel time (ns)	Actual Wave Velocity (m/ns)	Calculated Wave Velocity from the reflection (m/ns)	The error between the calculated velocity to the actual velocity
10cm	1.4923	0.1414	0.1367	-3.46%
15cm	2.2308	0.1414	0.1357	-4.22%
20cm	2.9846	0.1414	0.1347	-4.98%
25cm	3.7231	0.1414	0.1347	-4.95%
30cm	4.4615	0.1414	0.1348	-4.91%

On the other hand, natural fracture and discontinuity exist in the rock mass, and the difficulty in obtaining the rock core from coring drilling increases with the core length. Therefore, the simulation result

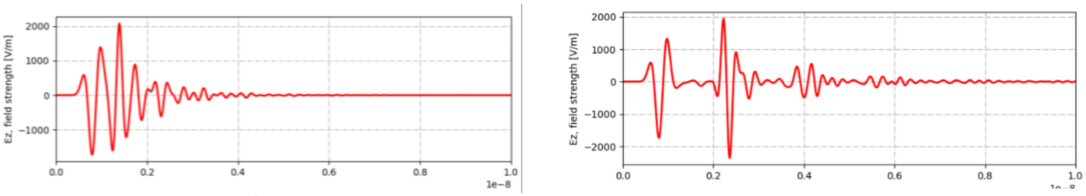

5cm Quartz

10cm Quartz

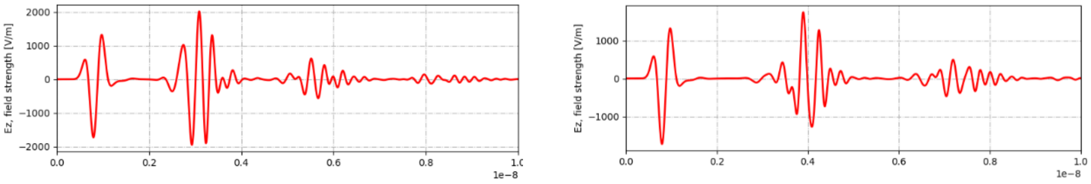

15cm Quartz

20cm Quartz

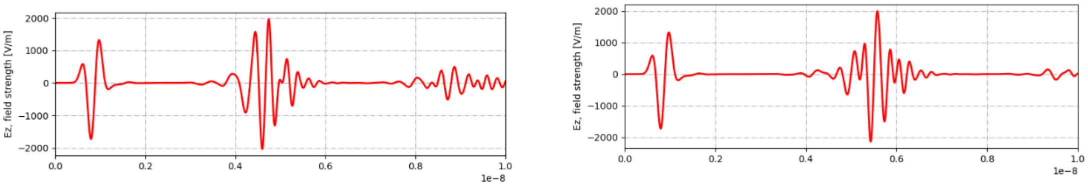

25cm Quartz

30cm Quartz

Figure 4-11 gprMAX simulation result for 6 NQ size quartz cores with different lengths agrees with the lab experiment that the optimum NQ rock core length ranges between 15cm and 30cm. The core length recommendation is safe for most lithologies because the quartz has a relatively low RDP and, thus, high EM wave velocity among general rock types.

In Table 4-7, the calculated wave velocity result of the NQ quartz (10cm -30cm long) is presented. In the simulation, the RDP of the quartz was assigned to 4.5. Thus, the EM wave velocity in the quartz was assigned as 0.1414 m/ns, calculated from Equation 1. It is discovered that the wave velocity calculated from the target reflection wave has a system error of around 5% less than the accurate wave velocity. The reason is expected to be the identification standard of the target. In this study, the location of the reflection (direct arrival and the target reflection) is regarded as the peak of the first half wavelength. In contrast, the half wavelength with very low amplitude is ignored (if any). The other reason is the limited resolution due to the GPR frequency.

The EM wave transmission path in the NQ core over time is studied in detail using gprMAX simulation. Figure 4-12 shows the H-field magnitude transmission at different transmission times. In addition to the direct wave transmission (transmitter- core edge- receiver), part of the EM wave bounces between the side

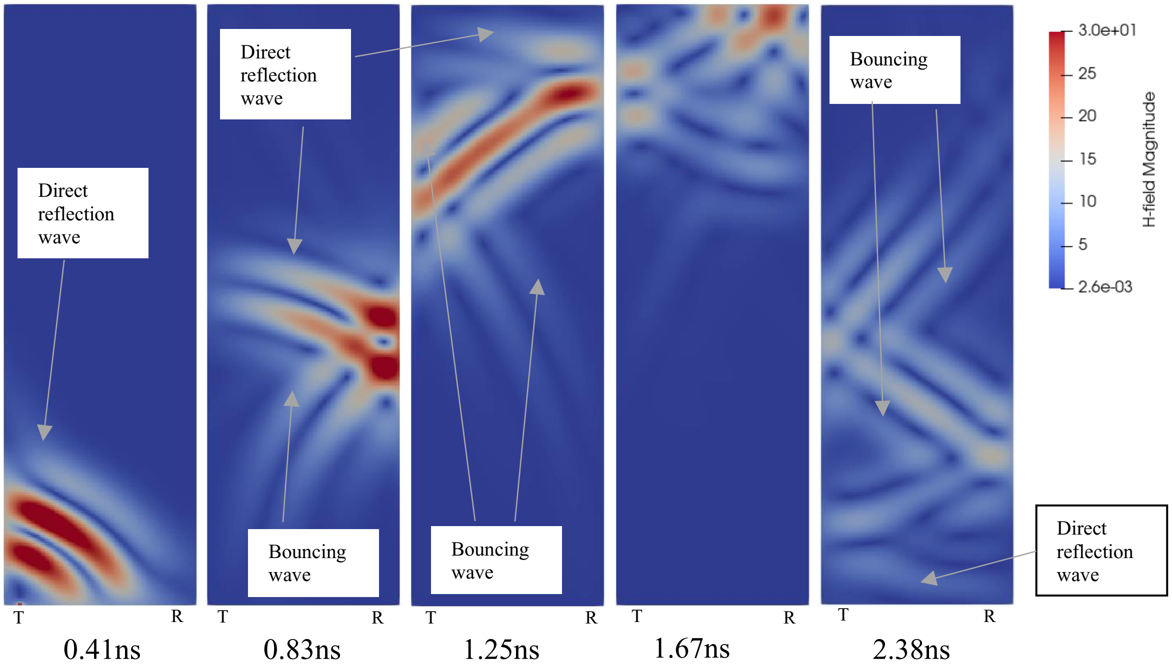

Figure 4-12 EM wave transmission path over time in 15cm long NQ quartz core. The location of Transmitter (T) and Receiver (R) are marked.

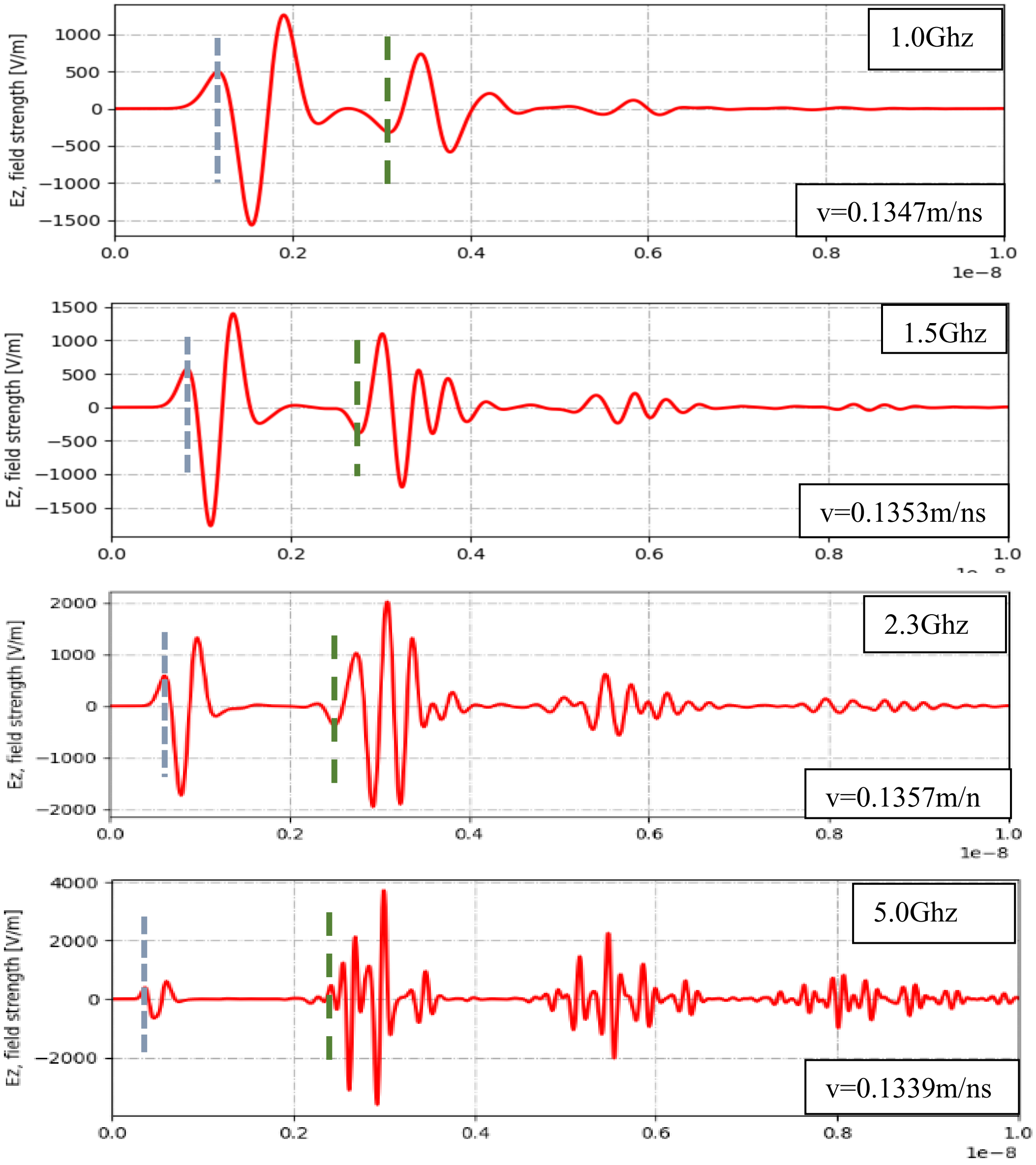

Figure 4-13 The variation of the target reflection time with the variation of GPR frequency, for a 15cm NQ quartz core. The identified target reflection is marked in green dash lines, and the time zero is marked in the grey lines

walls of the core. Two bouncing waves are generated, which arrive at the receiver later than the direct wave transmission. Thus, when identifying the reflection wave from the target core edge, it is essential to pick the first peak of the reflection wave because the direct reflection wave and the bouncing wave mix later, making the identification and interpretation difficult.

By keeping the NQ core length constant at 15cm, different GPR center frequencies (from 1GHz to

5GHz) were applied in the simulation. The wavelet result is shown in Figure 4-13. The identified target reflection is marked in green dash lines, while the time zero is marked in blue dot lines. Although the location of the direct arrival shifts with the GPR frequency, the two-way travel time between the direct arrival and the target reflection almost remain constant with different GPR frequency. For the 1GHz wavelet result, however, the target reflection is on the recognizable margin because of the intrinsic drawback of long wavelength due to the low frequency. It is suggested that with the antenna separation of 40mm, the GPR center frequency should not be below 1.5GHz for the NQ size rock core measurement.

It is noticed that the reflected wave has a higher amplitude than the direct arrival, as shown in Figure 4-11, which does not occur in the reality GPR test. Two reasons are identified from the visualized simulation result in Figure 4-11. First, the wave emitted from the transmitter exhibits different amplitude in different directions. The wave transmitted to the receiver is significantly lower than the wave transmitted through the rock core. This phenomenon is due to the coupling between the antenna and the rock in the simulation modeling. The other reason is that the wave reflected from the edges and corners of the core converges at the receiver; thus, the wave's energy is amplified. This phenomenon arises because of the limitation of the shape of the core. Despite the fact that the reflected wave amplitude is higher than reality, the wave transmission time and path are still reliable for analysis.

4.8 Conclusions

In order to effectively interpret the results of a downhole GPR survey, one of the most important steps is to determine the EM wave velocity of the various rock types as well as their permittivity. This study proposes a practical and rapid method for testing the dielectric permittivity of rock. This technique used a 2.3 GHz GPR system specifically designed for NQ-size cores, one of the more typical rock core sizes used in core drilling. The NQ rock core taken from the field was over one hundred meters long. Quartz (gold vein) and mafic volcanic were the two basic lithologies used to classify the ten different sub-categories (host rocks). Comparisons were made between the RDP result obtained by the GPR system, the open coaxial probe based system and the result found in the literature and the accuracy of the GPR system was demonstrated. The rock sample was subjected to a series of tests to determine its electrical conductivity and magnetic susceptibility. It was found that ignoring the electrical conductivity and magnetic susceptibility of the rock resulted in an average error of 0.79%. Despite the fact that XRD and MLA tests detected pyrite and other metal contents, the rocks in this mining area can still be classified as non-conductive and non-magnetic according to the GPR survey. The RDP for the vein, which is quartz, and the host rock, which is mafic volcanic, were found to be 4.1-4.7 and 6.5-8.6 respectively. It should be noted that the RDP value is measured from dry cores, which has difference from the subsurface rock in the mining zone. The main issue is that the dry core cannot reflect the influence of the groundwater to the rock. The fact that the vein and the host rock have significantly different dielectric properties demonstrates that it is possible to distinguish between the vein and the host using a borehole GPR scan.

The path taken by the electromagnetic waves as they pass through the NQ core was analyzed using FDTD simulations performed in gprMAX. The wave path was found to be convoluted as a result of the reflection on the side of the core as seen. The results of laboratory experiments and simulations were compared to determine the optimal length of the NQ core, which was found to be between 15 and 30 centimeters. This length range is recommended as it is suitable for the majority of lithologies. For a 40 mm antenna separation, it is recommended that the center frequency of the GPR be at least 1.5 GHz. This will help prevent interference from direct arrivals and will also increase the resolution of the measurement.

Chapter 5: Shielded directional mono-hole GPR surveys

The research work of this chapter has been published: Li, Z., Xiao, Y., Pilgrim, R., Royce, J. and Butt, S.D. Subsurface Rock Interface Imaging with the Application of Ground Penetrating Radar (GPR). Proceedings, 72nd Canadian Geotechnical Society Annual Conference; September 29 - October 2, 2019, St. John’s, Canada. Additional information is added in this chapter as supplement in chapter 5.8.

5.1 Co-authorship Statement

Zijian Li: Field Trial, Data Processing, Equipment Manufacture, and Writing Manuscript

Dr. Yingjian Xiao: Support on Field Trial and Data Processing

Rick Pilgrim: Support on Field Trial and Equipment Manufacture

Justin Royce: Support on Field Trial and Equipment Manufacture

Dr. Stephen Butt: Supervision and Reviewing

5.2 Abstract

In this study, ground penetrating radar (GPR) data were collected in field trials both on the surface and downhole. This study aims to evaluate the possibility of identifying the rock interface between gold ore and surrounding rock using borehole GPR. The basic theory of GPR was reviewed before the trials. In surface field trials, the GPR data were collected to identify the rock interface between shale and limestone in a quarry and to identify the rock interface between basalt and rhyolite in cripple bay. In the downhole field trials, the GPR antenna was put in the borehole in the mining site. The GPR imaging result was analyzed with the consideration of the field geometries. Then, the penetration depth and the ability to identify the subsurface structure was evaluated. According to the result, GPR units with the center antenna frequency of 1GHz present a smaller penetration depth than 250MHz GPR, which is 2.5m for surface imaging in homogenous material and 1.8m for downhole imaging. Primary reflections are collected in the results and concur with the field geometries. This study also revealed some problems. The fast traveling speed of the antenna reduced the noise cancelling efficiency and influenced the imaging quality. Unexpected reflections

were found in the result, which may result from a lack of understanding of the field geometry. Overall, 1GHz GPR showed its potential in the downhole imaging application and further work should be done to improve the quality and accuracy.

5.3 Introduction

Ground penetrating radar (GPR) is a popular geophysical imaging technique used for infrastructure imaging, such as soil moisture, archeology and downhole imaging. GPR emits electromagnetic (EM) waves and the delineates the structure using the received echo which is reflected and differentiated by the change of material EM properties. The GPR is an UWB EM wave device which uses a broad range of frequency of 10–5000 MHz and gains its popularity by numerous advantages. For example, the GPR system acquires and processes the signal in real time, and the result can be presented while operation is ongoing. When

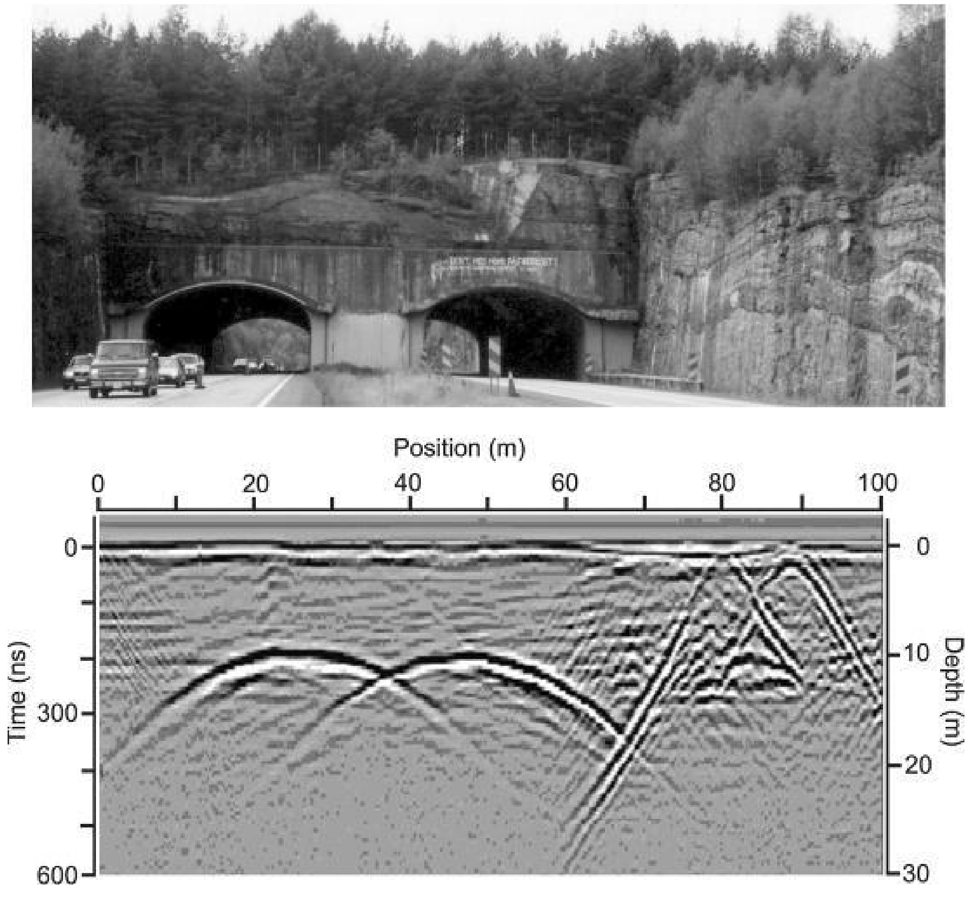

Figure 5-1 GPR cross-section obtained with a 50-MHz system traversing over two road tunnels. (Bristow and Jol, 2008)

different EM wave frequencies are used, the resultant spatial scale ranges from kilometers to centimeters. In addition, GPR is a non-destructive testing (NDT) method which brings no damage to the material.

The adoption of GPR come into existence in the field of geoscience after the mid-1950s (El Said, 1956; Waite and Schmidt, 1961). After 2000, the application of GPR mushroomed due to the development of digital computation and processing ability. Then, the application expanded to more research fields and larger scale imaging practice (Annan, 2002; Bristow and Jol, 2003). Francke et al. (2012) used GPR for the exploration of mineral resources to a large scale. Zaki et al. (2018) used GPR to detect the cavity in karst topography for tunnel construction.

In the Sustainable Mining while Drilling (SMD) project, the gold ore vein is thin and tilted with a dip angle around 70 degrees from horizontal, which increases the difficulty of the ore development. The SMD concept aims at a low dilution, high-efficiency mining process, in which a high-resolution geography imaging method is required. In this study, the target is to evaluate the possibility of the identification of the rock interface between gold ore and surrounding rocks using borehole GPR.

Application of borehole GPR started in the 1970s after the invention of downhole antennas. At first, the target of the borehole GPR is to characterize the fractures, cavity, and property changes in the rock mass for nuclear waste disposal (Olsson, 1987; Olsen, 1992). Then Gilson et al. (1996) used GPR for a smaller scale hydrogeological test. Gregoire et al. (2006) used GPR to check the steam-enhanced remediation in fractured limestone in a time-lapse mode. Mansour et al. analyzed the hydraulic property of the fracture subsurface structure using GPR. Serzu et al. (2004) used GPR to map the natural fracture distribution in the granitic bedrock. Dang et al. (2018) used ultra-wideband borehole GPR detected downhole geometries and proved its accuracy.

In this study, both laboratory and field experiments are conducted to evaluate the possibility of the borehole GPR to delineate the interface between the surrounding rocks and the gold ore. In the laboratory tests, the influence of water and plastic case on signal quality are evaluated. In field trials, the GPR is tested both along the ground surface and downhole to test its maximum imaging depth and the ability to image the rock face.

5.4 Background

The EM properties (ε, μ, σ) dictate EM wave transmission and reflection in the material. Generally, the permittivity ε and conductivity σ are most important, while variations in electron mobility μ are seldom discussed. GPR is most useful in low-electrical-loss materials where the penetration depth is increased. Generally, clay content, saline water, and conductive metal are the primary factors influencing the penetration depth. The penetration depth β is derived for low-electrical-loss materials based on Maxwell equations, as shown in Figure 5-2.

When the incident EM waves are emitted and arrive at a material interface, some of them will reflect back, and others will transmit through this interface to the other medium. Partition of reflected and through-transmitted EM waves can be described using the following reflection and transmission coefficients.

$$R = \frac{Reflected\ Amplitude}{Incident\ Amplitude} = \frac{\sqrt{\varepsilon_1} - \sqrt{\varepsilon_2}}{\sqrt{\varepsilon_1} + \sqrt{\varepsilon_2}} \tag{5-1}$$

$$T = \frac{Transmitted\ Amplitude}{Incident\ Amplitude} = \frac{2\sqrt{\varepsilon_2}}{\sqrt{\varepsilon_1} + \sqrt{\varepsilon_2}} \tag{5-2}$$

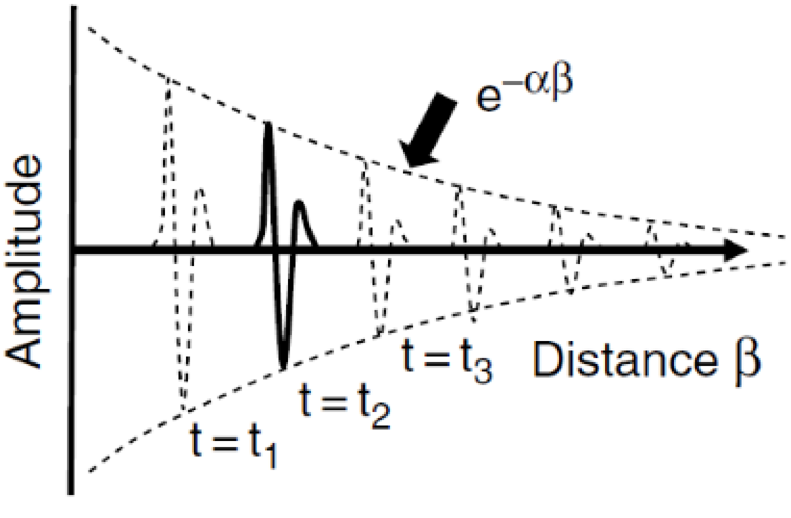

Figure 5-2 EM wave propagates and decays in amplitude with the distance

Where, ε_1 is the relative permittivity of the incoming media, while ε_2 is the relative permittivity of the second media. It is observed that the magnitude of reflected EM waves is dependent on the permittivity difference of rocks about the interface.

5.5 Experiment Instruments

The capability of the GPR systems is tested in this study. The Noggin 1000 MHz GPR unit from Sensors and Software Inc. is used in this study, as shown in Figure 5-3, which includes a GPR unit, a display, a control panel, the battery, and data storage. The GPR unit is 30cm long by 15cm wide and 12cm high. The GPR system is protected in a 3D-printed plastic case when used in a downhole survey, as shown in Figure 5-4.

The data acquired by the Noggin 1000 MHz is collected using the Digital Video Logger (DVL) from Sensors and Software Inc. Then, the data is post-processed using EKKO Project software. The Noggin 1000 MHz has a center frequency of 1000 MHz and a minimum sampling step size of 0.5cm. The Noggin's sampling step size primarily depends on the scanning depth and the stacking number. In the laboratory

Figure 5-3 1GHz Noggin GPR unit

Figure 5-4 Downhole survey with GPR unit protected

experiment and the surface imaging field trials, the minimum sampling step size is used while the stacking number is adjusted by the DVL automatically.

In this study, laboratory and field experiments are conducted to evaluate the possibility of the borehole GPR delineating the interface between the surrounding rocks and the gold ore. The laboratory tests evaluate the influence of water and plastic cases on signal quality. In field trials, the GPR is tested along the ground surface and downhole to test its maximum imaging depth and the ability to image the rock face.

5.6 Ground Surface Field Trial

The GPR field survey is conducted in Conception Bay South Quarry B, Quarry F. Transitions between shale and limestone are observed in these sites. In these tests, shale represents a multiple-layered rock material through which the EM attenuation is higher than homogeneous material.

A 250 MHz GPR unit is also used in the field trial in The Quarry. Then the results of 250MHz GPR and 1GHz GPR are compared. More than 50 data sets in total are collected and analyzed. Typical results are

Figure 5-5 Surficial geology condition of CBS Quarry

further discussed below. As shown in Figure 10, two data sets for the same geometry collected by different GPR units are compared. This line view shows that layered material such as shale greatly influences the GPR penetration depth. Specifically, the 1GHz GPR is unsuitable for layered material imaging due to significant attenuation in wave amplitudes.

5.7 Downhole Field Test

In the studied project, the gold ore vein is thin and tilted with a dip angle of around 70 degrees from the horizontal, increasing the ore development's difficulty. The development concept aims at a low dilution, high efficiency mining process, requiring a high-resolution geography imaging method. In this study, the target is to evaluate the possibility of identifying the rock interface between gold ore and surrounding rocks

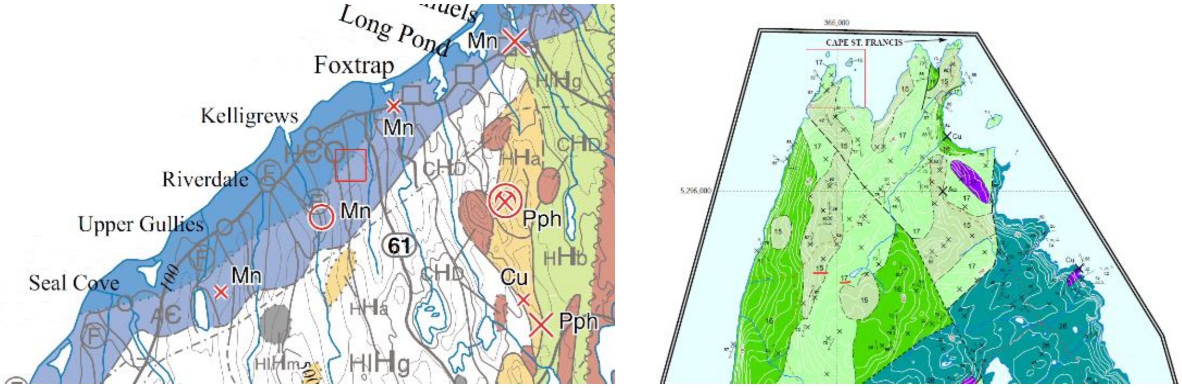

Figure 5-6 Bedrock map of CBS quarry and Cripple Bay

using borehole GPR. In the downhole field test, two 10m deep vertical boreholes with ~9in diameters are

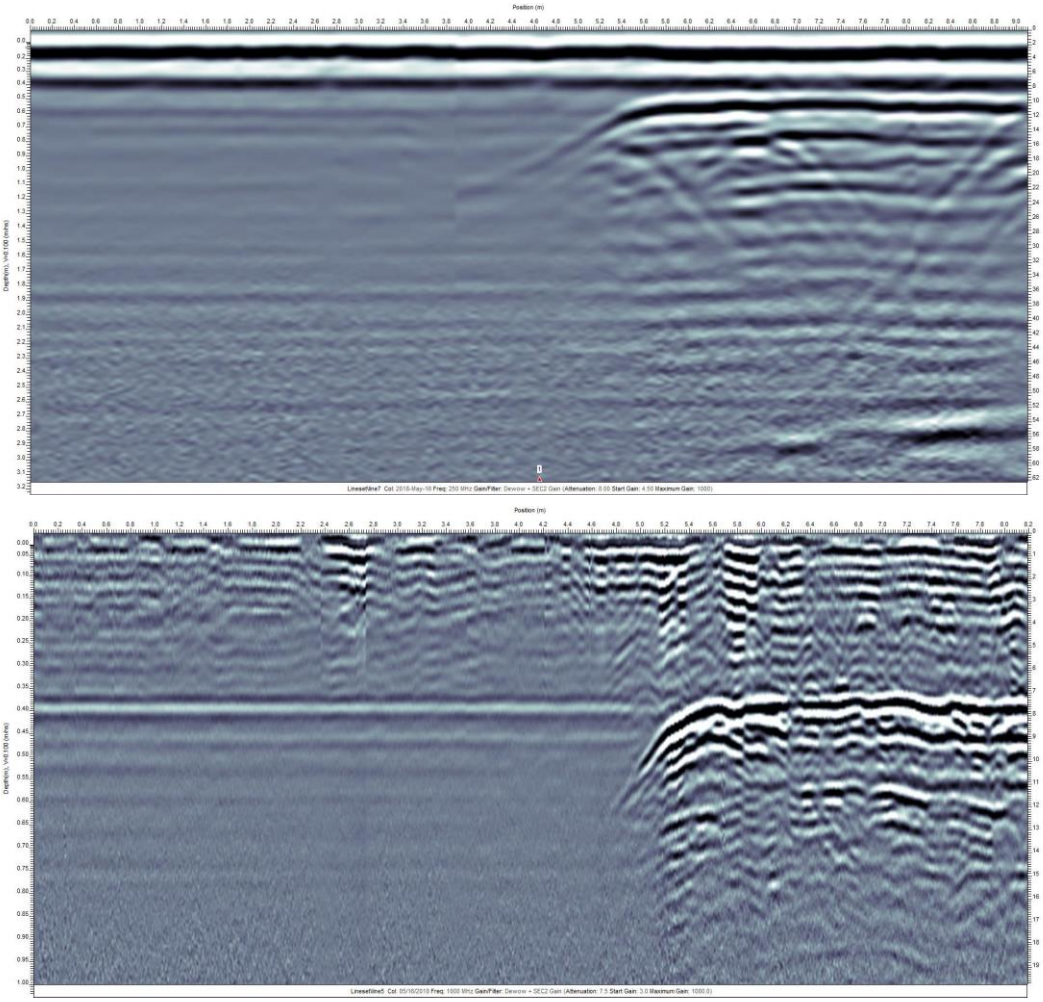

Figure 5-7 Line view result comparison between 250MHz GPR (upper) and 1GHz GPR (lower) in CBS quarry

drilled in the ore zone of the vein. The gold ore vein is quartz, while the surrounding rock is Mafic Volcanic, as shown in Figure 11.A quartz vein outcrop is used as a reference for hole drilling. The thickness of the vein is around 4m, while the dip angle is about 70 degrees (20 degrees from vertical). Hole No.1 is located 1.65m away from the vein outcrop, while hole No.2 is drilled in the middle of the vein, as shown in Figure 12. The outcrop and the hole preparation are shown in Figure 12 below. The total depths of both holes are around 10m. In the field GPR survey, the survey along boreholes reaches the depth of approximately 6m due to the limitation of the length of the data transmitting cable.

Then, using these two holes, the downhole GPR tests are conducted. Different antenna tool face angles are tested because the GPR antenna is shielded, meaning EM waves will be emitted and received in a specific direction. For Hole #1, when the GPR is facing perpendicular to the rock interface and moving upwards, the distance between the rock interface and the GPR increases from 0 m to 1.65m. When the GPR antenna is facing parallel to the vein strike, no rock interface is expected to be shown in the radargrams.

Figure 5-97 Rock cutting samples: Surrounding rock of Mafic Massive Flow (a), quartz (gold ore) (b), and a small layer of Quartz/Altered (c) for cutting analysis

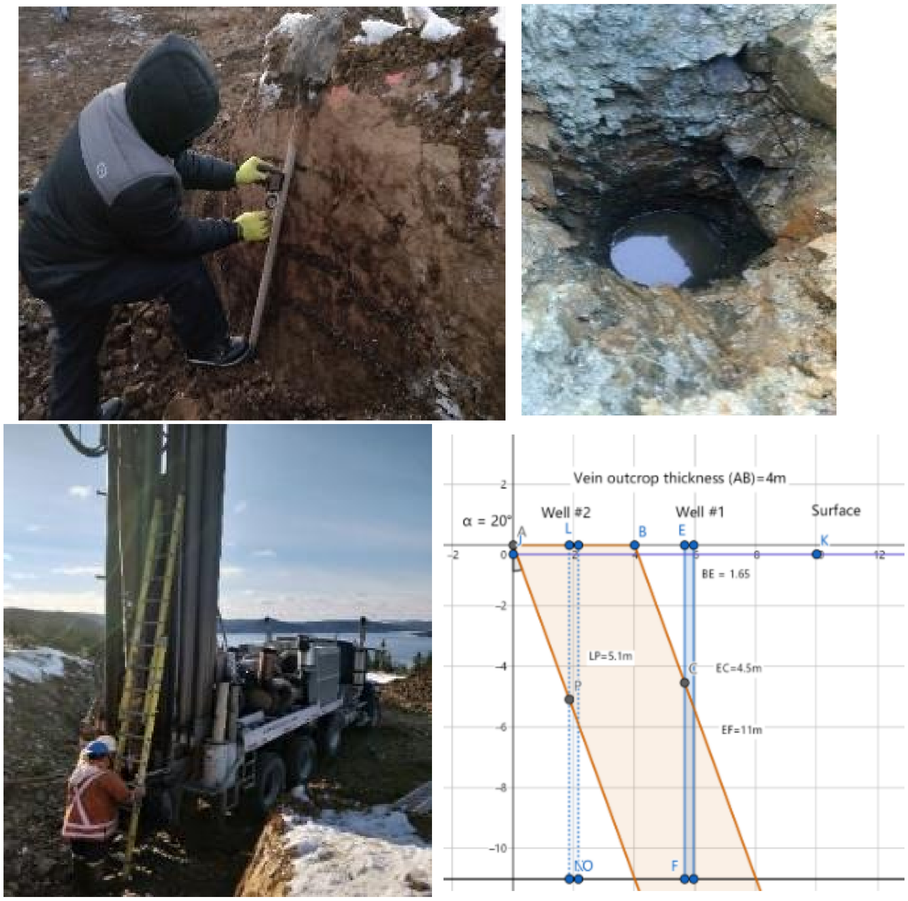

Figure 5-8 Test hole drilling near the vein outcrop and the underground geometry of two holes

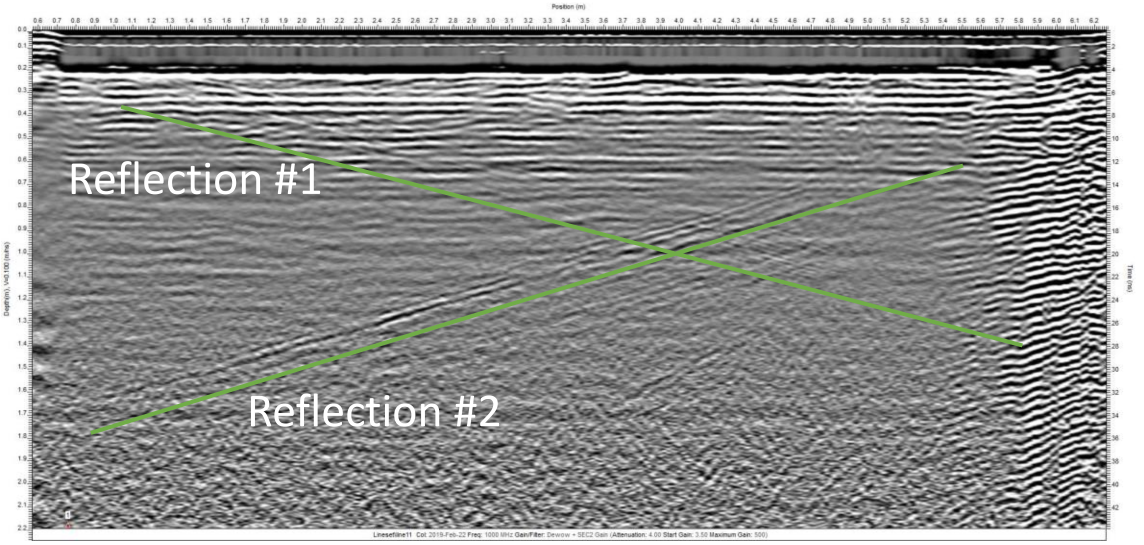

Figure 5-11 The downhole GPR test results in Hole #1

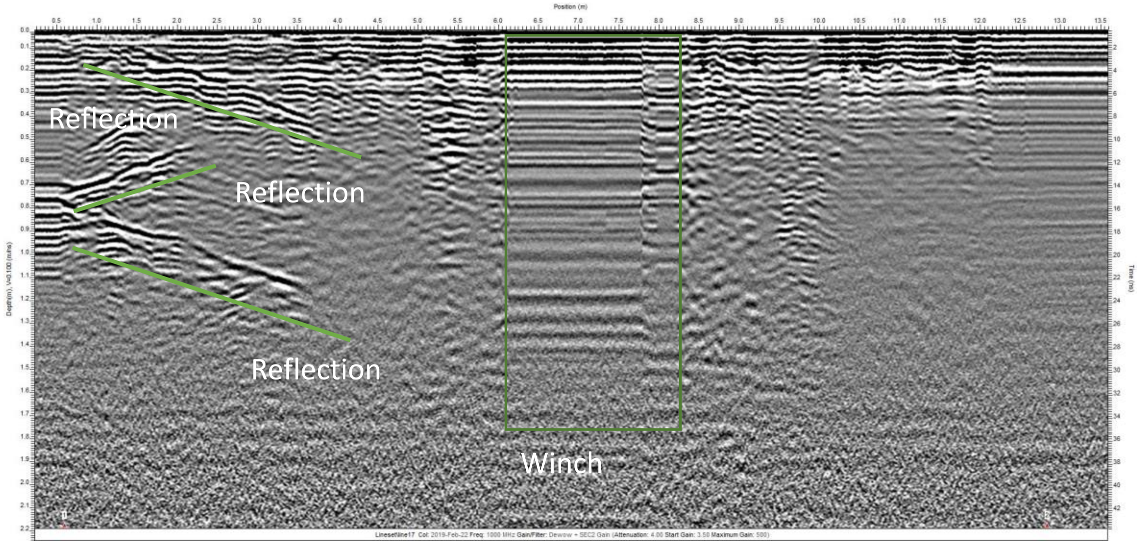

Figure 5-10 The downhole GPR test results in Hole #2

However, the reflection in the borehole may reduce the directional imaging capability. The data quality, however, is influenced by the wellbore's surface reflection and the antenna's directional capability. The test result of hole #1 and hole #2 is shown in Figure 5-11 and Figure 5-10, respectively.

In both holes, multiple horizontal reflections are observed in the downhole GPR radargrams and borehole reverberations. This is generated by the gap between the antenna face and the wellbore wall. Overall, the imaging quality or resolution can be improved by decreasing the speeding of the moving antenna along the borehole, which increases the stacking number with a higher signal-noise ratio. Unexpected reflections are observed for both holes.

5.8 Additional information as supplement (field trial data interpretation)

Based on the results of the previous GPR field test, an extensive post-processing of the data is performed. The goal of this study is to improve the quality and directionality of the data acquired with the Noggin 1GHz GPR in the mining zone field test. The test was conducted in two holes (#1 and #2) with different step sizes and stacking. In each borehole test, line scans were taken 12 times with an azimuth angle interval of 30 degrees.

The GPR antenna was raised using an electric winch. The movement speed of the GPR antenna is fixed due to the design of the motor, which is about 17cm/s. In the configuration of 1cm step size and 2 stacking, or 2cm step size and 4 stacking when using free-run trigger mode in this test, the system speed is automatically set to 25cm/s. In the imaging result, the x-axis position (measurement depth) should be calibrated using the ratio of these two speeds. In the data analysis, the wave speed is 0.1m/ns, which is the typical wave speed for wet rock. Also note that sometimes the winch gets stuck, which can be seen in the image.

Hole #1 is 1.8m from the hanging wall outcrop; 4.5m in the hanging wall and 6.5m in the vein. Hole #2 was drilled in the center of the vein outcrop with 5.0 m in the vein and 4.8 m in the footwall. Overlying gravel is noted above a hanging wall at a depth of 30 cm as shown by the purple line. The angle of the dip of the vein is measured as 67° from the horizontal.

The Hole #2 reflections sampled in the line views at different azimuths are combined and plotted in a 3D figure. The hanging wall and footwall are also plotted in the figure for reference. The blue dots represent the GPR reflection. The reflection is sampled every 5 cm with blue dots. The green mesh represents the hanging wall and footwall. The x-axis is east (positive); the y-axis is north (positive); the z-axis is elevation above surface. The strike of the vein is 30 degrees azimuth. Note that there are some reflections that have the opposite dip angle to the known vein boundary. The possible reason for this is that the antenna shielding is not perfect. So the antenna receives signal from more than its antenna face azimuth. Then the signal reflected from the other azimuth may be projected in an opposite angle of inclination.

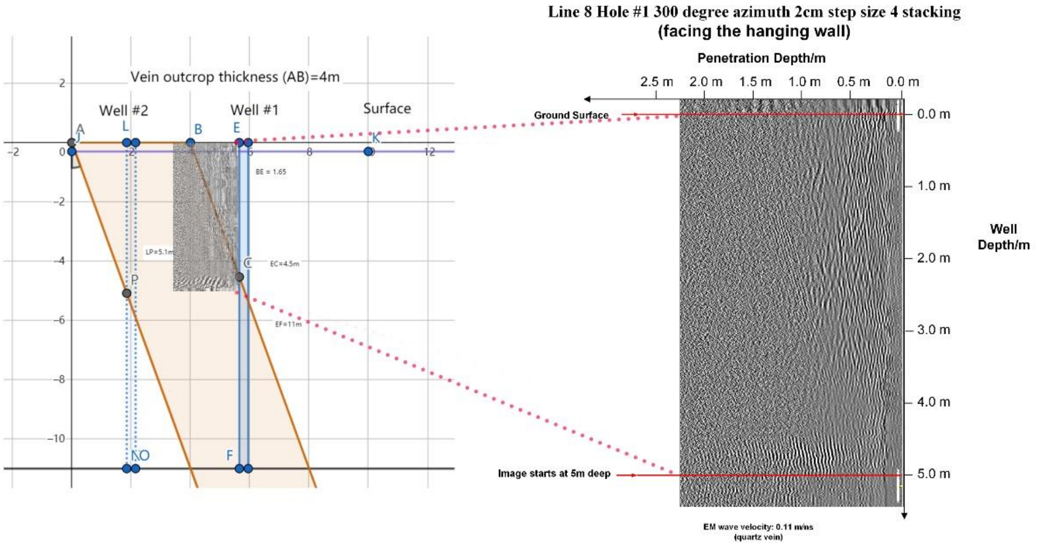

Figure 5-12 Imaging result Hole #1 300 azimuth facing hanging wall

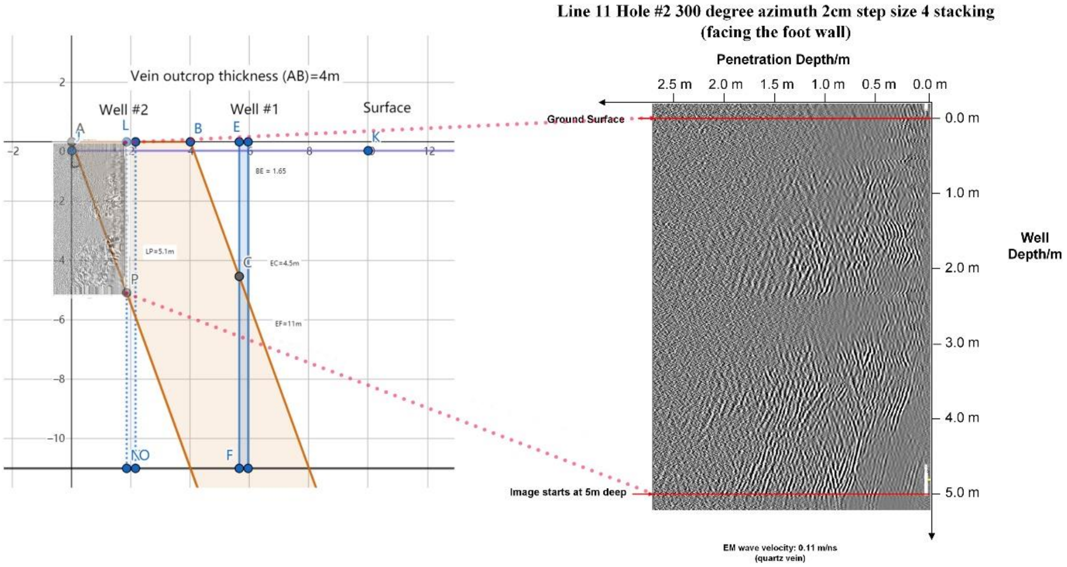

Figure 5-13 Imaging result Hole #2 300 azimuth facing foot wall

Note that there remain several groups of reflections.

Group 1: Two reflections are categorized in group 1. They appear in azimuth 270 degrees and 300 degrees. They are close to the footwall and almost parallel to it, but closer to the borehole. Their depth is from 4.5 m to 0.5 m. It is shown in Figure 5-14. It shows a high potential to be the vein footwall host rock boundary.

Group 2: Two reflections are categorized in Group 2. They appear in azimuth 270 degrees and 300 degrees. They are close to the footwall and almost parallel to it, but further away from the hole. Their depth ranges from 5 m to 3 m. It is shown in Figure 5-15. It shows a high potential to be the vein footwall host rock boundary.

Group 3: Three reflections are categorized in group 3. They appear in azimuth 90 degrees, 120 degrees, 150 degrees. They are almost parallel to the hanging wall but closer to the borehole. Their depth ranges from 5 m to 3.3 m. It is shown in Figure 5-14. It shows a potential to be a sublayer between the borehole and the hanging wall.

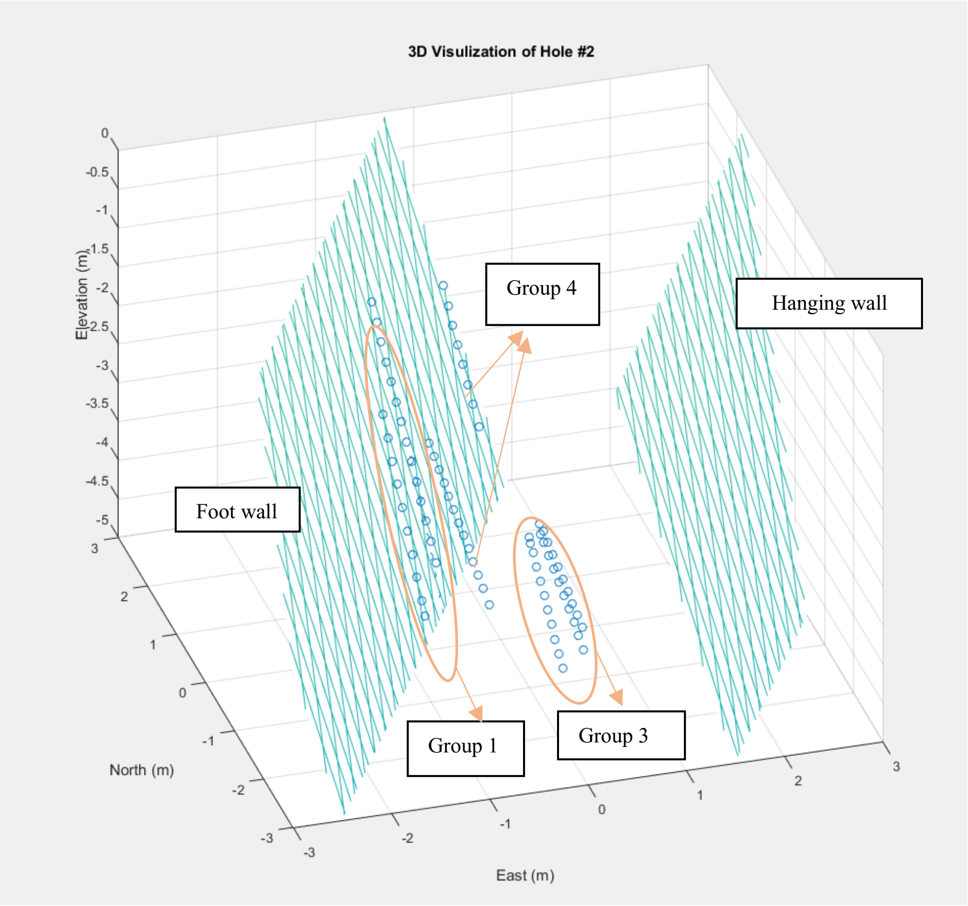

Figure 5-14 Groups of the reflections obtained in Hole #2 (1)

Group 4: Two reflections are categorized in group 4. They appear in azimuth 270 degrees and 300 degrees separately. They are almost parallel to the footwall but close to the borehole. Their depth is from 5m to 3m. They are two single reflections that do not repeat in the nearby azimuth. The reason could be that the amplitude is too weak to be sampled by the near azimuth survey. It is shown in Figure 5-14.

Based on the field trial results and the analysis, we believe that the 1GHz GPR shows potential in downhole imaging. Primary reflection shows a 1.8m penetration depth which is generally satisfactory. Primary reflections concur with the gold ore quartz vein interface and the volcanic mafic host rock. At the same time, some issues will be solved in the future. For example, there are some unexpected reflections collected in the field trials. It is recommended that more geotechnical and geological studies be done before the imaging survey. The image quality is not satisfactory enough due to the limitation of the field equipment. It is suggested that the antenna traveling speed should be small enough to guarantee a high

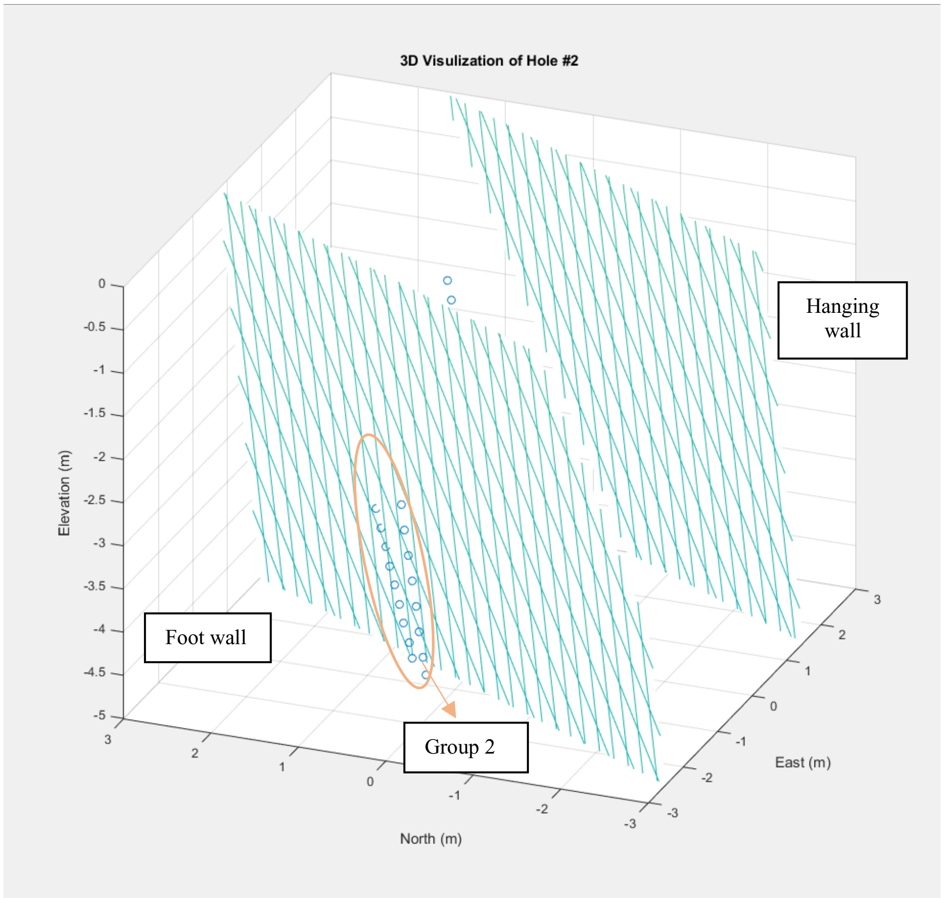

Figure 5-15 Groups of the reflections obtained in Hole #2 (2)

stacking number and thus a high noise-signal ratio. Multiple surface reflections are observed in the images at shallow depth.

The post-processing and 3D visualization improve the data quality of the borehole directional GPR field test in Hole #2. The application of the post-process highlights the plunging reflections and removes the noise. The data sets are then analyzed with reference to the field geometry. At the same time, the imaging results of the nearby azimuth are analyzed and compared.

The result shows that high potential reflections from the footwall are collected by borehole GPR. The reflections are in 300 degree azimuth, which is perpendicular to the footwall. The reflections are not continuous throughout the hole depth. The reason could be that the attenuation of the subsurface formation changes, reducing the strength of the reflected signal. The roughness of the boundary could also affect the continuity of the reflection. The hanging wall does not receive a significant reflection. The main reason is that the distance from the hanging wall to the borehole is greater than the penetration depth of the 1GHz Noggin GPR. There are also reflections with the same angle of inclination from the hanging wall and the footwall, but closer to the borehole. These may indicate a sublayer in the vein.

In the future, amplitude will also be considered for better analysis of GPR directionality. The gap in the amplitude study is that some of the significant reflections are saturated, which means that their amplitude recorded by GPR is at the upper limit of GPR. It is because their actual amplitude is higher than the physical limit of the GPR system. Algorithm study and wavelet analysis could help to recover the actual amplitude of certain reflections. In addition, noise filtering could also be helpful in the amplitude study. Some of the noise will also have a high amplitude that will interfere with the significant reflections.

5.9 Conclusions and recommendations

In this study, GPR data were collected from surface and downhole field tests. A 1GHz GPR unit is used to evaluate its ability to identify rock interfaces between gold ore (quartz) and surrounding rocks (volcanic mafic) in a downhole imaging test. The penetration depth reaches approximately 2 m in the downhole condition. In surface field trials, GPR data were collected to identify the rock interface between shale and limestone in a quarry and between basalt and rhyolite in Cripple Bay. The GPR results are compared with the actual geometries in the field. It is concluded that the penetration capability of GPR is weakened when encountering fractured media such as shale. Through homogeneous media (rhyolite), the penetration depth reaches a maximum of 2.5 m. The interface between basalt and rhyolite is also clearly delineated in the results. The 250MHz GPR is also used in the study and its result is compared with that of the 1GHz GPR. The result shows that the 250MHz GPR unit has greater penetration depth but worse resolution than the 1GHz GPR unit. In addition, the 250MHz GPR unit has a larger size than the 1GHz GPR unit. This requires more space for the 250MHz GPR in downhole imaging.

Underground borehole imaging will be performed using 1GHz GPR. Two holes are drilled at the mine site through the host volcanic mafic and the gold ore quartz. The GPR antenna is hoisted and moved along the hole. Imaging is performed at a series of azimuths. The result is then analyzed with respect to the actual geometry. Primary reflections are found in the result that correspond to the actual rock interface in the test site. The image quality is not satisfactory because the wave signal becomes weaker until it is indistinguishable. Also, the reflection is not consistent in the radargram. The reasons are as follows. First, the natural fractures and multiple layers in the target formation cause a large attenuation of the EM wave amplitudes. Second, the GPR antenna moving speed is high, which limits the number of stacks of data acquisition. Thus, the noise interference is much more than expected. A reflection in the radargram corresponds to the local geometry of the rock interface, while some strong reflections are found that do not correspond to any geometry. It is assumed that these reflections represent some rock interfaces or small layers that have not yet been detected.

Based on the field trial results and analysis, we believe that the 1GHz GPR has potential in downhole imaging. The primary reflection shows a penetration depth of 1.8m, which is generally satisfactory. Primary reflections are found to be consistent with the interface between the quartz gold vein and the volcanic mafic host rock. However, there are some issues to be resolved in the future. For example, there are some unexpected reflections collected in the field tests. It is recommended that more geotechnical and geological studies should be done before the imaging survey. The image quality is not satisfactory enough due to the limitation of the field equipment. It is suggested that the antenna moving speed should be low enough to ensure a high number of stacks and thus a high signal-to-noise ratio. Multiple surface reflections are observed in the images at shallow depths. The algorithm could be improved to remove the surface reflections in post-processing.

Chapter 6: Development of compatible imaging fluid for water-filled boreholes

The research work of this chapter has been prepared for submission to the peer-reviewed journal.

6.1 Co-authorship Statement

Zijian Li: Laboratory Experiment, Data Processing, Numerical Simulation, Field Trial, and Writing Manuscript

Prajit Premraj: Support on Laboratory Experiment and Field Trial

Dr. Stephen Butt: Supervision and Reviewing

6.2 Abstract

The application of borehole GPR in geotechnical exploration has become increasingly popular; however, groundwater in the survey borehole significantly impacts the GPR data quality. It contains non-toxic ingredients (canola oil, barite, and stearic acid) and thus exhibits low environmental impact. In order to solve this problem, a new recipe for imaging fluid was developed. The new imaging fluid has a higher density than water (SG 1.2) and enhances the borehole GPR imaging quality by replacing the groundwater in the borehole. The imaging fluid's ability to stay stable underwater and eliminate groundwater's influence in the borehole was proved through lab tests, numerical simulations, and field trials.

6.3 Introduction

During the past few years, borehole GPR has been used for obtaining geophysical information on subsurface heterogeneity and discontinuity in various engineering and environmental applications.

Hubbard et al. (1997) applied borehole GPR to image the groundwater flow paths in the unsaturated formation. Jung and Kim (1999) observed a GPR wave velocity reduction after the underground construction because the groundwater filled in the rock micro fractures generated by the drill and blasting excavation. Wänstedt et al. (2000) utilized a single borehole GPR system to conduct surveys on the rock fracture network and obtained three-dimensional visualization of the subsurface survey data. Gueting et al.

(2017) conducted a borehole GPR survey to image an aquifer's dielectric permittivity and electrical conductivity and proposed that the full-waveform inversion obtains an increased spatial resolution of the survey on aquifer structures than the conventional GPR ray-based inversion.

Among the variables that could influence the radar signal, the effect of fluids within and outside the borehole is one of the most prominent properties influencing imaging quality. Jol (2008) reported that water significantly attenuates radar wave propagation due to its high RDP. Cassidy (2007) reported increased EM wave energy attenuation due to the increased water conductivity. Then, the spatial/temporal variation in GPR signal attenuation can be used to interpret the potential polluted area hydrological interpretations and evaluate the contaminant properties, saturation index, and bio-degradation processes. Thus, the high RDP and conductivity of the groundwater are the two main reasons for its impact on the borehole GPR imaging quality. Ellefsen and Wright (2005) conducted an FDTD method simulation of borehole GPR. They presented that the groundwater significantly impacted the amplitude of the GPR signal in the borehole according to the radiation patterns. Vogt (2004) reported the impact of conductive groundwater on the borehole GPR imaging quality and suggested that reducing the clearance between the antenna and the wellbore is a viable way to mitigate the influence of water.

Drilling fluid is a heavy, viscous mixture used in the oil and gas drilling to transport rock cuttings to the surface and lubricate and cool the drill bit. The drilling fluid also helps to prevent the collapse of unstable strata into the borehole and the infiltration of water from any water-bearing strata discovered. The drilling fluid's electric properties significantly impact EM surveys conducted in the borehole (Jannin et al., 2014). By adopting the concept of drilling fluid, it is viable to propose a fluid to fill the borehole and solve the problem brought by the groundwater.

The relative dielectric permittivity of water is very high (81) compared to soil and rock (between 4 and 10) encountered in the borehole radar survey. As a result, a large amount of the wave energy will bounce back from the water-wellbore interface, which becomes a significant noise interfering with the radar imaging quality and also induces a reduction in the penetration depth of the radar wave. Besides, the groundwater also strongly attenuates the radar wave because of its polarity characteristics, and the dissolved salt increases the electric conductivity. Thus, the attenuation of the radar wave increases.

The drilling fluid can be categorized into three sorts: Water-Based Mud (WBM), Oil-Based Mud (OBM), and drilling fluids that comprise gas, aerated mud, or aqueous foams (Khodja et al., 2010). In order to achieve the goal of low dielectric permittivity and low electric conductivity, the OBM is considered an ideal solution to the groundwater problem for the borehole GPR. OBM was created for cases where WBM was considered insufficient, for example, in shale formations with lower stability. Traditional OBM uses direct petroleum refining products such as diesel or mineral oil as the fluid base. Synthetic-Based Mud (SBM) is introduced based on the traditional petroleum-based OBM to mitigate the environmental effect and comply with environmental regulations. The fluid base of the SBM is synthetic organic compounds (olefins, esters, or linear alkyl benzenes). The organic compounds are distributed in brine with other ingredients such as emulsifiers, wetting agents, and a weighing substance to make an emulsion. SBMs are specifically designed to be free of Polycyclic Aromatic Hydrocarbons (PAHs), resulting in a lower environmental impact and toxicity for the personnel.

Research has been proposed to utilize vegetable oil as an insulating fluid that has received several inputs (Abdelmalik, 2014; Umar et al., 2018). Vegetable oils are renewable as well as biodegradable. Vegetable oils can be used as dielectric fluids in high-voltage systems (Hamid et al., 2014; Umar et al., 2018).

In this study, a fluid recipe was developed to solve the groundwater problem on the borehole GPR signal quality based on the concept of SBM by replacing the groundwater in the borehole. This new fluid recipe is called imaging fluid. Only natural low-toxicity materials were used to ensure the imaging fluid was environmentally friendly. The dielectric permittivity and the electric conductivity of the imaging fluid complied with the borehole GPR requirements. A series of laboratory tests and field trials were conducted to validate the compatibility of the imaging fluid with the borehole GPR.

6.4 Physics of Dielectric Permittivity and Conductivity

Local redistribution of bound charges to new equilibrium positions occurs when an electric field is applied to a material. Polarization is the name given to this phenomenon of charge redistribution. Dipolar polarization occurs when molecules with a permanent electric moment are oriented along an applied field. This sort of polarization is typical in heterogeneous materials such as porous rocks saturated with various fluids (Cho et al., 2022). The pore structure's bound water molecules and the solid permittivity influence the dielectric response. When there is no dissipation of the energy carried by the electric field in the medium, the relative permittivity of a formation is a real number. When the formation dissipation is considered, its relative permittivity becomes a complex number as given below:

$$\varepsilon = \varepsilon' + \varepsilon'' \tag{6-1}$$

Where, ε is the relative permittivity, ε' is the real part and $\varepsilon''$is the imaginary part. In this study, the material dissipation is not taken into account, and only the real part of the dielectric permittivity is discussed. Dielectric permittivity significantly influences the energy of the wave reflected back from the interface between two materials since it determines the EM wave impedance of the material. The smaller the dielectric permittivity difference between the media in the borehole annulus and the rock formation, the less EM wave energy will be reflected back, and the better the borehole GPR signal-to-noise ratio will be.

For the GPR EM wave, the wave impedance is calculated as follows:

$$Z = \sqrt{\varepsilon} = \left(\frac{c}{v}\right)^2 \tag{6-2}$$

Where, Z is the EM wave impedance, ε is the RDP (dimensionless), v is the EM wave velocity in the rock media (m/ns), and c is the speed of light (~ 0.3m/ns).

The power of the incoming wave is

$$Z = \sqrt{\varepsilon} = \left(\frac{c}{v}\right)^2 \tag{6-3}$$

The power of the reflected wave is:

$$P_{ref} = \left(\frac{Z_1 - Z_2}{Z_1 + Z_2}\right)^2 P_{in} \tag{6-4}$$

The power of the transmitted wave is:

$$P_{trans} = \frac{4Z_1Z_2}{(Z_1 + Z_2)^2} P_{in} \tag{6-5}$$

Where, A_I is the amplitude of the incoming wave, P_{in} is the power of the incoming wave, P_{ref} is the power of the reflected wave, P_{trans} is the power of the transmitted wave, Z_1 is the impedance of the first media, and Z_2 is the impedance of the second media.

Electrical conductivity measures a material's ability to transport a current or the amount of electrical current it can carry. Specific conductance is another name for electrical conductivity. Conductivity is a material's inherent property. Electrical conductivity is denoted by the symbol σ and is measured in Siemens per meter (S/m) in SI units. The Greek letter κ is utilized in electrical engineering. The conductivity influences the EM wave attenuation in the media if the media is redeemed as a conductor ($\sigma/\omega\varepsilon \gg 1$), where σ is the material conductivity, and ω is the angular frequency of the wave. The wave (propagating in the x-direction) solution to Maxwell's equations in a conductive media can be expressed as:

$$E = E_0 e^{(-\beta x)} e^{[i(\alpha x - \omega t)]} \tag{6-6}$$

The value of β depends on the conductivity and frequency of the wave. When the media is recognized as a conductor,

$$\alpha \cong \beta = \sqrt{\frac{\omega\mu\sigma}{2}} \tag{6-7}$$

6.5 Imaging fluid characterization

The specific gravity of the imaging fluid was measured using the graduated cylinder. When using the optimum recipe, the specific gravity is determined as 1.2. The conductivity of the imaging fluid was measured by a conductivity meter. The conductivity of the imaging fluid was lower than the measurement limit of the conductivity meter, so the conductivity can only be characterized as <0.001mS/cm, but this conductivity was much lower than natural water. In comparison, the tap water conductivity in the Memorial University of Newfoundland was measured as 1.5mS/cm, which is more than 1500 times higher than the imaging fluid.

The dielectric permittivity of the imaging fluid was calculated theoretically and measured from the lab test. Lichtenecker's formula is adopted, which is the most appropriate for calculating the average permittivity of the mixture. It is a theoretical model derived from the effective medium theory (EMT) (Zheng et al., 2005).

$$-log\varepsilon_{mix} = \sum_{i=1}^{N} v_i log\varepsilon_i \tag{6-8}$$

Where, ε_{mix} is the complex permittivity of a mixture of N phases, and ε_i and v_i are the complex permittivity and volume fraction of the i_{th} phase, respectively.

In the lab test, the RDP of the pure canola oil and the imaging fluid were calculated using the GPR reflection test. The test fluid was poured into a glass tank. A 1GHz shielded surface GPR system was applied on one side of the tank. On the other side, aluminum foil was attached to the tank's inner surface,

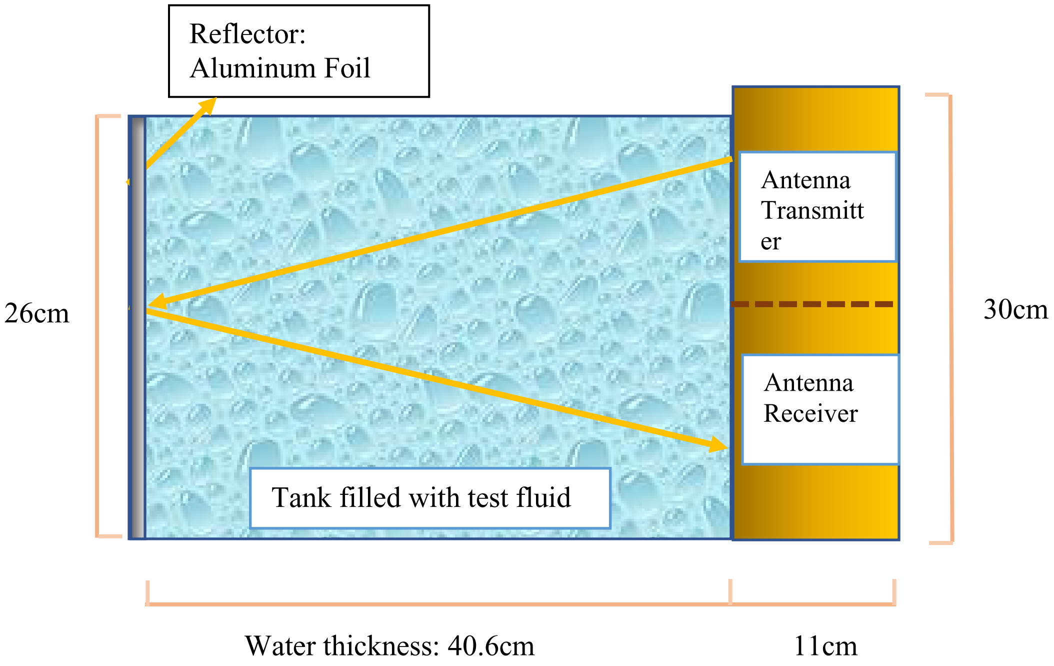

Figure 6-1 Canola oil and imaging fluid RDP measurement using GPR reflection

serving as the reflection target. Considering the tank's length and the GPR antenna's separation, the EM wave velocity transmitting through the test fluid was calculated. Then the RDP of the fluid was derived from the EM wave velocity. The RDP value of the canola oil was calculated from the lab test, and the result agreed with the literature value. The RDP of barite and stearic acid were obtained from the previous study. The theoretical calculation and test results of the canola oil and the imaging fluid RDP are given in Table 6-1. The error between the calculation based on Lichtenecker's formula and the test measurement result was less than 1.2%, which indicated that the RDP of the imaging fluid could be regarded as approximately 2.7-2.73 measured at 1GHz frequency. The reason for the error was that the resolution of the 1GHz GPR was limited and that the literature value of the RDP of each ingredient used in the calculation did not exactly agree with the value of the material in reality.

Table 6-1 Density and RDP of each ingredient and the imaging fluid mixture

	VOLUME FRACTION	RDP	DENSITY
CANOLA	85.41%	2.5 (Latif et al., 2015)/ 2.4 (Test)	0.9
BARITE	9.25%	8 (Rosenholtz and Smith, 1936)	4.2
STEARIC ACID	5.34%	2.7 (Agarwal and Ichijo, 1977)	0.8
MIXTURE	100.00%	2.700 (Calculation)/ 2.731 (Test)	1.2

In the test result, the fluid stays stable for more than one day after being poured in water at 0 ~ 50 Celsius degrees. With the temperature decrease, the stability increases while the viscosity also increases accordingly. At 0 Celsius degree, 3g/100ml stearic acid concentration also stayed stable for more than 20 hours. For the operation in July, it is recommended that the 5g/100ml stearic acid concentration should be used. For example, in 17.7 L fluid, there is 13.61kg (15.1 L) canola oil, 6.88 kg Barite, and 756g stearic acid.

All these three components have no toxicity and do not react with water. Canola oil is an economical choice that does not dissolve in water and has an appropriate RDP (2.4). Barite is not chemically reactive and has a high density which could modify the density of the imaging fluid. Stearic acid can only dissolve in water but not in oil; it increases the oil's viscosity when the temperature decreases.

The impact of the groundwater on the borehole GPR signal quality has not been widely discussed yet. In order to access the properties of the imaging fluid, the imaging fluid is compared with the groundwater from the mining site, WBM and OBM, as shown in the Table 6-2. It is suggested that the groundwater and the WBM have high conductivity and high RDP, due to the high water and salt content. The OBM provides appropriate RDP depends on the water/oil ratio, but the conductivity is higher than the groundwater due to its application of additives. The WBM and OBM both has toxicity since the additives are used to mix water and oil phase, to modify the rheology, or to modify other properties.

Table 6-2 Comparison between the groundwater from the mining site, WBM and OBM and imaging fluid

	Groundwater in mining zone	WBM (Parizad & Shahbazi (2016))	OBM Jannin et al. (2014)	Imaging Fluid
Density (g/cm^3)	1	>1	0.96-1.8	1.2
RDP	81	~81	3.5-14	2.7
Conductivity (m/S)	0.031	7	0.02	<0.0001
Toxicity	N/A	Toxic	Toxic	Very low toxicity

6.6 Laboratory experiment – GPR test of imaging fluid in the borehole simulator

This study tested three different media in the borehole simulator: air, tap water, and the new imaging fluid. The borehole simulator is 4 inches diameter pipe, which was filled with certain media during the test. The antenna was placed in the middle of the pipe. The target is the metal container, which reflects almost 100% of the EM wave energy. The distance between the antenna and the container is 4.5m to avoid potential interference. In each survey, three rotations were performed with the high point towards the container at the beginning. The geometry is shown in Figure 6-2.

In this test, the transmission media has two parts. The first part is the annulus between the borehole

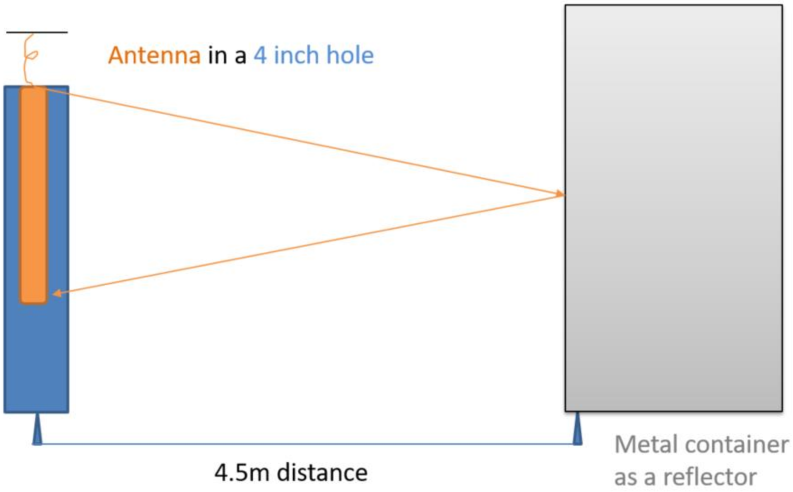

Figure 6-2 Experiment layout for the imaging fluid using borehole GPR

wall and the antenna, which is the media to be tested. The other part is the air. Although the air has different relative dielectric permittivity compared to the rock, the difference between imaging fluid and the water can still be evaluated here.

The experiment shows that the air (dry hole) and the imaging fluid obtained acceptable imaging quality, while the imaging quality of the tap water was very ambiguous. Thus, the capability of the imaging fluid to enhance the borehole GPR imaging quality is proved. The test result is shown in Figure 6-3, Figure 6-4,

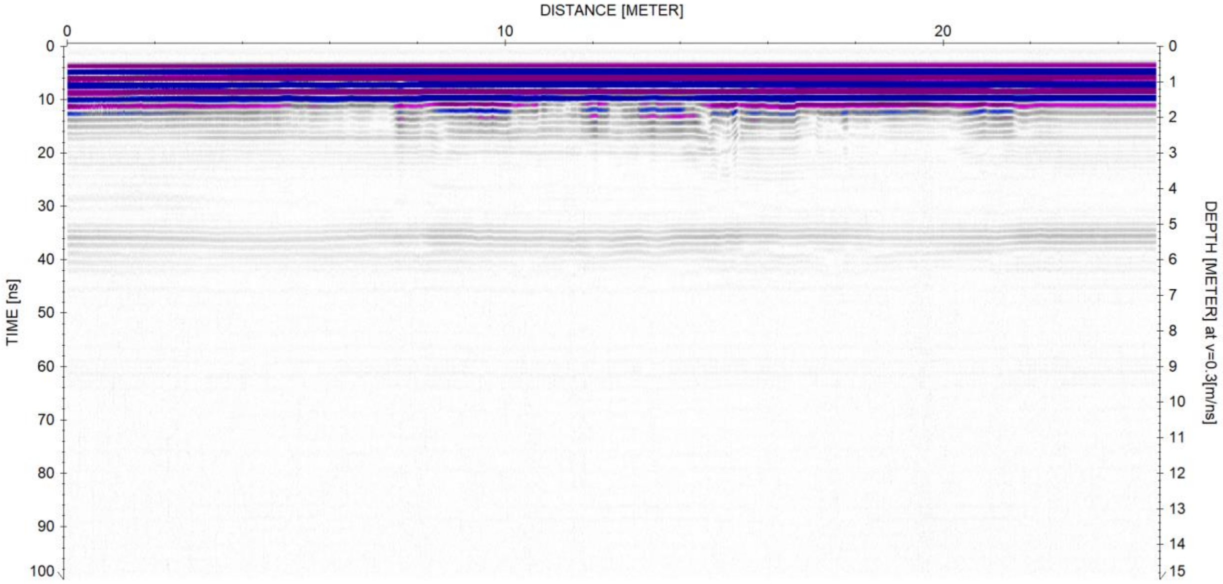

Figure 6-3 Borehole simulator GPR result with air media

and Figure 6-5

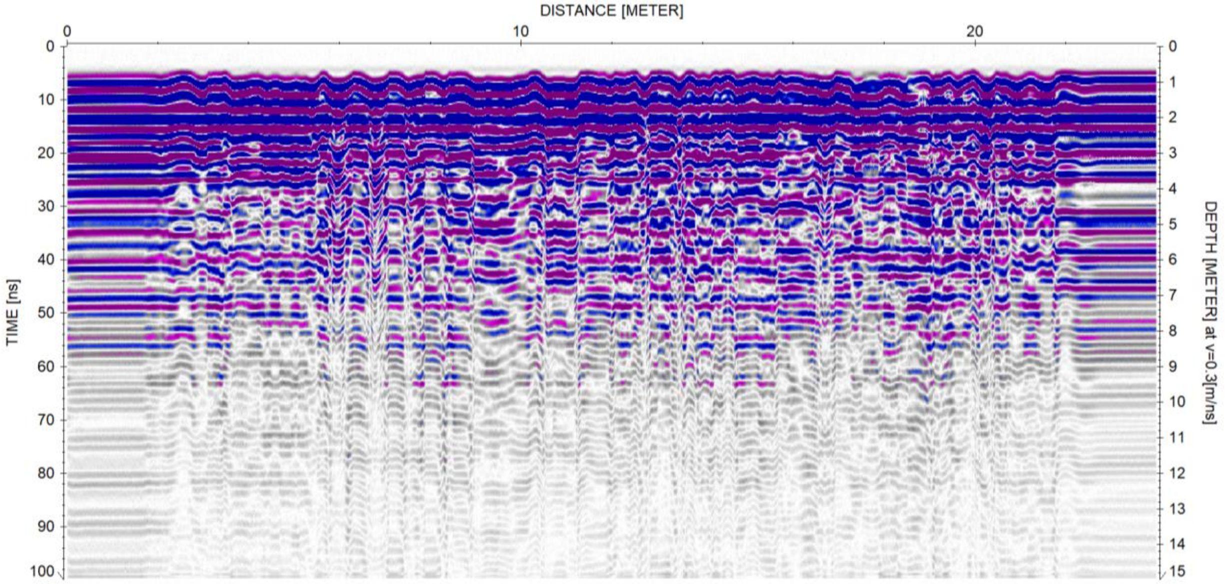

Figure 6-4 Borehole simulator GPR result with water media

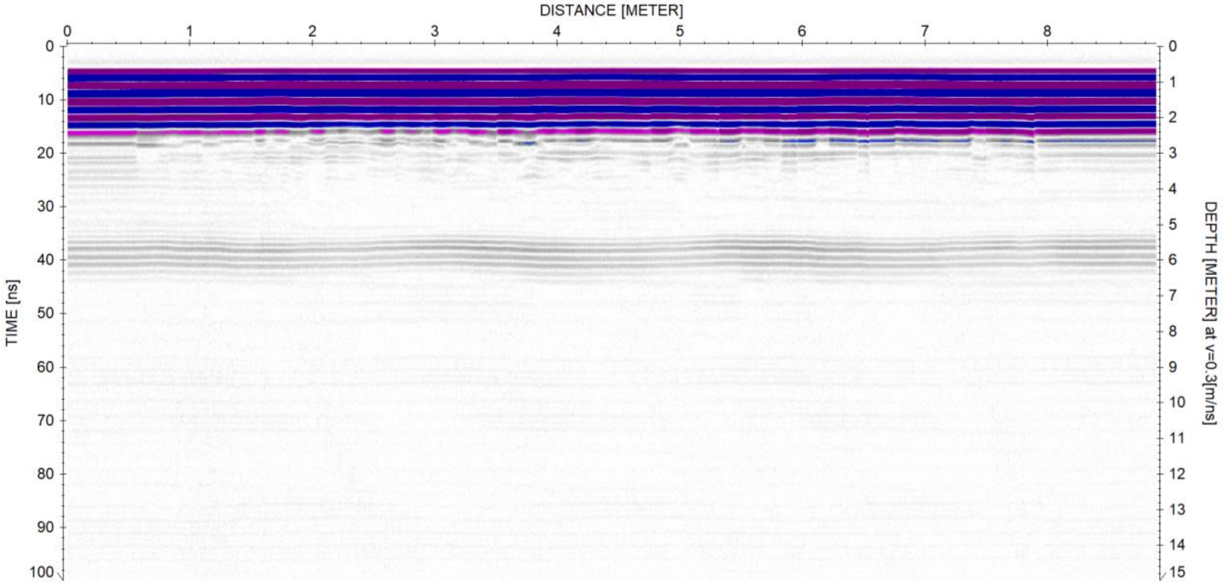

Figure 6-5 Borehole simulator GPR result with Imaging fluid media, a survey conducted 1 hour after the borehole was filled with water

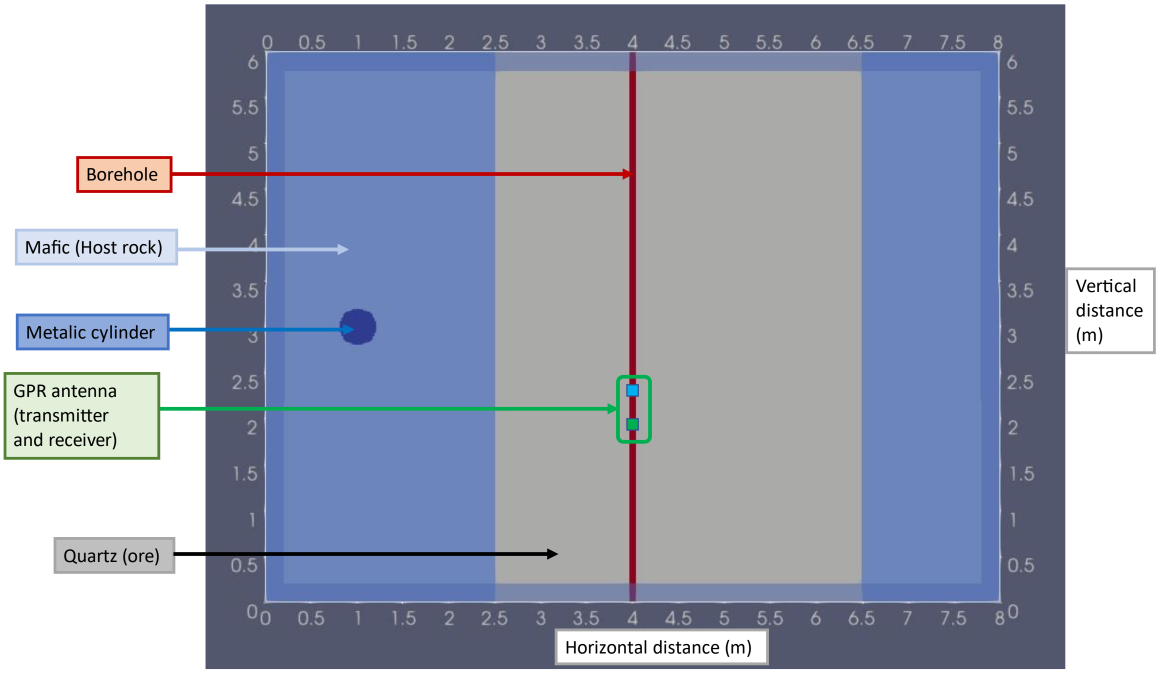

Figure 6-6 gprMAX simulation layout for the imaging fluid application in the field

6.7 Simulation of the borehole GPR with different fluids in the wellbore

In this study, the 2D simulation is conducted through gprMAX software. The geometry is constructed with a tilted borehole in the center of an ore vein. Different fluid media will be applied in the model to compare the imaging quality. The imaging quality will be evaluated regarding signal amplitude, noise level,

and unexpected noise or reflection. This simulation work will examine the imaging fluid effectiveness in a more realistic geometry.

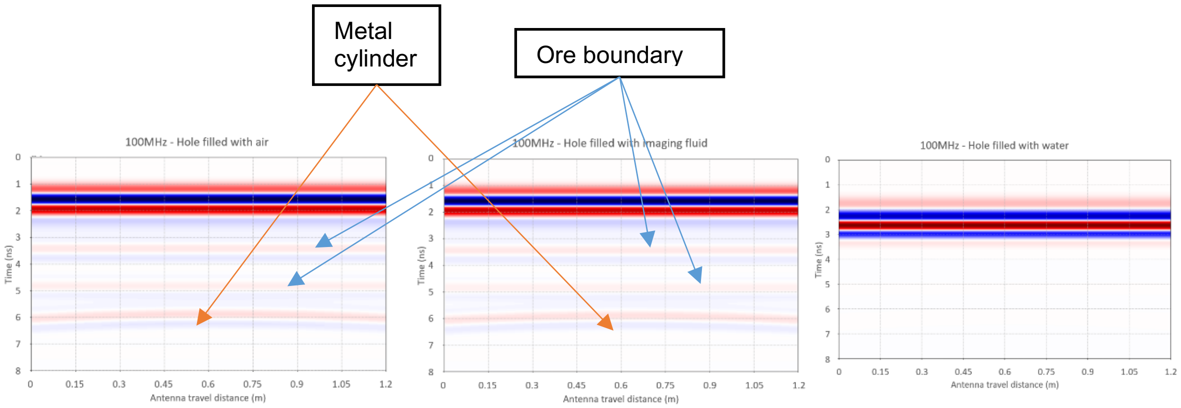

Figure 6-7 Borehole GPR simulation result comparison in 8cm diameter hole and 100MHz GPR

In the gprMAX simulation, with 500MHz GPR center frequency, different borehole media conditions are tested and compared. With the 8cm borehole diameter, the result of air, water, and imaging fluid are compared below:

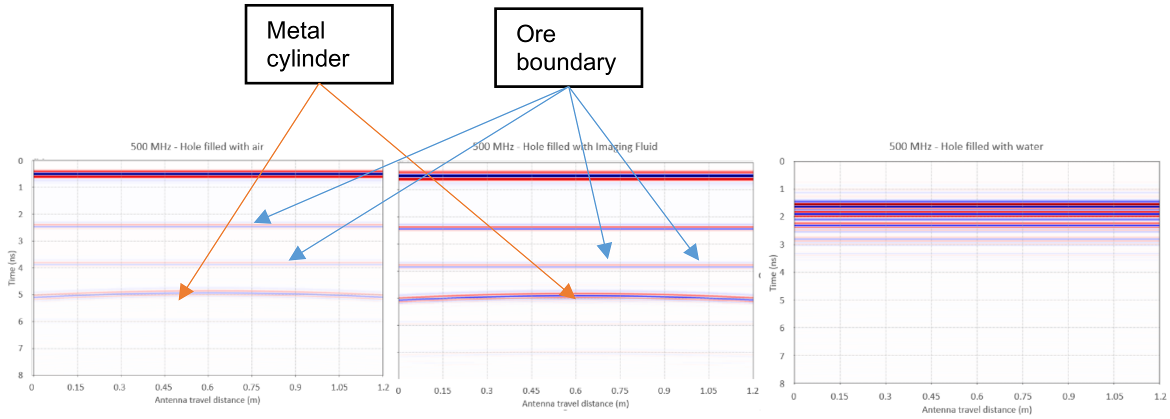

Figure 6-8 Borehole GPR simulation result comparison in 8cm diameter hole and 500MHz GPR

It is noticed that both the air and imaging fluid filled holes presented excellent GPR imaging quality. The signal-to-noise ratio is very high, and no visible noise interference impacts the target reflection. The imaging fluid also achieved a higher reflection energy than the air, because of the appropriate RDP value design of the imaging fluid. When it comes to the water filled hole, the target signal and the noise are totally mixed and impossible to be interpreted, due to the inappropriate RDP value of water.

The same conclusion can be drawn for the 100 MHz GPR situation as it can for the 500 MHz GPR: both the air and imaging fluid filled hole displayed excellent GPR imaging quality, and the imaging fluid also achieved higher reflection energy than the air due to the proper RDP value design of the imaging fluid. Due to the water's incorrect RDP value, the target signal and noise in the water-filled hole are completely intermingled and hard to understand.

6.8 Field trial of the borehole GPR using imaging fluid

The imaging fluid will be tested in the NQ size hole in the mining site, together with the 500MHz borehole GPR system. The imaging quality of different media will be compared to prove the capability of the imaging fluid. The result is shown in Figure 6-9.

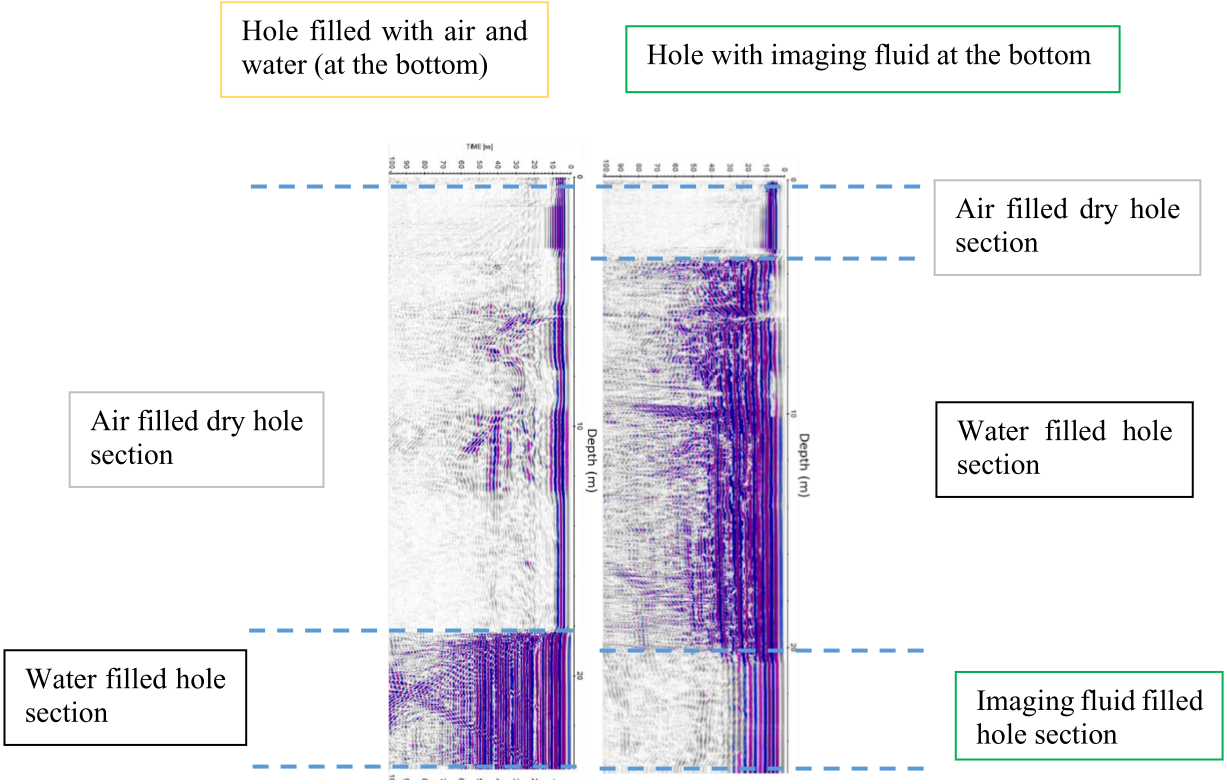

Figure 6-9 The field trial result: the imaging quality of water, air, and imaging fluid

Two results from the same NQ size borehole in the field trial above are compared. On the left, the groundwater in the borehole was pumped out from the surface to 18.5m deep. On the right, imaging fluid was poured into the borehole, covering from the bottom to 20.4m deep, while water covered from 3.5m to 20.3m deep. It was observed that in the dry hole, the signal quality was satisfying with a low noise level. The noise level in the groundwater-filled interval was very high, which overwhelmed the target's significant reflections. Both horizontal noise and tilted noise were presented. When imaging fluid was applied, the noise level was significantly reduced compared to the groundwater-filled condition. Although the near antenna region has horizontal noises, the far field (>30ns) was not influenced by the horizontal noise. The horizontal noise was expected to be the amplified direct arrival. The reason is likely that the groundwater was not totally displaced by the imaging fluid, with a thin layer of water left between the imaging fluid and the wellbore. Overall, the field trial result of the imaging fluid proved its capability to enhance imaging quality.

6.9 Conclusions

In this study, a new recipe for imaging fluid was presented. The imaging fluid was aimed to replace the groundwater in the borehole before the borehole GPR survey and enhance GPR signal quality. The imaging fluid recipe involved canola oil (fluid base), barite (density moderator), and stearic acid (viscosity improver). Through the lab test, the imaging fluid was characterized with appropriate RDP (~2.7), very low electric conductivity (<0.001mS/cm), density (1.2 g/cm^3), and good stability underwater. A series of lab tests, numerical simulations, and field trials were conducted. It was proved that the imaging fluid solved the borehole GPR signal problem due to the groundwater in the borehole by replacing it. In the field trial, the high-level noise of the borehole GPR survey caused by the groundwater was confirmed, and the GPR signal quality significantly enhancement was observed one day after the imaging fluid was poured in and filled the borehole, compared to the groundwater-filled borehole. It was concluded that the imaging fluid could successfully enhance the borehole GPR in the water-filled borehole.

As a practical solution for the field application of the borehole GPR, the new fluid possesses these four advantages:

a) Appropriate relative dielectric permittivity and low attenuation coefficient

The relative dielectric permittivity of the new imaging fluid is around 2.7, while that of the soil and rock ranges between 4 and 10, and that of water is 81. Thus, after substituting the groundwater with the imaging fluid, the corresponding energy of the reflected wave from the imaging fluid-wellbore interface takes 0.96%~ 9.99% (depending on the formation lithology) of the initial wave energy. In comparison, 23.04% to 40.50% of the energy will reflect if the borehole is filled with groundwater. As a result, the signal-noise ratio increases, and the imaging quality is improved. In addition, the attenuation coefficient of the imaging fluid is much lower than that of groundwater because the imaging fluid can be regarded as an isolator. Then, the signal amplitude will increase accordingly.

b) Higher density than water

The imaging fluid provides a higher density (1.2g/cm^3) than water (1.0g/cm^3). This feature allows the imaging fluid to settle on the bottom of the water-filled wellbore. When the borehole GPR is tripped into the wellbore for the survey, the imaging fluid will replace the groundwater at the wellbore bottom, encapsulate the borehole GPR and enhance the imaging quality. Besides, the high density of the imaging fluid results in a higher pore pressure than groundwater, which prevents groundwater from flowing into the wellbore after being applied.

c) Stability underwater

The imaging fluid is fabricated with the novel recipe, which enables the imaging fluid to reach the bottom of the water-filled wellbore and remain stable for more than one month. This long period of stability provides the borehole GPR survey with a wide time window to operate, making the field application of the imaging fluid practical.

d) Non-toxicity recipe

The recipe of the imaging fluid only includes gradients made from natural materials. This eliminates the possibility of the existence of materials harmful to the operating personnel.

Chapter 7: Determination of the formation properties from LWD measured rotary percussion drilling data

The research work of this chapter has been published: Li, Z., Kyzym, I., Qiu, H., and Butt, S.D. Determination of the formation properties from Rotary Percussion Drilling data, Proceedings 72nd Canadian Geotechnical Society Annual Conference; September 29-October 2, 2019; St. John's, Canada.

7.1 Co-authorship Statement

Zijian Li: Field Trial, Data Processing and Writing Manuscript

Igor Kyzym: Support on Field Trial and Data Processing

Dr. Hongyuan Qiu: Support on Data Processing

Dr. Stephen Butt: Supervision and Reviewing

7.2 Abstract

This research aims to investigate the potential of determining rock formation strength and gold mineralization from rotary percussion drilling data. To achieve this objective, an electronic Logging While Drilling (LWD) system was developed to record real-time drilling parameters, including feed pressure (thrust), percussion pressure, damping pressure, rotation pressure, air flush pressure, and bit travel. This LWD system was installed in an Atlas-Copco T40 top hammer rotary percussion drill rig. During the field trial of the system, a set of 37 vertical blast holes were drilled to a depth of 7.5m in mafic volcanic rock containing thin gold-bearing quartz veins. For 10 of these blast holes, the cutting sample was collected for every 0.5m of bit travel. Based on standard rotary penetration drilling models, the Rate of Penetration (ROP) is inversely proportional to the square of the formation strength. For the drilling data analysis, it was determined that the damping pressure (which is related to the percussion rebound energy) was inversely proportional to the measured ROP. Also, the rotary pressure (related to rotary speed) was proportional to the measured ROP. From the drilling data, logs of formation strength were determined from the measured drilling parameters. Percussion Index (PI) is used in the attempt to calculate the in-situ UCS of the rock.

The result is analyzed, and suggestions are proposed for this empirical method. PCA (Principal Component Analysis) is introduced to build the prediction model of gold grade using the real-time LWD data. The result was obtained after the model training and cross-validation. The gold grade prediction model based on PCA analysis captured the trend of the gold grade and showed potential in the gold grade prediction.

7.3 Mining site geology

This study used the rotary percussive drilling method in the blast hole drilling at the pine cove mining site. Gold mineralization is hosted by mafic volcanic and intrusive volcanic rocks in the Pine Cove area. Outside the mafic volcanic, there is also some argillite as surrounding rock. The estimated average gold grade is 2.07g/t Au at a cutoff of 0.95 g/t (Puritch and Buck, 2010).

The rotary percussive drilling method was used for the blast hole drilling for the open-pit mining in Pine Cove. Cores were drilled from the mining site, and a laboratory test was conducted on the cores to determine the mechanical properties of the rock. Among all the mechanical properties of the rock, e.g.,

Figure 7-1 Pine Cove open pit mining site

Figure 7-2 Field survey showing mafic intrusive and mafic volcanic

Unconfined Strength (UCS), tensile strength, and Young's modulus, UCS has the most vital relationship with the Rate of Penetration (ROP) (Bakar et al., 2018; Kahraman et al., 2003). Also, according to the laboratory test, the average UCS of the gold ore is 66.5MPa, while the UCS of mafic volcanic and argillite ranges from 51MPa to 56MPa. The difference in UCS shows potential in distinguishing gold ore from waste rock using in-situ UCS value. If we can effectively distinguish the ore and waste boundary, the dilution will be reduced, and the recovery will be obtained. Traditionally the gold grade and rock classification are conducted by cutting analysis. However, the cutting analysis is time-consuming and increases production downtime because it requires laboratory experiments. Thus, real-time MWD data analysis to predict in-situ UCS and distinguish between ore and waste rock is beneficial for the mining industry by reducing the time and cost during the operation.

Rock face mapping was conducted and calibrated by field survey, as shown in Figure 32. The rock face mapping result identified the potential ore-waste boundary, and the blast zone was determined. In this research, MWD data was collected in 37 blast holes in two blast zones; cutting samples were collected and analyzed in the laboratory every 0.5m of bit travel for ten holes. The average depth of the holes is 7.5m.

7.4 LWD system configuration

Table 7-1. Atlas Copco T40 parameters

Parameter	Characteristics
Drilling method	Top hammer
Hole diameter	76 mm - 127 mm
Rock drill/DTH hammer size	COP 2560+
Maximum hole depth	28 m
Engine power	168 kW

A new Logging While Drilling (LWD) system was developed by Kyzym (2018) and installed on Atlas

Figure 7-3 Data Acquisition System (DAQ) system (left) and the remote control for the driller (right)

Copco T40 blast hole drilling rig. The Data Acquisition System (DAQ) system and the remote control for the driller are shown in Figure 7-3. FlexiROC T40 is a flexible and versatile top hammer drill rig. Some of the T40 parameters are shown in Table 7-1

Major LWD components include:

1) Hydraulic and pneumatic pressure transducers that measure the various drilling parameters.
2) Cable position sensor (string pot) that measures the travel of the hydraulic line carousel.
3) Data Acquisition System (DAQ) to record the data from the sensors.
4) Electrical cables and pneumatic and hydraulic fittings connect the sensors to the DAQ system.

The LWD was designed to be compatible with the T40 drill rig. The hydraulic and pneumatic pressure data was read from the rigged system using pressure transducers. The hole depth was measured using an independent system by mounting a string potentiometer on the plate on top of the mast. The recorded parameters were:

1) The time during the whole drilling operation.
2) Hole depth.

3) Rotation pressure.

4) Feed pressure.

5) Percussion pressure.

6) Torque pressure.

7) Damping pressure.

8) Flushing air pressure

Based on the time and hole depth measured by LWD, the Rate of Penetration (ROP) was then calculated. Please note that the rotation speed, feed force, percussion force, torque, damping force and flusing air force are measured by pneumatic or hydualic pressure transducer which were attached to the pressure port on the drill rig. The measured pressures unit (Pa) were converted to rpm or Newton based on the drill rig mechanical structure.

7.5 LWD data process

The time, hole depth, rotation pressure, feed pressure, percussion pressure, torque pressure, damping pressure, and flushing air pressure were collected in real-time during the top hammer drilling by the LWD system. Then the ROP is calculated using time and hole depth. Thirty-seven holes were drilled, and around 25 thousand data points were acquired. The gold grade for each 0.5m deep interval was obtained for ten holes through laboratory cutting analysis (Kyzym, 2018). Then, based on these data, the rock characterization is attempted.

7.5.1 The relationship between rotary pressure (torque) and ROP

Among all the drilling performance parameters, it was observed that the torque pressure and damping pressure have a relatively good relationship with the ROP. The rotary motor applies rotary pressure to the drilling rod to rotate the drill bit at the bottomhole. Thus, each successive percussion of the bit is impacted at a new place in the bottomhole.

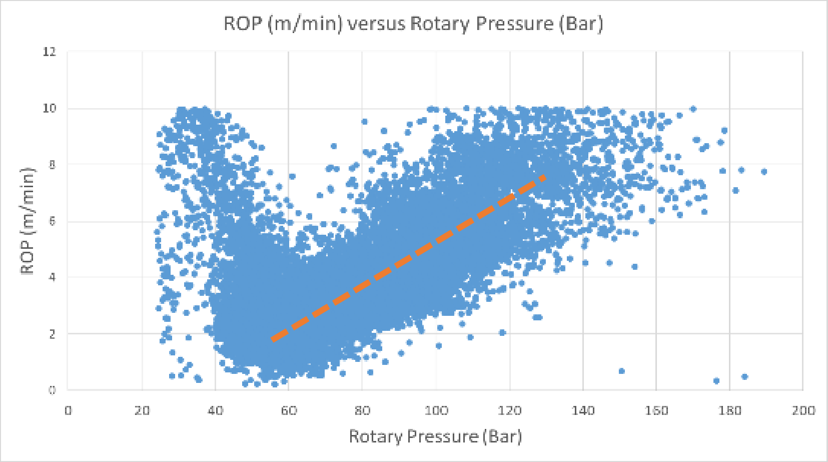

Figure 7-4 Relationship between ROP and Rotary Pressure

The ROP was plotted against rotary pressure. By combining all the available LWD data, the relationship between the ROP and rotary pressure was presented in Figure 7-4. The recorded raw data need to be filtered, as they may include incorrect or faulty data. The ROP data selected range was 1m/min to 10m/min, and the rotary pressure selected range was 0 bar to 200 bar. The data out of this range was considered incorrect. Considering that the LWD data was collected in real-time and contained too many data points, the data was processed by calculating the average ROP and rotary pressure every 5 seconds in time intervals (50-time steps). Then the number of data points is reduced, eliminating the possible error due to the real-time data collection. The relationship between the average ROP and average rotary pressure is presented in Figure 7-5.

It is noticed that these two Figures show the same trend: ROP decreases with the increase of rotary pressure when the rotary pressure is less than 60 Bar. After that, the ROP increases with rotary pressure. Firstly, when the ROP decreases with the increase of rotary pressure. Referring to the previous study (Schunnesson, 1996), these data points are considered error data. After going back to check these data, it is found that most of them are collected when the drilling rod is tripped or when the drilling operation starts or stops. When the ROP increases with rotary pressure, the rock is identified as medium-hard solid rock. Thus, after eliminating the error data, the relationship between ROP and rotary pressure is considered linear

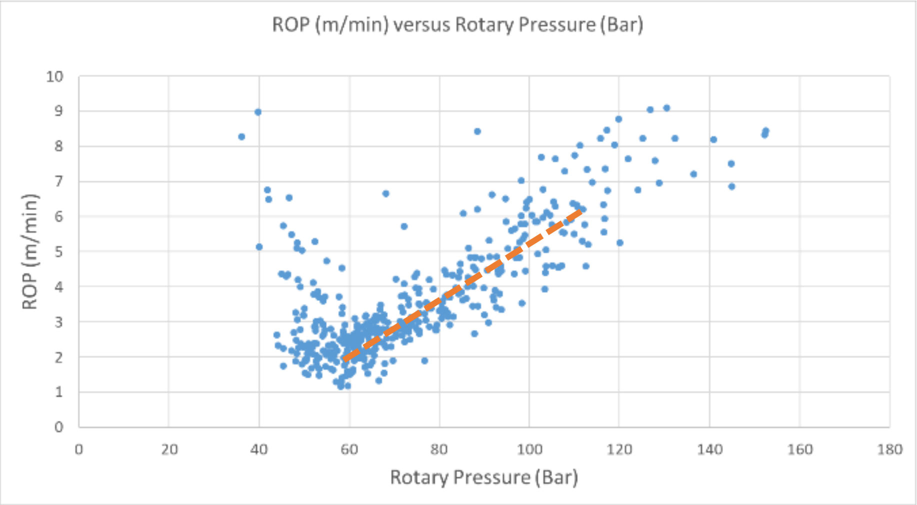

Figure 7-5 Relationship between ROP and Rotary Pressure (Average value)

fitted with a linear trend line, as shown in Figure 7-4 and Figure 7-5. The equations for the fitted linear trend lines for raw data and processed average data are given in the equations below.

$$ROP = 0.0687 * (Rotary\ Pressure) - 1.6347,\ R^2 = 0.6887 \tag{7-1}$$

$$ROP = 0.0669 * (Rotary\ Pressure) - 1.4596,\ R^2 = 0.7496 \tag{7-2}$$

By comparing these two equations, it is concluded that the relevant results of the raw data and the processed data have the same trend, and the equations are similar. However, the processed average data presents a better fitting accuracy than the raw data in terms of the R square. The rotary pressure is strongly related to the ROP of top hammer rotary percussion drilling.

7.5.2 The relationship between damping pressure and ROP

Damping pressure is the pressure of the damping system absorbing the rebound energy from the piston. It directly reflects the strength of the rock to some extent. Previously, the relationship between rotation pressure (torque) and the ROP has been widely discussed. However, the damping pressure has not been studied as much as other drilling performance parameters.

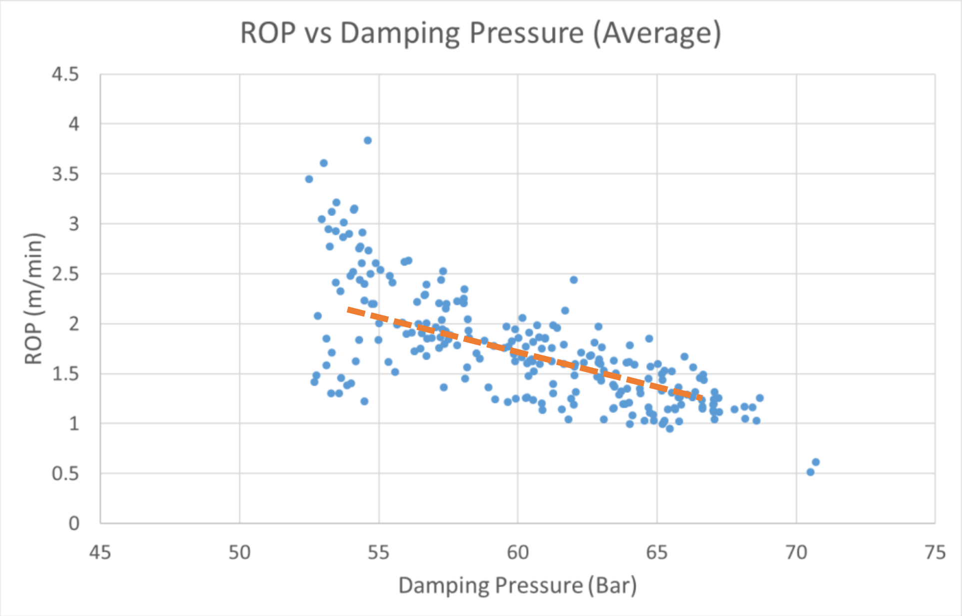

Figure 7-6 Relationship between ROP and Damping Pressure (Average value)

Combining all the available LWD data, the relationship between the ROP and damping pressure is presented in Figure 7-7. The recorded raw data need to be filtered, as they may include incorrect or faulty data. The ROP data selected range was 1m/min to 10m/min, and the rotary pressure selected range was 0 bar to 80 bar. The data out of this range was considered incorrect. The data was also processed by calculating the average ROP and rotary pressure every 5 second time interval (50-time steps). Then the number of data points is reduced, and the possible error data due to the real-time data collection is eliminated. The relationship between the average ROP and average rotary pressure is presented in Figure 7-6.

From the Figures, it is noticed that there is a significant crop of damping pressure at around 52 Bar. Below 52 Bar, there is almost no data point. In the region between 52 Bar and 54 Bar, the ROP goes up to 9 m/min. It is assumed that this phenomenon is induced by the physical limit of the damping system of the drill rig or the limit of the damping pressure transducer. Both Figures show that the ROP decreases with the damping pressure. It concurs with our general understanding of the damping mechanism of the percussive drill rig. When the rock strength increases, more percussion energy is required to penetrate the

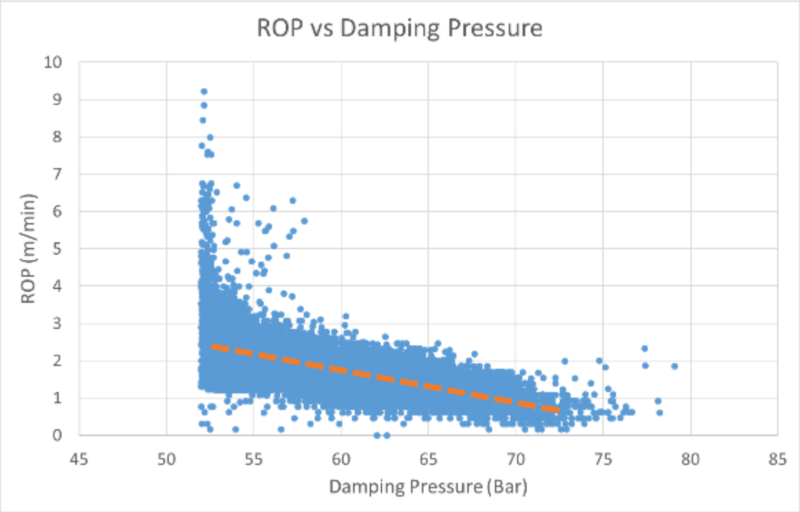

Figure 7-7 Relationship between ROP and Damping Pressure

rock, and more energy is rebounded. Then the two Figures are fitted by linear trend lines. The equations are given below

$$ROP = -0.0928 * (Damping\ Pressure) - 7.338,\ R^2 = 0.4312 \tag{7-3}$$

$$ROP = -0.0904 * (Damping\ Pressure) - 7.184,\ R^2 = 0.5637 \tag{7-4}$$

The equations show that the relationship between ROP and damping pressure has the same trend and close parameters for raw and processed average data. In the processed average data, data points far from the trend line are eliminated because of the average algorithm, and the accuracy is higher because its R square is higher. The damping pressure is proven to be potential in terms of predicting the ROP of top hammer rotary percussion drilling, although further study is needed.

7.5.3 In-situ rock UCS calculation

Calculation of in-situ rock UCS is a time and cost-consuming task. The laboratory experiment is a reliable method, but it requires a long time to move the cuttings to the lab, and for the test, sometimes it would even lead to an increase in downtime. In this study, the parameter Percussion Index (PI) (Chitty et al., 2005; Xiao et al. ,2018) is used as an attempt to calculate the in-situ rock UCS using the real-time LWD data.

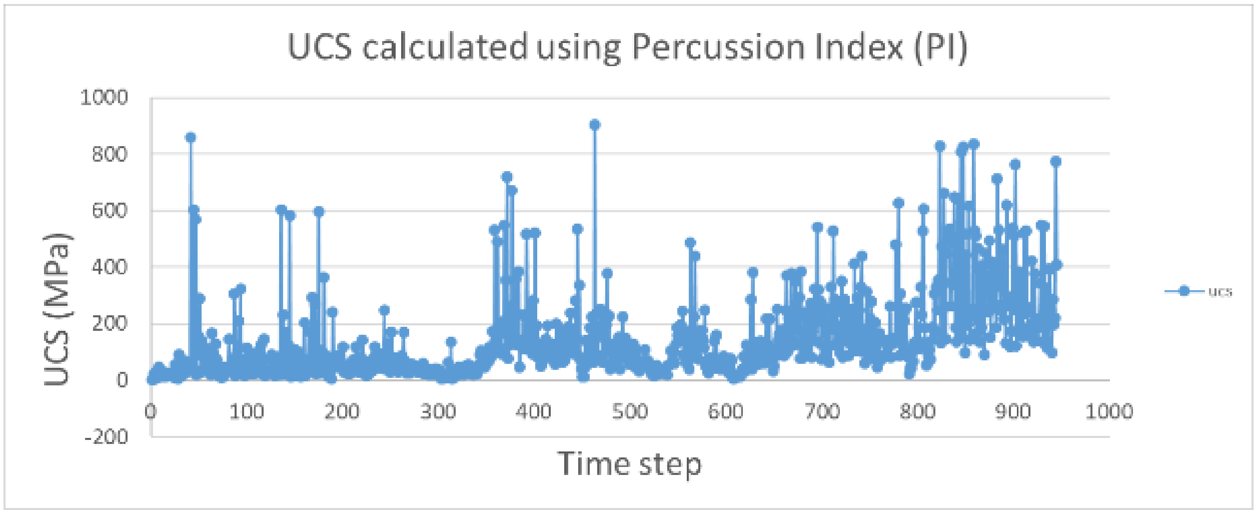

Figure 7-8 Real-time UCS calculated using Percussion Index (PI)

The Percussion Index (PI) is an empirically defined metric that could calculate the in-situ UCS of rock and identify the change in the mechanical rock properties and thus change of rock face. Each hammer blow requires real-time ROP, percussion frequency, and impulse (momentum). The calculation of the Percussion Index and the in-situ UCS is shown below:

$$\lambda_p = \frac{e^{(0.00127 I_b^2 + 0.00708 I_b)} \times \omega}{ROP} \tag{7-5}$$

$$UCS = 0.13 {\lambda_p}^3 \tag{7-6}$$

Where, λ_p is the Percussion Index; $I_b$is the impulse (momentum) in each hammer blow, N*s; ω is the percussion frequency, Hz; ROP is the penetration rate in real-time, mm/s. In the real-time LWD data collection, the percussion pressure is recorded. Based on the percussion pressure, the percussion power for each blow is then obtained.

$$I_b = \sqrt{2W \times m \times \beta} \tag{7-7}$$

Where W is the percussion power per blow, Walt; m is the mass of the piston in the percussion drill assembly; β is the energy transfer coefficient from the hammer to the piston, dimensionless. Then the Percussion Index (PI) was calculated using the real-time LWD data.

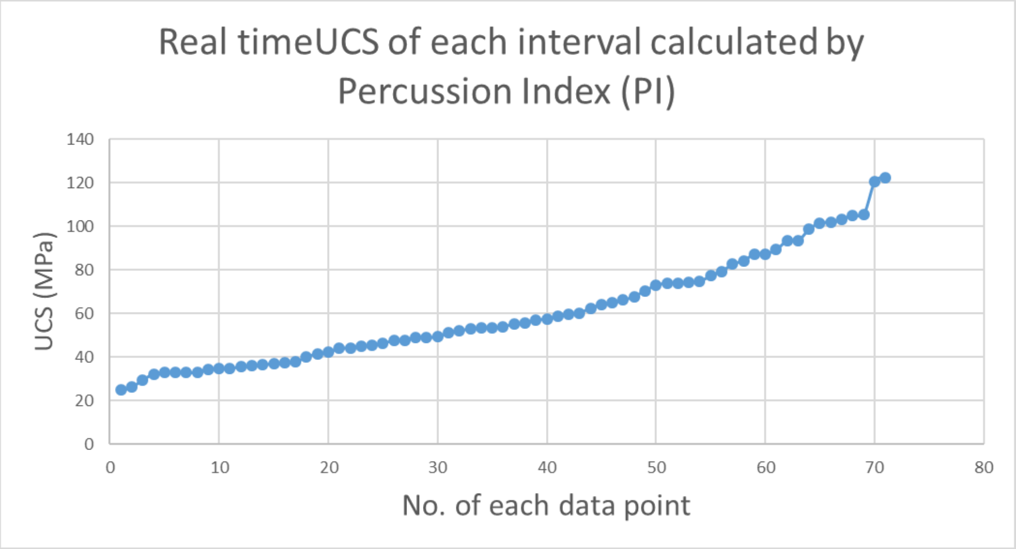

Figure 7-9 Real-time UCS of each interval calculated using Percussion Index (PI)

The real-time UCS calculated from the Percussion Index (PI) of one of the blast holes is shown in Figure 7-8. It is seen that some data points highly deviate from the center. Thus, the UCS is calculated in each 0.5 depth interval. Then, it is compared with the gold grade data of each interval.

It is seen in Figure 7-9 and Figure 7-10. When in-situ UCS is calculated by layer rather than time step, the highly deviated data points are eliminated because of the average algorithm. The new UCS ranges from

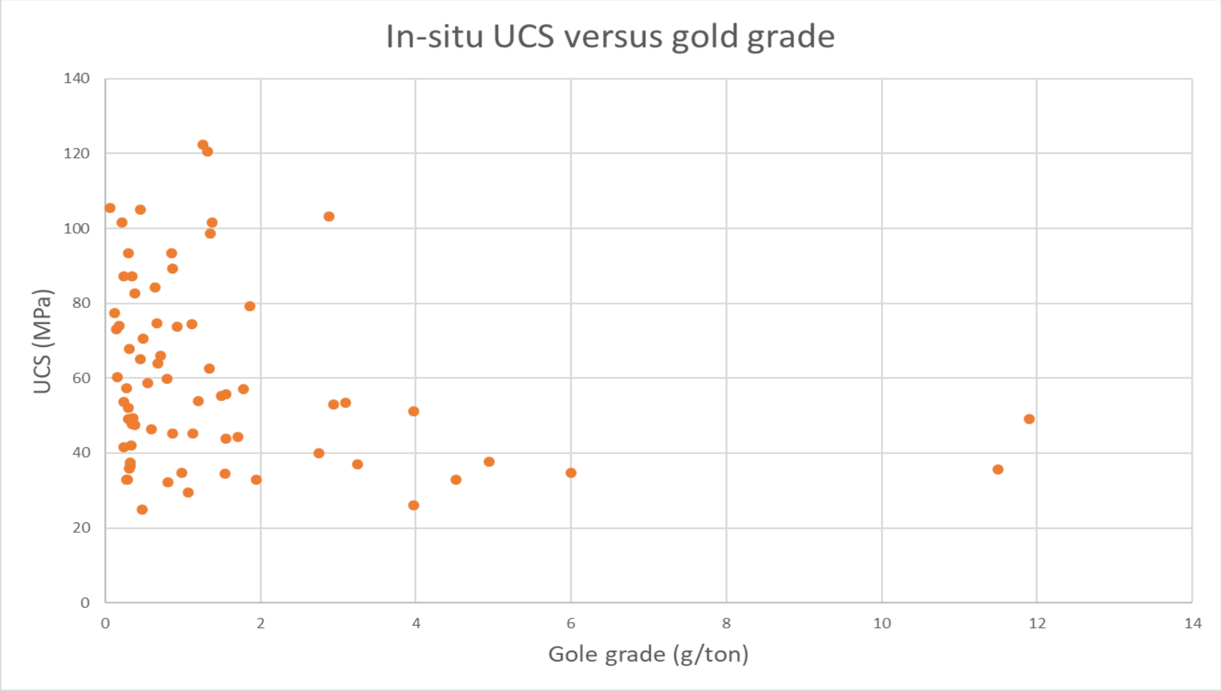

Figure 7-10 In-situ UCS versus gold grade

22 MPa to 124MPa. According to the laboratory core test of the Pine Cove rocks, the UCS of mafic volcanic and argillite ranges from 41MPa to 75MPa. The distribution of the calculated in-situ UCS is dispersed in an extensive range. Also, it is concluded that the gold grade cannot be predicted directly by the calculated in-situ UCS, although the UCS of gold ore and the surrounding rock are different. Further study is needed to calculate in-situ UCS using Percussion Index (PI) because parameters are needed, especially for the study area or the rig.

7.5.4 Attempt to gold grade prediction

Among all the measured LWD parameters, ROP, feed pressure, damping pressure, percussion pressure, and rotation pressure potentially influence factors of gold grade. In order to get to the relationship between the measured parameters and the gold grade, PCA (Principal Component Analysis) is used to identify the most critical influence factor and discard the influence factors with less weight.

According to the table, component 5 accounts for 83% of the variation of gold grade, and component 4 has 10.4 percent weight. More than 93% of the gold grade variation can be kept by keeping these two components. In the meantime, only parameters determine the gold grade, simplifying the calculation. Then using the correlation between component 4,5 and the gold grade, the gold grade is predicted, as shown in

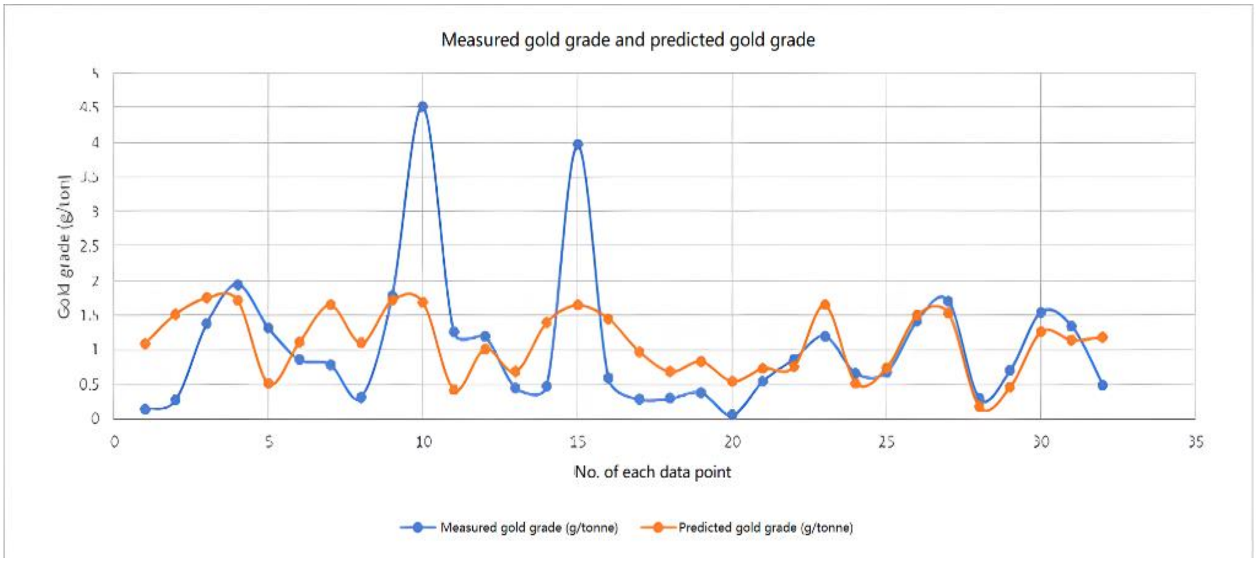

Figure 7-11 Comparison of measured gold grade and predicted gold grade using PCA analysis.

Figure 41. Note that the average value (by depth interval) of the LWD parameters is used, and the number of data points is reduced. In Figure 7-11, only 10% of the data point is used in the prediction because 90% of the data points are used for model training and cross-validation with the shown 10% data points. This is because in this case, the best prediction accuracy was achieved when 90% data was used for model training and 10% data was used in the prediction.

From the comparison result, the predicted gold grade roughly captures the trend of the measured gold grade. However, the prediction model fails to give an immediate answer for some measured gold grades, especially for some extremely high gold grades. Although the prediction is close to some data points, the overall accuracy is not satisfying enough.

Table 7-2. PCA components and weight

Contribution of each parameter in each Principal Component					
	PC1	PC2	PC3	PC4	PC5
ROP	0.011	-0.103	-0.108	-0.369	0.917
Damp	0.820	0.547	0.143	0.080	-0.023
Feed	-0.399	0.696	-0.527	0.2758	-0.024
Percussion	0.408	0.417	-0.8052	0.103	-0.011
Rotation	0.007	0.176	0.202	0.877	0.397
Weight	0.006	0.013	0.043	0.104	0.832

7.5.5 Conclusions and recommendations

Based on standard rotary penetration drilling models, the Rate of Penetration (ROP) is inversely proportional to the square of the formation strength. The drilling data analysis determined that the damping pressure (related to the percussion rebound energy) was inversely proportional to the measured ROP. The rotary pressure (related to rotary speed) was also proportional to the measured ROP. From the drilling data, logs of formation strength were determined from the measured drilling parameters. Percussion Index (PI) is used to calculate the in-situ UCS of the rock. The result is analyzed, and suggestions are proposed for this empirical method. PCA (Principal Component Analysis) is introduced to build the prediction model of gold grade using the real-time LWD data. The result was obtained after the model training and cross-validation. The gold grade prediction model based on PCA analysis captured the trend of the gold grade and showed potential in the gold grade prediction.

Chapter 8: Rock mechanical characterization through indentation test

The research work of this chapter has been submitted to the peer-reviewed journal < journal of rock mechanics and geotechnical engineering>, and now it's under review.

8.1 Co-authorship Statement

Zijian Li: Laboratory Experiment, Data Processing, Numerical Simulation, and Writing Manuscript

Prajit Premraj: Support on Laboratory Experiments and Data Processing

Dr. Stephen Butt: Supervision and Reviewing

8.2 Abstract

Most rock samples acquired in Canadian mining and civil field work are NQ size rock cores (47.6mm diameter). In the traditional Unconfirmed Compressive Strength (UCS) test, the length required is around 100mm for the NQ size core. The discontinuity in the field always limits the core recovery rate. When the natural fractures and joints are highly developed, the sample preparation for the UCS test becomes difficult. In this study, the Indentation Test (IT) on rock cores was evaluated through laboratory experiments and numerical simulation, since it has the potential to estimate the UCS strength but requires less amount of rock sample. The IT lab test results of Granite and Rock Like Material (RLM) were analyzed, and a correlation between the UCS strength and the IT result was developed for the UCS prediction. Based on the IT lab test results, suggestions were presented for the sample preparation method optimization. A series of disk cutter drilling tests were performed on granite. The relationship between the IT test results and the disk cutter was proposed, because IT and disk cutter drilling have the same rock failure mechanism: crushing rather than shearing. Discrete Element Method (DEM) simulation was conducted using PFC software in order to investigate the rock model failure process during the IT test. It was observed from the simulation result that the ball size of the rock model influences the IT test performance, and it is suggested that the ball size should be regarded as a critical micro property for the PFC rock model calibration for IT

or other forms of tests regarding the rock crushing failure.

8.3 Introduction

In drilling engineering, rock indentation and rock shearing (cutting) are the two main types of rock fragmentation (Copur et al., 2003). The rock indentation is the dominant rock penetration mechanism of the roller cone bit, the percussion bit, and the disc cutter, while rock shearing plays a vital part in the drag bit drilling. The difference is that the former indenter's contact force is perpendicular to the rock surface, whereas the latter is parallel to the rock surface (Hood and Roxborough, 1992). Studying the rock deformation and failure mechanism during the rock drilling process is necessary. A series of lab-scale experiments have been carried out to explore the rock-breaking behaviors and provide a reference for the drilling optimization. The indentation and linear cutting tests are the most common lab-scale rock-breaking tests. Drilling with an indenter is widely used in rock excavation. In this study, the research focuses on the rock indentation process.

The indentation experiments have been widely employed on different rock types and indenter shapes to study the rock indentation failure mechanism. Gnirk and Cheatham (1963) experimentally investigated the effects of tooth angle and confining pressure on the force required for the indentation of dry rock samples under different confining pressure. Mishnaevsky (1995) reviewed the energy consumption during the rock indentation process and discussed the influence of the loading rate, the shape of the indenter, and cutting conditions on the rock penetration. Szwedzicki performed the standardized indentation test procedures on different rock types (Szwedzicki, 1998). Chen and Labuz (2006) conducted indentation tests using a wedge-shaped indenter to evaluate the development of the rock failure zone. It was proposed that the rock properties, the indenter geometry, and the rock confinement stress are the principal factors controlling the rock failure process. Kahraman et al. (2012) conducted an indentation test on 46 rock types. They developed an empirical correlation between the indentation hardness index (IHI) and the Uniaxial Compressive Strength (UCS), and Brazilian Tensile Strength (BTS) (Kahraman et al., 2012). Zou et al. (2020) investigated the effect of the loading rate and the in-situ rock stress state on the failure patterns of indentation. Although the sample preparation and the indentation operation vary among researchers, a general can be summarized as a laterally confined rock sample crushed by an indenter with a controlled loading rate.

During the indentation test, the indenter's displacement and force are recorded. The size or depth of the resulting indentation is used to calculate the indentation hardness index (IHI), which is usually calculated as the slope of the indentation load/displacement curve (Szwedzicki, 1998). The soft material gives the larger and deeper the depression and the lower the hardness index number. The IHI has been used to predict the rock UCS (Szwedzicki, 1998; Copur et al., 2003; Mateus et al., 2007; Yagiz, 2009; Kahraman et al., 2012; Haftani et al., 2013). because of its direct relationship to the rock's strength. The drillability of the rock is generally quantitatively described as the rate of penetration (ROP), and the correlation for the ROP prediction is also reported (Kahraman and Gunaydin, 2008; Kahraman et al., 2012).

Indentation tests may use less complex testing equipment and have less strict standards for sample preparation. Therefore, compared to the common UCS test, such tests are significantly more straightforward, quicker, and cost-effective (Szwedzicki, 1998). One of the best methods for determining a rock's cuttability is to conduct a full-scale rock cutting test, which decreases the scaling impact by cutting a realistic rock sample. Its drawback is that technique necessitates obtaining big slabs of rock samples (about 1 x 1 x 0.6 m), which are frequently challenging and expensive (Copur et al., 2003; Kahraman et al., 2012). Therefore, while having weaker predictive capacities than full-scale rock cutting tests, core sample based cuttability studies are frequently recommended. The predictive power of core-based cuttability tests could be increased by creating new index tests or test interpretation techniques.

Previous simulations of rock indentation are mainly based on two-dimensional simulations through FLAC2D, PFC2D, and RFPA2D (Ma et al., 2011; Potyondy, 2017; Zhang and Zhang, 2019; Liu et al., 2017; Zhu et al., 2017). Although the two-dimensional model can contain more particles with a much smaller diameter at a higher computing speed, it adopts simplified boundary conditions that do not conform to the actual three-dimensional situation. Because of the discontinuous failure patterns in rock fragmentation, FEM is limited (Zhai et al. 2019). The PFC has recently become popular in geotechnical simulation tests (Xuefeng et al., 2018; Yang et al., 2014). It has also been widely used to simulate the process of rock fragmentation. For example, Yang et al. (2019) used PFC to simulate crack propagation and the Brazilian failure of shale rock. Yang and Qiao (2018) studied the jointed granite material's shear behavior and failure mechanism using PFC. Few numerical methods could depict the entire crack propagation process simulating the indentation test. In many places, the mechanism of the influence of different breaking parameters on rock fragmentation remains unknown, particularly the failure mode of rock and the formation of a crushed zone under the cutting tool.

8.4 Background

The rock fracture model using a single button-bit is summarized as shown in Figure 8-1, based on experimental observations (Tan et al., 1998 and Liu, 2004). There is a crater, a disintegrated and partly re-compacted zone, a crushed but mostly confined zone, and a cracked zone beneath the button bit. Outside the cracked zone, long cracks are classified into three types based on their relationship to the button-bit: median cracks, radial cracks, and side cracks. The numerical modeling explains the fracture system's forming mechanics. The crater forms as a result of tool penetration and rock removal. The re-compacted zone is caused by the recompaction of the crushed rock and is located immediately beneath the button bit. The zone with a high density of micro cracks, which makes the distinction between the crushed zone and the crack zone less clear, is actually the crushed zone. In certain instances, the radial and median cracks are

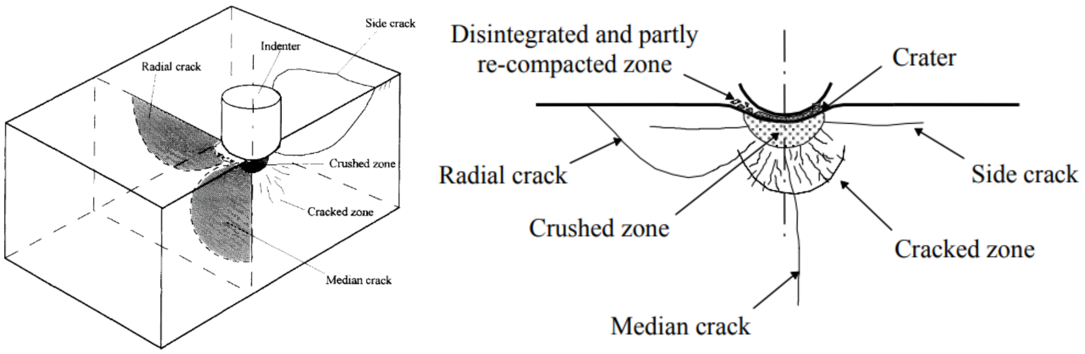

Figure 8-1 General picture of fracture systems in rock under a single button-bit (Tan et al., 1998 and Liu, 2004)

difficult to see. Conical Hertzian cracks, which are primarily responsible for rock fragmentation in bit rock fragmentation, are split into side cracks, which begin in the area of the crushed zone and spread approximately parallel to the free surface.

The three primary controlling factors of the rock failure during the indentation test were: 1. The mechanical properties of the rock; 2. The geometry and hardness of the indenter; 3. The lateral confinement of the rock sample (Chen and Labuz, 2006).

There are two forms of rock strength prediction correlations using the indentation test result.

The first form is the exponential form. Kahraman et al. (2012) presented a linear correlation for the rock strength prediction for igneous, metamorphic, and sedimentary rocks:

$$UCS = 0.07 \times IHI + 28.28 \quad R^2 = 0.76 \tag{8-1}$$

Mateus et al. (2007) introduced the definition of Indentation Modulus (IM). IM is the ratio of change in load to the change center in the proportionality zone of load against the penetration curve of the indentation test, which is similar to the IHI. Based on the indentation test on sandstone, the UCS prediction correlation was developed:

$$UCS = 17.38 \times IM \quad R^2 = 0.82 \tag{8-2}$$

Haftani et al. (2013) presented a linear equation to estimate the UCS of limestone using IM:

$$UCS = 3.32 \times e^{0.0019 \times IM} \quad R^2 = 0.97 \tag{8-3}$$

Besides the exponential correlation, Szwedzicki (1998) proposed an exponential equation for the prediction of UCS from IHI for ultramafic and basaltic rocks:

$$UCS = 3.1 \times IHI^{1.09} \tag{8-4}$$

Where, UCS is the unconfined compressive strength (MPa), and IHI is the indentation hardness index (kN/mm). In this equation, there is a coefficient, and an index number comes with the IHI.

Based on the indentation test on limestone, Haftani et al. (2013) also proposed an exponential relationship between the UCS and IM:

$$UCS = 0.2 \times IM - 226.21 \quad R^2 = 0.91 \tag{8-5}$$

In the previous study, the general form of the rock strength prediction correlation using the indentation test result is as follows:

$$UCS = a \times IHI^{b} + c \tag{8-6}$$

Where, a is the proportional parameter, b is the exponential parameter, and c is the intercept. UCS is the unconfined compressive strength (MPa), and IHI is the indentation hardness index (kN/mm).

For simplification, the exponential parameter can be regarded as 1, and only the proportional parameter a and the intercept c are kept. Then the UCS prediction correlation can be simplified as follows:

$$UCS = a \times IHI + c \tag{8-7}$$

8.5 Sample preparation

This study used two rock types for the sample preparation: granite and RLM. The granite blocks were collected from the quarries. RLM is a material fabricated following a specific recipe. RLM has proven to be consistent in terms of strength and reproduces repeatable in the UCS test (Zhang, 2017). Granite was categorized as a high-strength rock, while the RLM was classified as a medium-strength rock. As a artificial rock material, the RLM reduces the material cost, ensures the repeatability of the experiment result, and enables to control of the rock properties (porosity, grain size, etc.). During the fabrication of the RLM, a moderate water reducer content was used to control the water content and enhance the cement content. The granite and concrete block samples were inspected for defects so that the test sample had no fractures or other defects before the test.

2-inch diameter core samples were drilled from the granite and RLM blocks through diamond core drilling. The core samples were placed in 4-inch diameter cylindrical molds and then cast with concrete paste with a UCS strength between 30 and 35 MPa. The samples were stored in a controlled moisture and temperature environment for curing. After the curing, the samples were cut into 4-inch-long cylinders, indicating that the height-to-diameter ratio was 1:1. The samples' surfaces were grinded to ensure the surface was smooth. Then the grinded core was restrained by a metal strap around the circumference to provide confining pressure. The two bolts on the metal strap were fastened with a torque wrench, and the torque was controlled at 8.84 N/mm

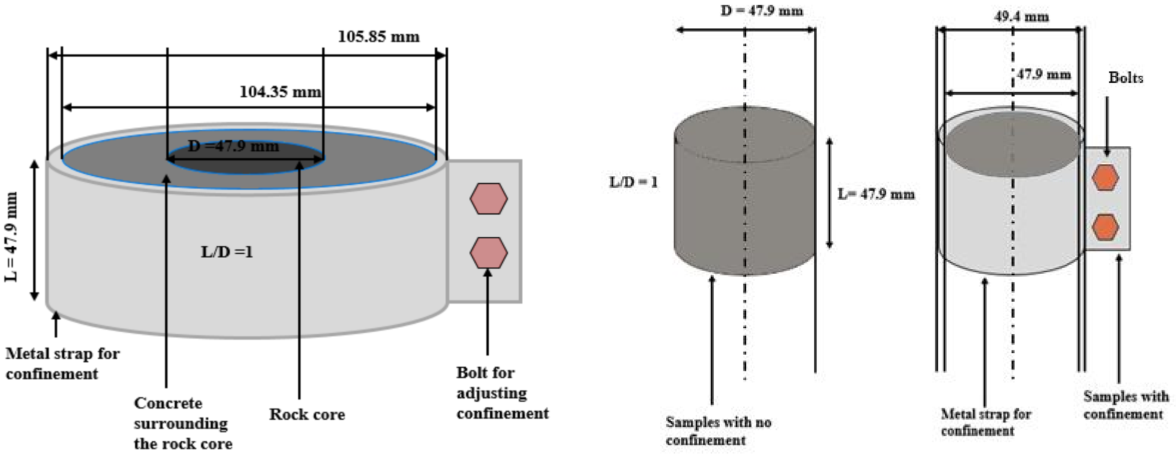

Figure 8-2 Dimensions of the sample for indentation (casted in concrete with metal strip)

In summary, there are four sorts of samples prepared. Both granite and RLM were cast in concrete and confined in the metal strip. Besides, granite was also confined in the metal strip without concrete casting or any confinement. The summary of the sample preparation is given in the table below.

Table 8-1 Sample preparation of the Granite and RLM

Sample Preparation Type	**Rock Type**	**Core Length**	**Core Diameter**	**Concrete Confinement**	**Metal Strap Confinement**	**Number of Samples**
1	Granite	2 inch	2 inch	Yes	Yes	4
2	Granite	2 inch	2 inch	No	Yes	4
3	Granite	2 inch	2 inch	No	No	4
4	RLM	2 inch	2 inch	Yes	Yes	6

The mechanical properties of the Granite and RLM were obtained from the laboratory tests before the IT. The laboratory test result was used as a reference for the IT analysis.

Table 8-2 Laboratory test result of the Granite and RLM

Rock	Density	UCS	PLI	E	P-wave	S-wave	μ
	(g/cm^3)	(MPa)	(MPa)	(GPa)	(m/s)	(m/s)	N/A
Granite	2.93	167.78	14.17	13.17	5480.91	3433.19	0.18
RLM	2.3	78.98	5.79	9.68	4703.85	2840.99	0.21

8.6 Laboratory experiment setup

Figure 8-4 Instron 5585 series dual column floor servo-control frame

The test is conducted on a servo-controlled loading frame. The maximum capacity for compression load is 250 KN. The instrument works on the principle of closed-loop servo control. The metallic indenters used in indentation are mounted on the top platen. The compression loading rate is chosen ahead of time, and the experiment runs for 3 minutes.

The indenter has an apex angle of 60°, tip diameter of 5mm, and strength above Rockwell 58 HRC.

Figure 8-5 Indentation indenter. (Premraj, et al., 2022)

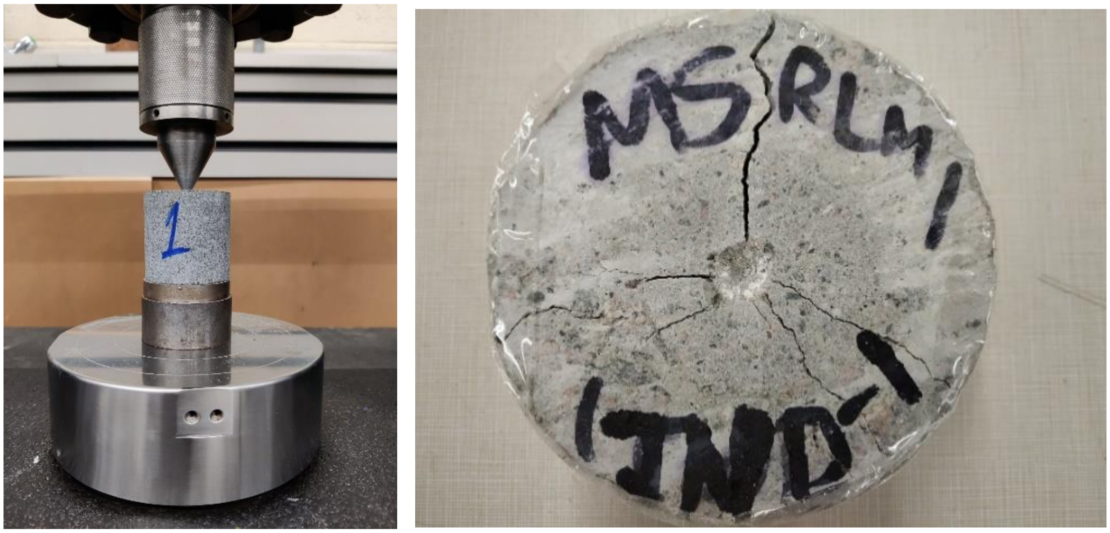

Figure 8-6 Left: the indentation test on the unstrapped rock sample. Right: Top view of crater and fracture formed on an indentation sample. The sample is tested with metal strip during the indentation test. (Premraj, et al., 2022)

The NQ-size core is cast in a 4-inch diameter mold with concrete with a UCS of 30 to 35 MPa. Then the casted sample is cut into a 4-inch-long test sample. Half of the samples are confined with a metal strap, which is tightened to 8.84 Newton meters. The rest are not confined with a metal strip.

To ensure that the results of the IT test could be replicated, the following procedures were followed.

1. Sample preparation was completed and each sample now has a flat end.
2. The load frame was calibrated and adjusted to the desired load rate before being set up.
3. The indenter is secured in place by threads that connect it to the top moving platen of the load frame, and rubber strap wrenches are used to keep the connection tight. (This eliminates the possibility of the load curve being stressed in any way by the loose threads of the indenters).
4. A force of 12 newtons is applied to the indenter as it is pressed into the specimen. (This is done to ensure that the rock sample is properly engaged; starting all tests at the same value ensures repeatability).
5. The evaluation can begin at the predetermined loading rate and will take a total of three minutes.

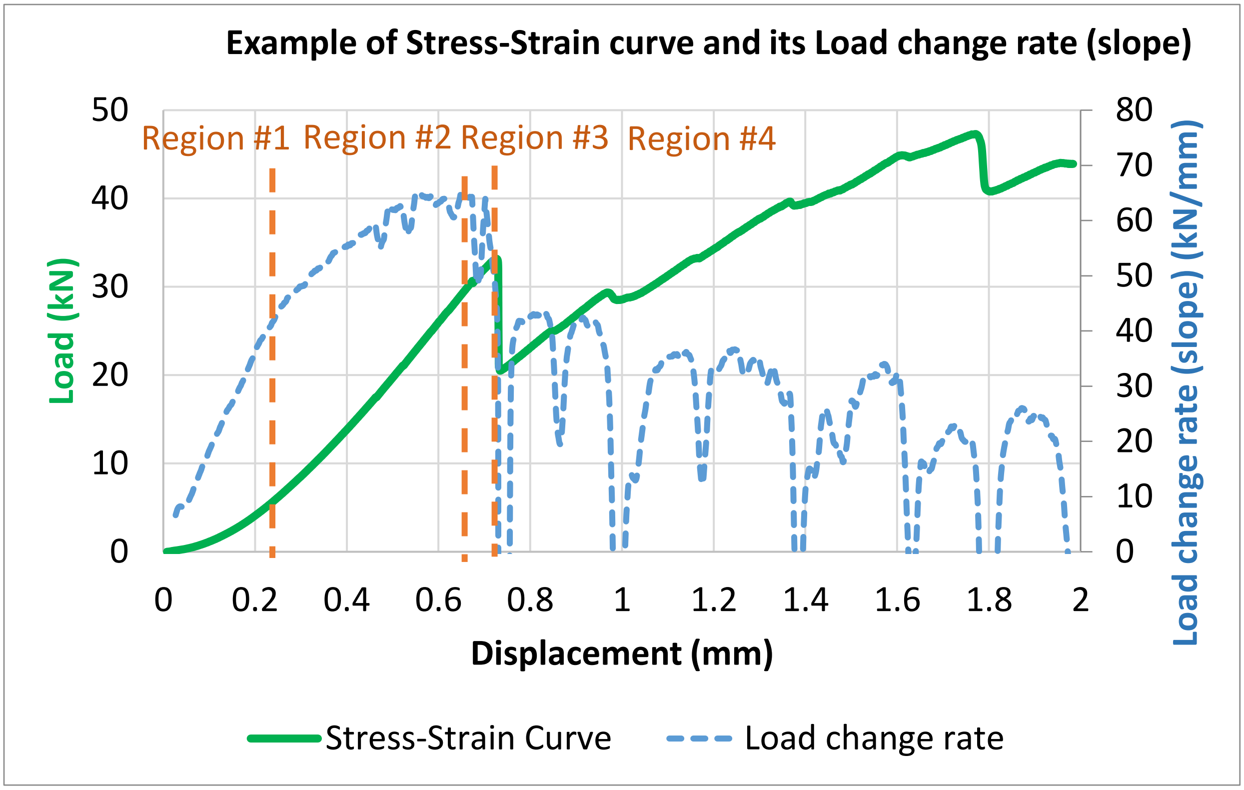

Figure 8-8 Example of Load-Displacement curve and its Load change rate (Granite sample with casting and strip)

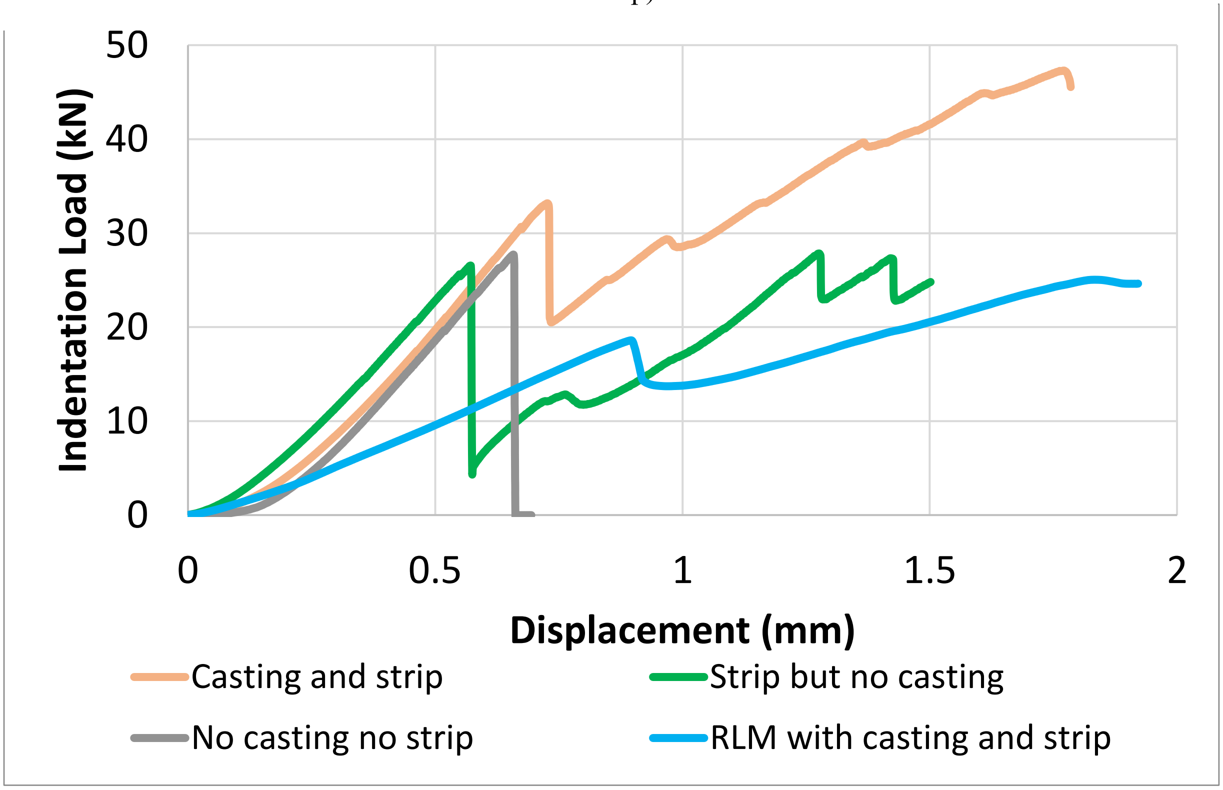

Figure 8-7 IT comparison of 4 differently prepared samples

The loading rate affects the indentation test, and the outcomes may also change if the loading rate

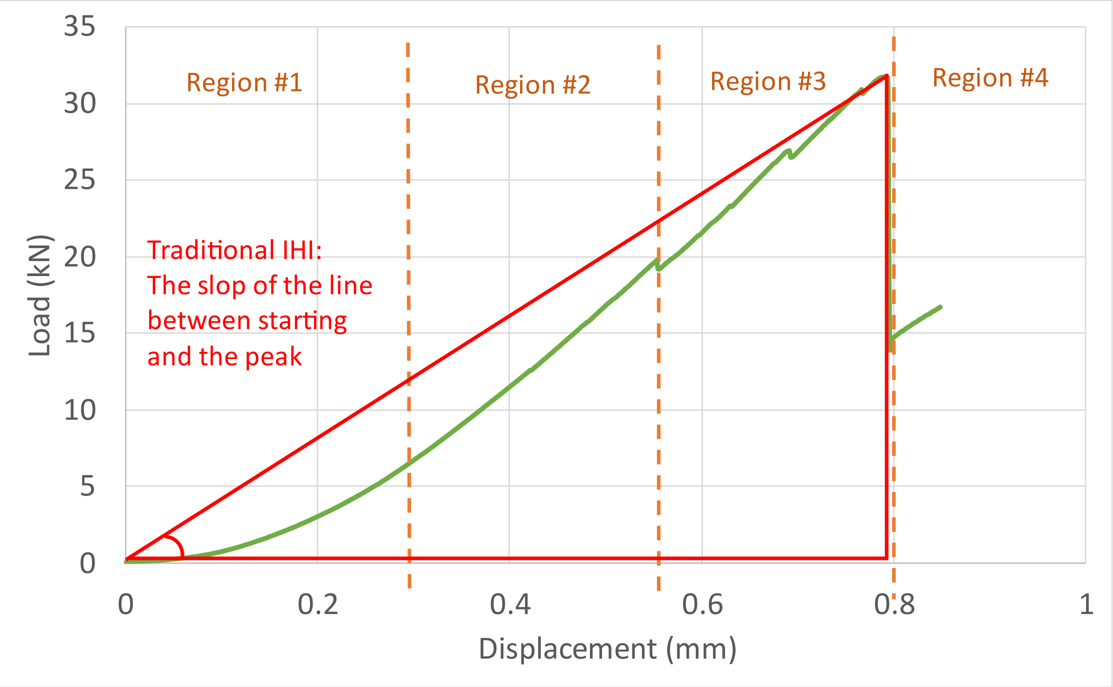

Figure 8-9 Indentation Hardness Index from the IT Stress-Strain Curve of the of Granite Sample with Casting and Strap

changes. Load-controlled and displacement-controlled loading are the two types (Kalyan, 2015). A specified load is applied to a sample once every second in load-controlled loading. The load decreases when a rock fails or fractures, and this system will ramp up in such circumstances. The main drawback of this loading style is this. In the past, most research has employed displacement-controlled loading. The indenter is designed to move a unit distance every second with this type of loading. This works with rocks of all different strengths. Various researchers have frequently used the loading rate value of 0.001mm/sec. The changes in indentation results using loading rates between 0.0025mm/sec to 0.01mm/sec are insignificant (Zhang et al., 2018).

8.7 IT laboratory experiment

8.7.1 The analysis of the stress-strain curve in the rock indentation test

Granite and RLM samples were tested in the laboratory indentation test, and the stress-strain curve was obtained. In Figure 8-9, the calculation of the IHI is shown on the indentation test result. In this chart, the granite sample was prepared with the concrete casting and the metal strip.

According to the test result, it is observed that the stress-strain curve can be divided into four regions. In the first region, a nonlinear increasing slope is observed due to the poor contact and the under-compaction between the indenter and the sample in the early stage. In the next stage, the increase rate of the slope decreases, and the slope tends to be constant. A minor failure is experienced in the third region, while several minor failures may follow until a major failure occurs. Each minor failure is accompanied by a small fracture, which does not penetrate the sample. Although the slop is stable between minor failures, the slop decreases from that in the second region because the slop now does not represent the compliance response of the intact rock sample. Region #3 can be considered a subregion of region #2. If no minor failure occurs, region #3 does not exist. In the last region, a significant failure occurs, which induces the split of the whole rock sample and the declination of the slop as the post-peak response.

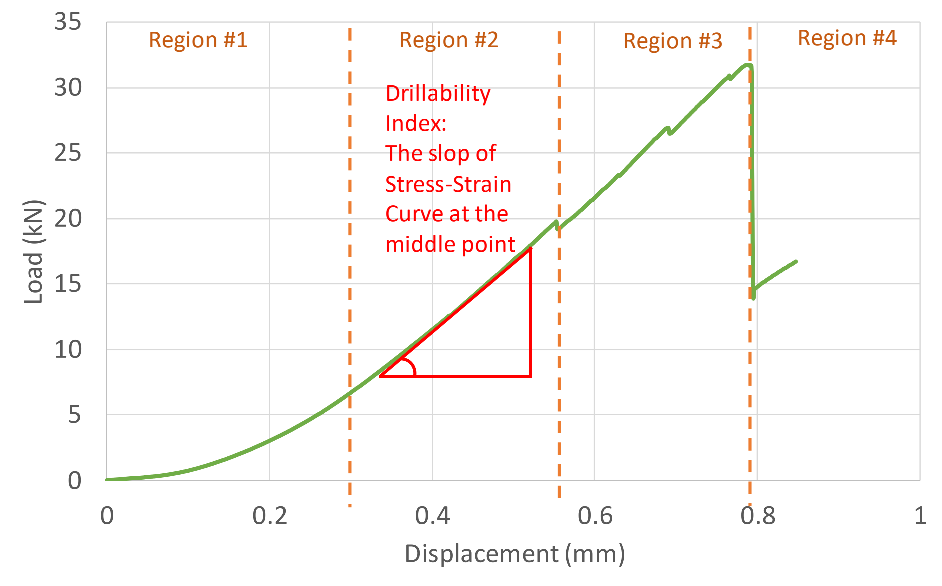

Figure 8-10 Drillability Index from the IT Stress-Strain Curve of the of Granite Sample with Casting and Strap

Figure 8-8 shows an example of a stress-strain curve and a granite sample's load change rate (slope) with casting and strip. The y-axis of the slope was tuned so that only the positive slope was shown in the figure. It is because the magnitude of the peaks of the negative value is significantly higher than the positive ones, which occurred during major rock failures. In region #1, the slope builds up fast from zero. The slope

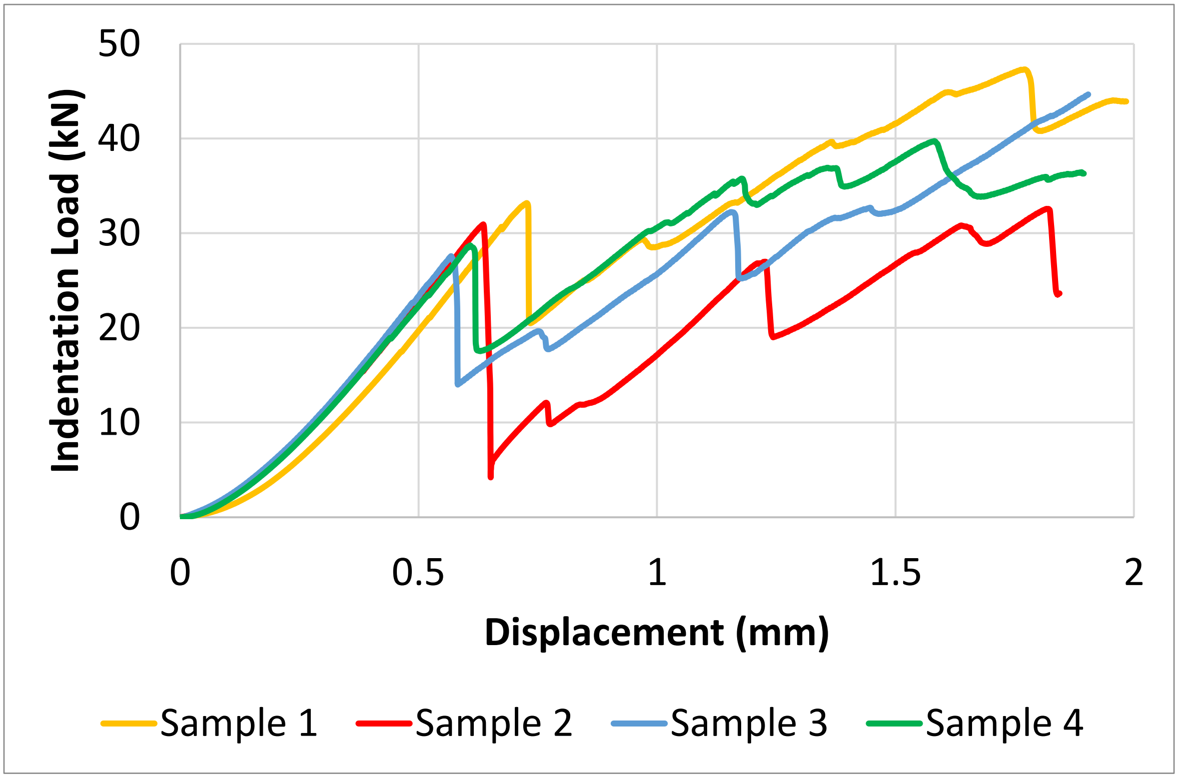

Figure 8-12 IT result of Granite samples with casting and strip

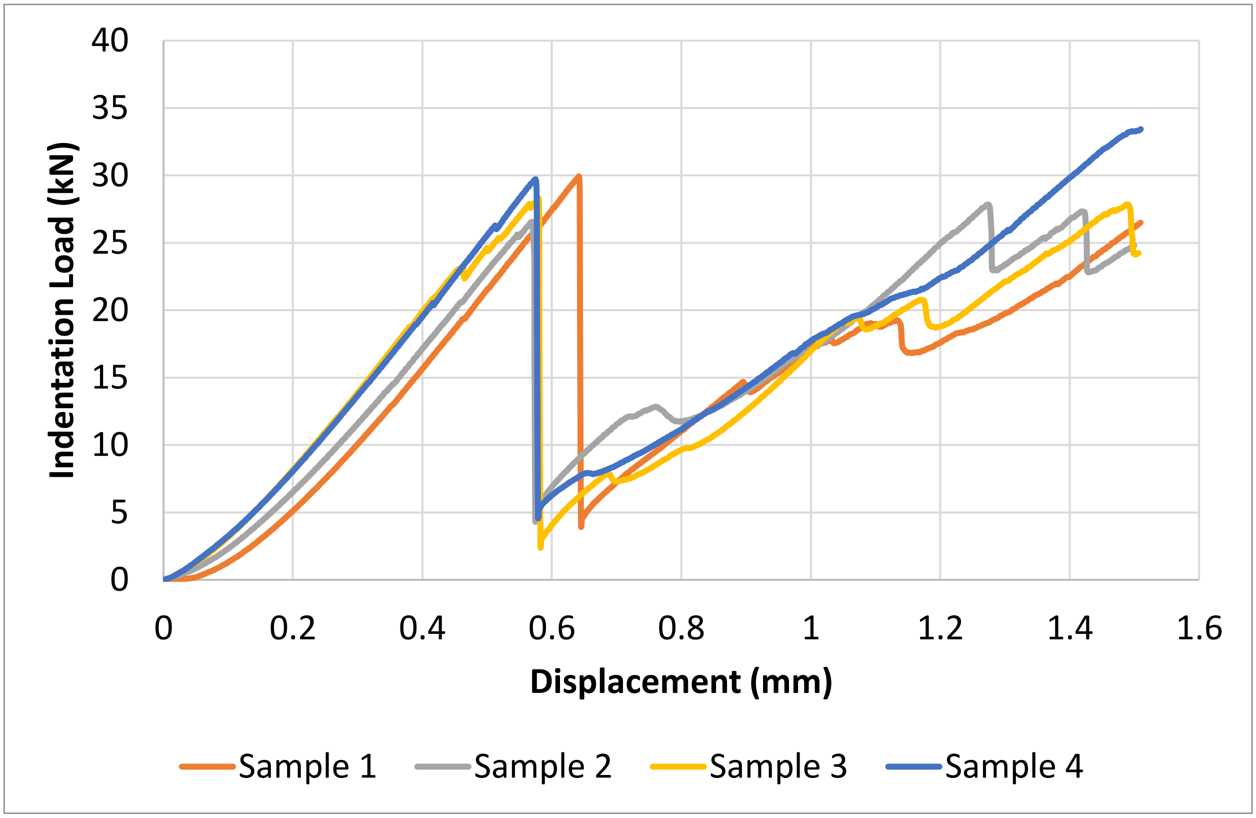

Figure 8-11 IT result of Granite samples with no casting but with strip

in this figure does not start from zero because the data was processed using a smooth average algorithm, and some data points near the zero displacement point cannot be shown here. In region #2, the slope increase rate decreases and tends to be constant. Fluctuations were observed, which indicated the minor rock failures which were difficult to identify from the stress-strain curve. Region #3 started with a minor rock failure presented in the stress-strain curve. The slope exhibited a sharp decrease at the minor rock failure but remained positive. Region #4 lies between the first major rock failure and the end of the curve. The average slope was lower than the maximum slope in region #2 and region #3 and decreased in the post-failure zone.

Table 8-3 IHI and DI result of Sample type 1: Granite with concrete casting and strip

IHI and DI result of Sample type 1: Granite with concrete casting and strip			
Sample No.	**IHI**	**DI**	**UCS Lab result (MPa)**
	kN/mm	**kN/mm**	
1	46.91	56.64	167.78
2	49.07	55.12	
3	49.30	58.22	
4	46.50	55.86	
Average	47.95	56.46	
Standard Deviation	1.25	1.15	
Coefficient of Variance	0.0261	0.0204	

Table 8-4 IHI and DI result of Sample type 2: Granite with strip but no concrete casting

IHI and DI result of Sample type 2: Granite with strip but no concrete casting			
Sample No.	**IHI**	**DI**	**UCS Lab result (MPa)**
	kN/mm	**kN/mm**	
1	46.77	56.2	167.78
2	46.60	55.6	
3	49.00	58.7	
4	51.86	58.5	
Average	48.56	57.25	
Standard Deviation	2.13	1.37	
Coefficient of Variance	0.0438	0.0239	

Table 8-5 IHI and DI result of Sample type 3: Granite no strip, no concrete casting

IHI and DI result of Sample type 3: Granite no strip, no concrete casting			
Sample No.	**IHI**	**DI**	**UCS Lab result (MPa)**
	kN/mm	**kN/mm**	
1	42.75	52.68	167.78
2	37.88	49.49	
3	39.22	51.44	
4	44.82	57.74	
Average	41.17	52.84	
Standard Deviation	2.76	3.05	
Coefficient of Variance	0.0670	0.0578	

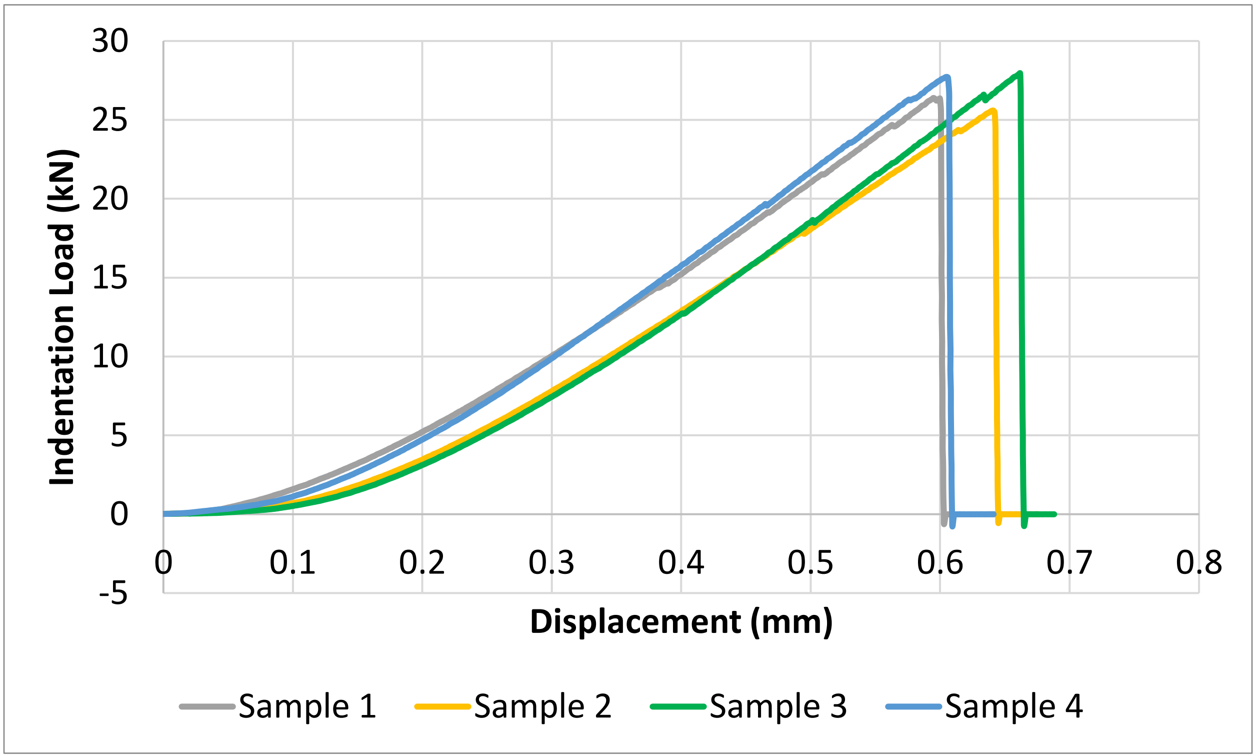

Figure 8-13 IT result of Granite samples with no casting no strip

Table 8-6 IHI and DI result of Sample type 4: RLM with concrete casting and strip

IHI and DI result of Sample type 4: RLM with concrete casting and strip			
	IHI	DI	UCS Lab result (MPa)
Sample No.	kN/mm	kN/mm	
1	20.98	23.09	78.98
2	20.30	22.08	
3	19.31	22.35	
4	21.44	23.78	
5	19.41	21.38	
6	19.62	21.57	
Average	19.61	22.49	
Standard Deviation	0.81	0.84	
Coefficient of Variance	0.0413	0.0372	

8.7.2 The prediction of UCS using the IHI and DI

The calculation of the IHI was shown in Figure 8-9. The average slope of the stress-strain curve from the zero point to the peak load point was used to represent the IHI. At the beginning of the stress-strain curve, the stress gradually builds up from zero partially because of the poor contact between the indenter and the rock sample and the fact that the sample is not compacted enough. It was noticed, however, the length of region #1 varies with different samples, although the rock core came from the same batch of the rock block and was prepared in the same way. On the other hand, several minor failures could occur in region #3, influencing the calculation of the IHI. These two factors contribute to the uncertainty when selecting the starting and peak points in the stress-strain curves.

Another parameter, the Drillability Index (DI), was analyzed in this study in addition to the traditional IHI. The example and the UCS prediction result are shown in Figure 8-10. The DI is considered the slope of the point with half of the peak load on the stress-strain curve (Kahraman et al., 2000). In this way, the uncertainty brought, for example, the minor failure and region #1, are excluded from the calculation. Compared to the IHI, the slope of region #2 (or region #2 and Region #3 together) is less influenced by the minor failure and the variation of the length of region #1, which produces a more stable result. By comparing the IT result of the samples prepared in the same way, it is observed that the IHI and DI of different do not exhibit significant variance, which indicates that the IHI and DI results are relatively stable.

The IT result of different samples was depicted, while the IHI and DI of each sample were calculated. In Figure 11, the examples of four differently prepared samples' IT test results are shown. It is noticed that the RLM stress-strain curve presents a smaller slope, and a smaller peak load but a higher displacement at the peak load. The main reason is that the RLM has a lower UCS strength and lower Young's modulus.

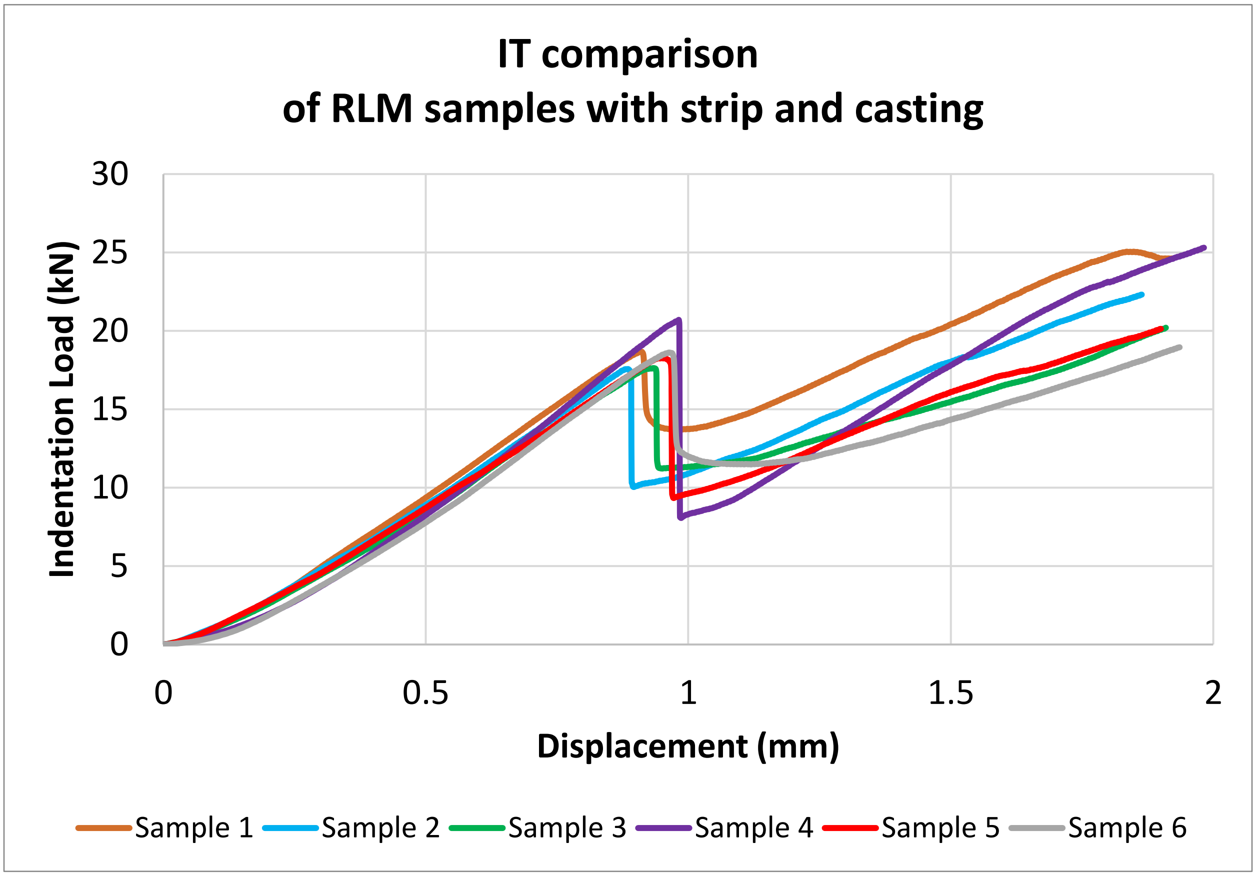

Figure 8-14 result of RLM samples with casting and strip

The IT results of Granite samples with casting and strip were shown in Figure 8-12 and Table 8-3; the IT results of Granite samples with no casting but with strip were shown in Figure 8-11 and Table 8-4; the IT results of Granite samples with no casting no strip were shown in Figure 8-13 and

Table 8-5; the IT results of RLM samples casting and strip were shown in Figure 8-13 and Table 8-6. By comparing the IT result of the samples prepared in the same way, it is observed that although the stress-strain curve slope is relatively stable, the peak load and the corresponding displacement of each sample vary. This indicates that the IHI and DI give a more stable estimation of the rock sample strength regardless of the variation of the failure point.

The IHI and DI and their Coefficient of Variation (CoV) were plotted in Figure 8-15. By comparing the IT result of granite samples prepared in different ways, it is noticed that the IHI and DI (of sample types 1 and 2) do not present significant variance if the sample was prepared with confinement (concrete casting or metal strip). If the sample had no concrete casting or metal strip (sample type 3), both IHI and DI were lower than the confined samples (sample types 1 and 2). The IHI and DI of the RLM (sample type 4) were lower than the granite (sample type 1), due to the difference in the UCS.

On the other hand, the CoV of the IHI and DI increased when a lower confinement condition was applied. For granite, the minimum CoV of the IHI and DI occurred when the granite was prepared with both concrete casting and metal strip, and the maximum CoV was observed when the granite had confinement. For all four sample types, the CoV of DI was consistently lower than that of IHI, which indicates that the DI presents a more stable rock strength characterization than the IHI regardless of the sample confinement and lithology. The DI CoV, however, was kept almost constant for granite with both casting and strip (sample type 1) and granite with only strip (sample type 2). It is shown that the metal strip

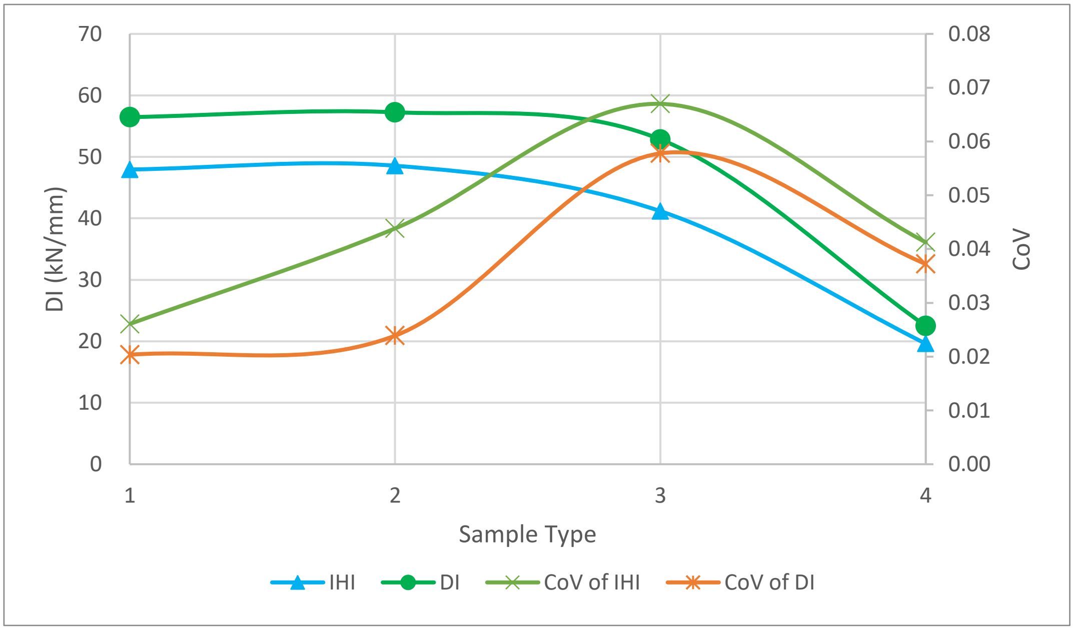

Figure 8-15 Comparison of IHI and DI and their CoVs of differently prepared sample

confines the rock core, and the CoV of DI keeps a low level (<0.02). Thus it is recommended that for the UCS estimation using IHI, the sample should be striped and not required to be cast. Otherwise, if the UCS is estimated from the IHI, the sample should be both casted and striped.

As shown in Table 8-2 to

Table 8-5, the CoV of the predicted UCS using the drillability index for RLM is similar to that of the indentation index. On the other hand, for granite, the standard deviation is significantly lower than that of the indentation index method. Thus, it can be concluded that the drillability index calculation method presents better stability for the UCS prediction result.

Based on the test results of the Granite and RLM with both concrete casting and metal strip, using the general form discussed previously, the correlation between the IHI and the UCS is fitted as:

$$UCS = 3.13 \times IHI + 17.53 \tag{8-8}$$

By substituting IHI with DI, a modified UCS prediction equation is presented correlated with the new method:

$$UCS = 2.61 \times DI + 20.19 \tag{8-9}$$

The new equation has modified coefficients compared to that of the IHI-UCS correlation. The main reason for the modification is that the IHI calculated from the new method is higher than the traditional method due to the inherent feather of the nonlinear region (region 1) in the curve. This new method can potentially improve the accuracy of the result for the UCS prediction because of the stability and the high certainty of the IHI calculation. Please note that this model is developed based on the granite (representing high strength volcanic rock) and RLM (representing medium strength rock), thus the accuracy of this model has not been validated for other lithologies obtained from other locations. It is recommended that the influence of lithology and the rock location on the UCS prediction accuracy should be considered in the future study.

8.8 Disk cutter drilling laboratory experiment and ROP prediction using the IHI and DI

In the previous study, Kahraman et al. (2000) developed a correlation between the drillability index and the ROP of the roller cone bit. For the conical bit-tooth and spherical bit-tooth, the ROP is estimated as:

$$ROP_{(Conical)} = 3.20 \times \frac{NW}{\alpha D} \tag{8-10}$$

$$ROP_{(Spherical)} = 3.35 \times \frac{NW}{\alpha D} \tag{8-11}$$

Where ROP is the rate of penetration (m/h), N is the rotational speed (rpm), W is the Weight on Bit (WOB) (kN), a the Drillability Index (DI) (kN/mm), and D is the bit diameter (cm). In this model, except for the drilling performance (WOB, bit diameter, and rotational speed), the shape of the bit and the rock's mechanical properties dominate the ROP. The DI in this model characterizes the rock's mechanical properties.

This study conducted a series of single cutter (triple disk) drilling laboratory tests on the granite block. The granite blocks prepared for the experiment were cut into 45cm x 45cm x 45cm cubic and grinded for

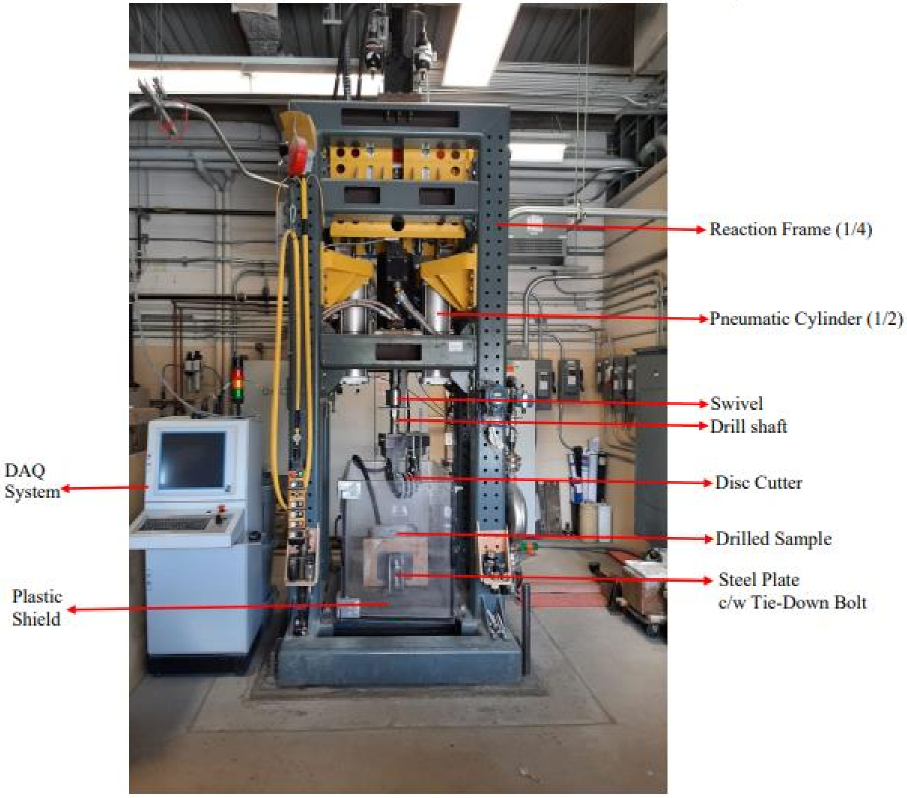

Figure 8-16 Experimental Drilling System

smooth surfaces, as shown in Figure 8-17. The mechanical properties of the granite are given in Table 8-2 since the granite used in the IT, and the drilling tests came from the same batch. The disc cutter used for this drill-off test is the cylindrical tri-disc disc cutter with a pressure compensator, whose features are shown in Table 8-7 below.

Table 8-7 Configuration of the disc cutter used in the drilling test

Number of Discs	3 (in an integral body)
Diameter	180mm
Cutter Type	Tungsten Carbide Inserts in a Matrix Body
Height of insert	5mm
Max Allowable Thrust	69.9KN
Included Angle (deg)	102.5

In the drilling experiment, different drilling bit rotary speeds (6.9-9.1 rpm), WOB (4.9-21.8 kN), and disk offset (6cm, 8cm, and 10 cm) were tested. The disk offset represents the offset between the center of rotation and the middle disc, as shown in Figure 8-18. The drilling experiment setup is given below:

Based on the single cutter (triple disk) drilling on the granite block lab test, the ROP prediction correlation based on the IHI and DI was developed. The form of the correlation is proposed as follows:

$$ROP = DE \times \frac{N \times WOB}{DI} \tag{8-12}$$

Where DE is the Drilling Efficiency parameter, which corresponds to the bit shape, diameter, wear-out condition, friction coefficient, and other physical properties which influence the drilling efficiency; N is the rotary speed (rpm); WOB is the weight on bit (kN), and DI is the drillability index (kN/mm).

The DE is calculated for different disk cutter diameters to summarize the experiment result.

Table 8-8 ROP prediction using IHI and DI of Single disk drilling on granite

Drilling efficiency coefficient (DE)					
	Disk diameter	6cm	8cm	10cm	Average
Predicted UCS	IHI	0.0096	0.0085	0.0097	0.0093
	DI	0.0127	0.0112	0.0128	0.0122

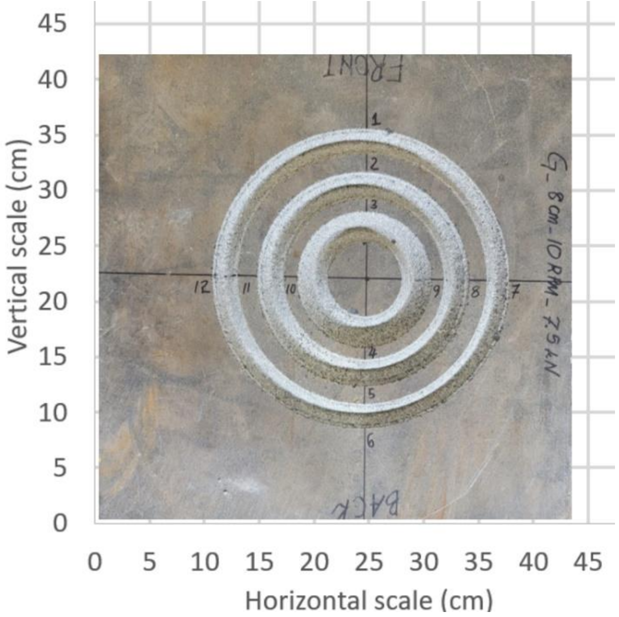

Figure 8-18 Plan view of a rock sample after disc cutter drilling test with an 8cm offset. The edge length of the sample in the picture is smaller than 45cm, because the picture is cropped.

Figure 8-17 : Granite Block Set Up for Drilling Experiment

It is noticed that the DI gives a higher DE number than the IHI. The limitation of this UCS prediction correlation is that it only considers one drill bit setup. In addition, this correlation has not been validated on other lithologies but granite. Thus, the DE should be calibrated when the drill bit setup changes since it represents the drilling performance-related drill bit properties.

8.9 PFC numerical simulation on IT test

PFC2D is a DEM software that is widely used to solve a variety of geotechnical problems. In this investigation, PFC2D is used to mimic the mechanical behavior of the rock model, which is conceptualized as an assembly of distinct particles adhered together at each contact point. In order to perform macro-parameter calibration operations in PFC simulations, it is necessary to make an accurate selection of the micro-parameters related to the particles and bonds, in addition to performing several iterations of trial and error methods. In this particular investigation, the material calibration indicator parameters are determined using the UCS result, Young's modulus, and Poisson's ratio. In this simulation, both the RLM and the granite are modeled as simulations and both models are determined.

A set of springs with normal and shear stiffness in the particles' contact bond can be imagined as the chosen Bond Particle Model (BPM), which is a parallel bond model. Particles that move with respect to one another create tension and torque. If these forces are more significant than the limits of the bonds' strength, the ties will rupture.

The finalization phase follows the packing phase in the model creation process. During the packing step, the linear contact model has fitted at all grain-grain interactions, and PFC walls were created to stop the balls from escaping the container. The servomechanism likewise managed the vessel walls' movement. The contacts were then given the linear parallel bond model and particle material properties during the finalization process, and the connected ball assembly was eventually obtained.

The model's physical and micromechanical parameters must be supplied when performing a uniaxial compression test to calibrate the micromechanical properties of limestone. Radius multiplier, effective modulus, stiffness ratio, frictional coefficient, the mean value of normal and tangential parallel bond strength, the standard deviation of normal and tangential parallel bond strength, parallel bond mean value, and parallel bond stiffness ratio are all examples of micromechanical parameters.

In this study, the PFC synthetic rock model was developed against the RLM material in the IT using the parallel bond model. During the material calibration, besides the micro parameters mentioned above, the effect of the particle size on the macro parameters was also analyzed. Following the suggestions of Xu et al. (2020), specific relationships between micro properties were adopted to simplify the matrix of the micro properties. In this study, the particle elastic modulus equals the parallel bond elastic modulus, the particle stiffness ratio equals the parallel bond stiffness ratio, the parallel bond normal strength equals five times of parallel bond tangential strength, the maximum particle size is 1.66 times the minimum particle size, and the radius multiplier was set to 1. In the material calibration, compression and tensile tests were conducted in PFC to measure the macro properties of the synthetic rock model. At different particle size ranges, the macro properties of the synthetic rock model were calibrated to match those of the RLM mechanical properties lab test result. The rock material calibration result of different particle size ranges is summarized in Table 8-9.

Table 8-9 RLM material calibration micro properties different particle size ranges

Sample	Macro Properties			Micro Properties			
	UCS (MPa)	E (GPa)	Poisson's Ratio	Ball size range (mm)	Parallel bond stiffness ratio	Parallel bond elastic modulus (10^9)	Parallel bond tangential strength (10^6)
Lab Test	78.98	9.68	0.21	N/A			
Simulation 1	79	9.8	0.24	1.0-1.66	1.7	7.7	50
Simulation 2	78	9.7	0.22	1.5-2.49	1.7	7.5	51
Simulation 3	81	10	0.21	2.0-3.32	1.7	7.8	48
Simulation 4	79	9.6	0.2	2.5-4.15	1.7	7.6	50

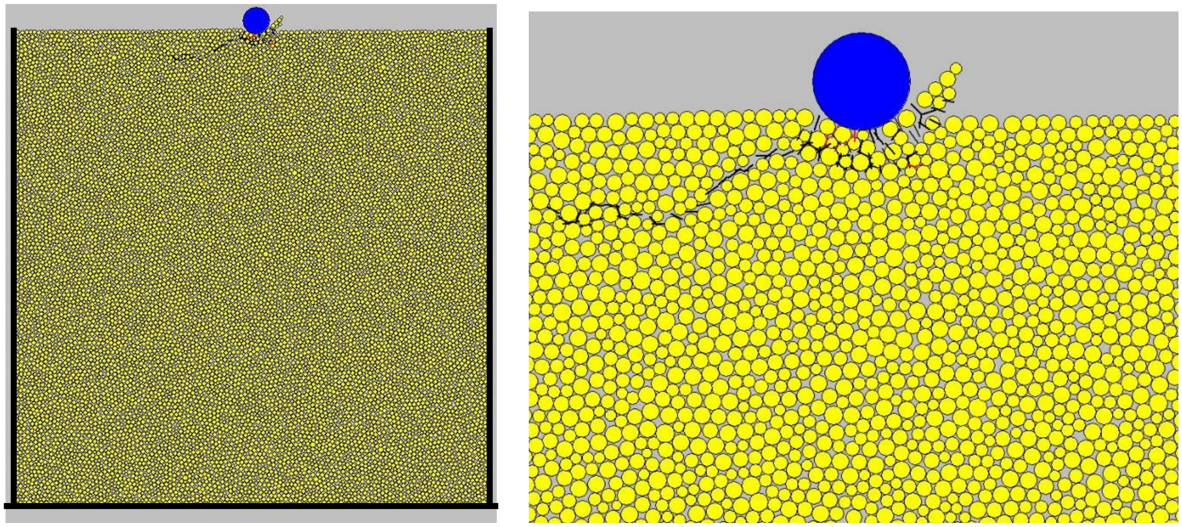

Figure 8-19 IT simulation using PFC2D visualization. The blue ball represents the downward travelling indenter; the yellow balls represent the RLM model; the black short lines represent the tensile micro fracture and the short red lines represent the shear micro fracture

Four rock models were calibrated in PFC2D with different particle size ranges. It is observed that the differences in the micro properties between the rock model are not significant, while the macro properties are similar. Thus, it is concluded that in the ball size range from 1.0-1.66mm to 2.5-4.15mm, the micro properties do not significantly vary with the ball size.

The simulation visualization result of the granite indentation test is given below in Figure 8-19. The rock model consists of yellow particles as a synthetic rock model. The sample was set on a bottom plate and surrounded by two walls representing the metal strap of the sample. The blue indenter was controlled to travel downward to make the indentation at a fixed displacement rate. The downward movement of the indenter crushed the rock at stopped at 1.8mm displacement, which agrees with the laboratory test. Due to the confinement of the walls, no major crack is formed, splitting the sample during the indentation process. In Figure 8-19, the short black lines represent the tensile micro fracture, and the short red lines represent the shear micro fracture. It is observed that the plastic deformation region is formed below the indenter, indicating that the failure zone's volume is larger than the intrusion of the metal indenter. A side crack was observed on the left of the indenter. On the right of the indenter, the chipping phenomenon was identified.

Both side cracks and chipping were observed in the lab test. The dominant fracture propagating throughout the sample was not obtained in the PFC simulation. The reason should be that the stiffness of the side confining wall is high, and the significant fracture development was restrained.

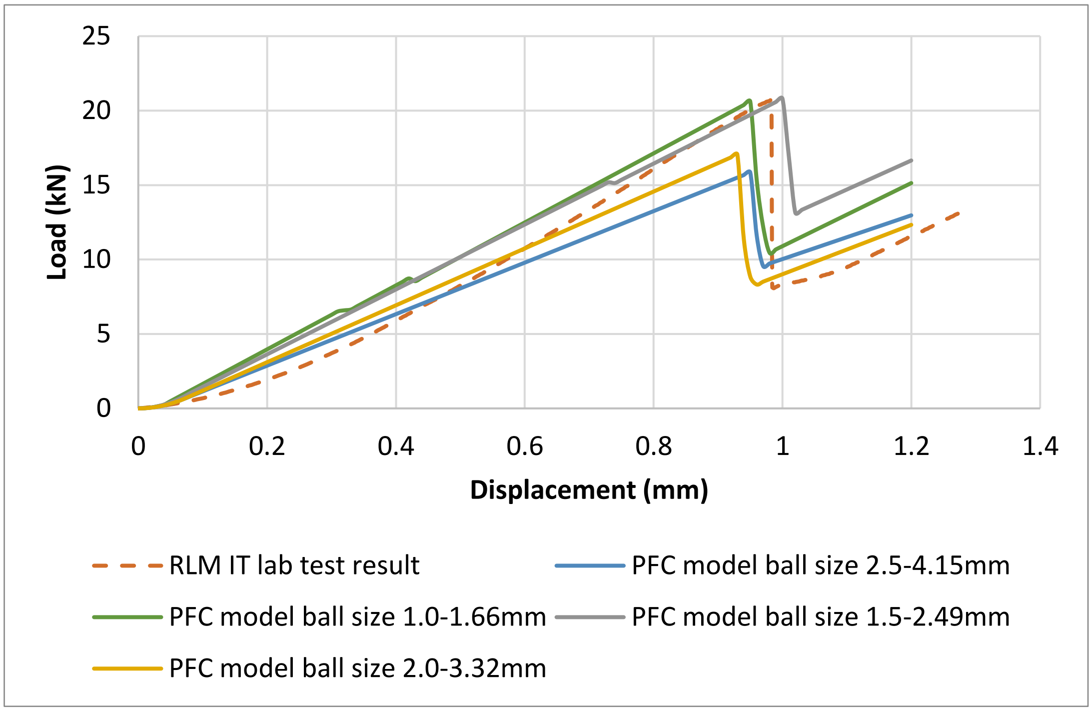

Figure 8-20 PFC IT test results with different ball size range comparison with the IT lab test result

Figure 8-20 compares the PFC IT test results with the IT lab test result. It is observed that the IT performance of the synthetic rock model varies with the ball size range, although they have similar UCS, Young's modulus, and Poisson's ratio. The displacement at the peak load point differs due to the randomness of the rock model formation. The slope of the simulated stress-strain curve increased with the decrease in the ball size. It is noticed that region #1 of the simulation result, where the slope near the zero point rapidly built up with the displacement increase, was smaller than the lab test result. In this situation, the IHI and DI of the simulation result can be regarded as the same value. It is suggested that the slope of the simulation result should match the DI of the lab test result, since the low slope less influences the calculation of DI in region #1. In this study, the ball size range of the synthetic rock model is suggested to be 1.5-2.49mm.

Due to the uncertainty in microscopic parameters and macroscopic responses, calibration of macroscopic and microscopic parameters must be done first. A well-liked calibration technique is the method of trial and error. Based on a series of PFC rock model calibration tests, Xu et al. (2020) proposed a connection between the micro and macro parameters of the rock model. Effective modulus and stiffness ratio are negatively correlated with elastic modulus. The stiffness ratio and Poisson's ratio are connected. UCS is inversely related to effective modulus and stiffness ratio and positively correlated with the mean value of parallel bond normal strength.

Zhou et al. (2011) and Xu et al. (2020) proposed that particle size influences the macro properties of the PFC rock model. When the particle size is below a certain level, its influence on the macro properties can be ignored. A definition of the resolution of a dimension RES was proposed as:

$$RES = (L/R_{min})[1/(1 + R_{max}/R_{min})] \tag{8-13}$$

Where L is the minimum size of the model, R_{max} and R_{min} are the max and min radius of the ball.

Zhou et al. (2011) and Xu et al. (2020) suggested that the ball size has a negligible effect on the macro properties when the RES≥10. In this study, the R_{max} equals 1.66 times the R_{min}, and the minimum size of the model is around 5cm. Thus, according to the RES criteria, the ball size has little influence on the macro properties if the R_{min} is below 2mm. In this study, the ball size range ranges from 1.0-1.66mm to 2.5-4.15mm, where the RES ranges from 7.5-19. The regular macro properties (UCS, Young's modulus, and Poisson's ratio) change slightly with the ball size in this range, while the IT result slope increases with the ball size decrease. It is concluded that the RES criterion of RES≥10 is strict enough to ensure the influence of ball size on the regular macro properties (UCS, Young's modulus, and Poisson's ratio) can be ignored. However, the IT performance keeps changing in the RES ranges from 7.5-19. Thus, the RES threshold for IT performance requires further study.

8.10 Conclusions

Prediction of rock strength from indirect tests instead of the traditional UCS test is valuable and cost-effective, especially for the highly fractured geology condition. This study investigated the predictability of the UCS of rocks from IT tests performed on 2-inch diameter rock cores. Comparing to the previous IT test, the sample preparation was suggested that the metal strip should be used because it enhances the repeatability of the IT test result. The lateral confinement of the rock core sample was recommended to enhance the quality of the IT result. The metal strip only confinement condition presented a similar performance to the confinement with concrete casting and a metal strip.Based on the optimized sample preparation, the UCS prediction model using the IT test result was developed, and the deviation of the result is relatively low. Correlation to predict UCS from IT results was developed from the IT test results of granite and RLM. It is suggested that the DI should be used for the UCS prediction since the DI presented a lower CoV than the IHI. The DEM simulation using PFC revealed that the slope of the IT simulation stress-strain curve increased with the decrease of the synthetic rock model's ball size. In the DEM simulation, the ball size of the synthetic rock model should be calibrated for IT or other forms of rock crushing tests.

Chapter 9: Conclusions and recommendations

9.1 Summary

This thesis investigates rock characterization from the point of view of EM properties and mechanical properties. In terms of EM property characterization, the availability of a mono-borehole GPR system for directional imaging of subsurface targets was verified, a practical and economical method for estimating the EM wave velocity and RDP of the NQ size rock core was proposed, and its accuracy was determined to be acceptable for field testing. An imaging fluid was developed to mitigate the effect of groundwater on borehole GPR signal quality. For mechanical property characterization, models were developed to predict the in-situ strength and gold grade of the mining field using the rotary percussion drilling performance data collected by a handheld data acquisition system. Correlations were also presented to predict UCS from the IT results. The optimal sample preparation procedures were proposed. The ball size range was suggested to be an important micro-parameter of the PFC rock model calibration, which influences the rock model failure performance due to crushing.

9.2 Concluding Remarks and Highlights

Concluding remarks and highlights of each chapter are given below.

9.2.1 Conclusion and highlights from Chapter 4

This study proposes a practical and rapid method for measuring rock dielectric permittivity. This method used a 2.3 GHz GPR system specifically designed for NQ-size cores, which is one of the most common rock core sizes for core drilling activities. The RDP result obtained by the GPR system, the open coaxial probe based system, and the literature result were compared and the accuracy of the GPR system was demonstrated. It was found that ignoring the electrical conductivity and magnetic susceptibility of the rock results in an average error of 0.79. The RDP for the vein (quartz) / host rock (mafic volcanic) was determined to be 4.1-4.7 and 6.5-8.6. The difference in dielectric between the vein and the host rock proves that it is possible to distinguish between the vein and the host by borehole GPR.

FDTD simulation using gprMAX was used to study the EM wave propagation path in the NQ core. It was observed that the wave path was complicated due to the reflection on the side of the core. By comparing the laboratory experiment result and the simulation result, the optimum NQ core length is proposed to be 15cm to 30cm, which is a safe choice for most lithologies. For the 40mm antenna separation, the GPR center frequency is suggested to be not lower than 1.5GHz to avoid the interference of direct arrival and improve the measurement resolution.

9.2.2 Conclusion and highlights from Chapter 5

Based on the field trial results and analysis, we believe that the 1GHz GPR has potential for downhole imaging. The primary reflection shows a penetration depth of 1.8m, which is generally satisfactory. The primary reflections are consistent with the gold ore quartz vein interface and the volcanic mafic host rock. At the same time, some issues will be resolved in the future. For example, there are some unexpected reflections collected in the field tests. It is recommended that more geotechnical and geological studies be done before the imaging survey. The image quality is not satisfactory enough due to the limitation of the field equipment. It is suggested that the speed of the antenna should be low enough to ensure a high number of stacks and thus a high signal-to-noise ratio. Multiple surface reflections are observed in the images at shallow depth.

9.2.3 Conclusion and highlights from Chapter 6

This work introduced a novel imaging fluid formulation. Prior to borehole GPR scanning, the imaging fluid was intended to replace the groundwater in the borehole and improve the GPR signal quality. The ingredients of the imaging fluid included stearic acid, barite, and canola oil as a fluid base (viscosity improver). Through laboratory testing, the imaging fluid was found to have an acceptable RDP (2.7), extremely low electrical conductivity (0.001mS/cm), density (1.2 g/cm3), and good underwater stability. Numerous laboratory experiments, computer simulations and field tests were conducted. It was found that the imaging fluid, which replaced the borehole groundwater, solved the GPR signal problem. One day after the imaging fluid was pumped in and filled the borehole, as opposed to the day the borehole was filled with groundwater, a significant improvement in GPR signal quality was observed. This was confirmed during the field test. The imaging fluid was found to successfully improve borehole GPR in the water-filled borehole.

As a practical solution for the field application of borehole GPR, the new fluid has the following four advantages

a) Appropriate relative dielectric permittivity and low attenuation coefficient

b) Higher density than water

c) Stability underwater

d) Non-toxicity recipe

9.2.4 Conclusion and highlights from Chapter 7

In this study, a DAQ system was developed to collect real-time drilling performance data from the rotary percussive drilling rig. Inverse relationships between drilling performance parameters (rotation pressure and damping pressure) and ROP were developed. Using the real-time drilling performance data, an analytical model was built to predict the in-situ UCS of the formation using drilling parameters based on the concept of PI, and the correlation for in-situ gold grade estimation was developed.

9.2.5 Conclusion and highlights from Chapter 8

Especially in highly fractured geology, predicting rock strength using indirect tests rather than the conventional UCS test is essential and cost effective. This study investigated the predictability of rock UCS using IT tests on 2-inch diameter rock cores. Granite and RLM IT test data were used to develop a correlation to predict UCS from these results. Since the DI had a lower CoV than the IHI, it is recommended that it be used for UCS prediction. To improve the quality of the IT result, lateral confinement of the rock core sample was recommended. The confinement with concrete casting and a metal strip performed similarly to the metal strip-only confinement condition. The DEM simulation using PFC showed that as the ball size of the synthetic rock model decreased, the slope of the stress-strain curve in the IT simulation increased. The ball size of the synthetic rock model in the DEM simulation must be calibrated for IT or other types of rock fracture tests.

9.3 Recommendations for Future Work

Based on the current research, some recommendations can be proposed:

1. The design of the GPR system used for the dielectric permittivity measurement should be improved to reduce the system noise level and enhance the signal-to-noise ratio.

2. The new water-oil mixture liquid phase recipe could be developed based on the current pure oil-based imaging fluid recipe. Because the water content could increase the dielectric permittivity of the imaging fluid, the dielectric permittivity is closer to that of the rock. In addition, water content allows the application of water-based viscosity modifiers and other additives, which can enhance the imaging fluid's rheology and stability.

3. In this study, the in-situ UCS was predicted using the Percussive Index (PI) value which was obtained from concrete. In the future, the PI can be determined specifically for the rock type encountered in the field. Thus, the accuracy of the in-situ UCS estimation will be improved.

4. Regarding the DEM modeling of the indentation test, the flat-joint model can be introduced to build the rock model in the simulation. It is because the rock model built by the flat-joint model presents a more realistic tensile strength than the current parallel-bond model, and the simulation's accuracy could be further improved. I

5. Currently, the UCS prediction model using IT results is derived from the result of two different rocks. The indentation test should be conducted on more samples with different lithologies in the future to optimize the reliability and applicability of the model.

6. The XRD and MLA tests can be used together with the indentation test. MLA delivers a quantitative mineral content result of the rock sample, while XRD is more accurate when identifying minerals with different crystal structures. The rock mineral content and micro-grain crystal structure are directly related to the rock macro strength. Thus the analytical model can be developed between the indentation test result (rock strength) and rock micro properties (mineral content and mineral micro-grain crystal structure) if the indentation test result and the XRD and MLA test result are coupled.

Reference List

Abdelmalik, A.A., 2014. Charge dynamics in vegetable oil-based ester dielectric fluid. Br. J. Appl. *Sci. Technol. 4* (2), 371–386.

Agarwal, V. K., & Ichijo, B. (1977). Determination of dielectric constant of stearic acid films using varying gap immersion method. *Electrocomponent science and technology*, *4*(1), 23-28.

Al-Jaroudi, S. S., Ul-Hamid, A., Mohammed, A. R. I., & Saner, S. (2007). Use of X-ray powder diffraction for quantitative analysis of carbonate rock reservoir samples. *Powder Technology*, *175*(3), 115-121.

Altun, A. O., Yilmaz, I., & Yildirim, M. (2010). A short review on the surficial impacts of underground mining. Sci Res Essays, 5(21), 3206-3212.

ASTM D5731-16 (2016). Standard Test Method for Determination of the Point Load Strength Index of Rock and Application to Rock Strength Classifications. *American Society for Testing and Materials*

ASTM D6432-19 (2019). Standard guide for using the surface ground penetrating radar method for subsurface investigation. *American Society for Testing and Materials*

ASTM D7012-13 (2013) Standard test methods for compressive strength and elastic moduli of intact rock core specimens under varying states of stress and temperatures, *American Society for Testing and Materials*

Annan, A.P., 2002, The history of ground penetrating radar. *Subsurface Sensing Technologies and Applications, Vol. 3,* No. 4, October 2002, pp. 303–320.

Bakar, M. A., Butt, I. A., & Majeed, Y. (2018). Penetration Rate and Specific Energy Prediction of Rotary–Percussive Drills Using Drill Cuttings and Engineering Properties of Selected Rock Units. *Journal of Mining Science, 54*(2), 270-284.

Baker-Jarvis, J., Vanzura, E. J., & Kissick, W. A. (1990). Improved technique for determining complex permittivity with the transmission/reflection method. *IEEE Transactions on microwave theory and techniques, 38*(8), 1096-1103.

Bano, M. (2004). Modeling of GPR waves for lossy media obeying a complex power law of frequency for dielectric permittivity. *Geophysical Prospecting, 52*(1), 11-26.

Barton, N., Lien, R., & Lunde, J. (1974). Engineering classification of rock masses for the design of tunnel support. *Rock mechanics, 6*(4), 189-236.

Benedetto, A., & Pajewski, L. (Eds.). (2015). *Civil engineering applications of ground penetrating radar*. Springer.

Beres, M., Green, A., Huggenberger, P., & Horstmeyer, H. (1995). Mapping the architecture of glaciofluvial sediments with three-dimensional georadar. *Geology, 23*(12), 1087-1090.

Bieniawski, Z. (1988). The rock mass rating (RMR) system (geomechanics classification) in engineering practice. In *Rock Classification Systems for Engineering Purposes*. ASTM International.

Binley, A., Winship, P., West, L. J., Pokar, M., & Middleton, R. (2002). Seasonal variation of moisture content in unsaturated sandstone inferred from borehole radar and resistivity profiles. *Journal of Hydrology, 267*(3-4), 160-172.

Bobrov, P. P., Lapina, A. S., & Repin, A. V. (2015, July). Effect of the rock/water/air interaction on the complex dielectric permittivity and electromagnetic waves attenuation in water-saturated sandstones. In *PIERS Proceedings* (pp. 1877-1879).

Booth, A. D., Emir, E., & Diez, A. (2016). Approximations to seismic AVA responses: Validity and potential in glaciological applications. *Geophysics, 81*(1), WA1-WA11.

Borchert, O., Behaimanot, K., & Glasmachers, A. (2009). Directional borehole radar calibration. Journal of applied geophysics, 67(4), 352-360.

Bristow, C. S., & Jol, H. M. (Eds.). (2003). *Ground penetrating radar in sediments*. Geological Society of London.

Campbell, M. J., & Ulrichs, J. (1969). Electrical properties of rocks and their significance for lunar radar observations. *Journal of Geophysical Research, 74*(25), 5867-5881.

Carpinteri, A., & Invernizzi, S. (2005). Numerical analysis of the cutting interaction between indenters acting on disordered materials. *International journal of fracture, 131*(2), 143-154.

Cassidy, N. J. (2007). Evaluating LNAPL contamination using GPR signal attenuation analysis and dielectric property measurements: Practical implications for hydrological studies. J*ournal of Contaminant Hydrology, 94*(1-2), 49-75.

Chang, P. C. (2011). Physics-based inverse processing and multi-path exploitation for through-wall radar imaging (Doctoral dissertation, The Ohio State University).

Chen, L. F., Ong, C. K., Neo, C. P., Varadan, V. V., & Varadan, V. K. (2004). Microwave electronics: measurement and materials characterization. John Wiley & Sons.

Chen, L. H., & Labuz, J. F. (2006). Indentation of rock by wedge-shaped tools. International Journal of Rock Mechanics and Mining Sciences, 43(7), 1023-1033.

Chitty, D. E., Blouin, S. E., Zimmer, V. L., Thompson, P. H., & Tremba, E. L. (2005, January). Rotary percussion sounding system for in situ rock mass characterization. In *Alaska Rocks 2005, The 40th US Symposium on Rock Mechanics (USRMS)*. American Rock Mechanics Association.

Cho, Y., Dolan, S. S., Saxena, N., & Das, V. (2022). Estimation of Water Saturation in Shale Formation Using In Situ Multifrequency Dielectric Permittivity. *Geofluids*, *2022*.

Colone, F., Cardinali, R., & Lombardo, P. (2006, April). Cancellation of clutter and multipath in passive radar using a sequential approach. In 2006 IEEE Conference on Radar (pp. 1-7). IEEE.

Concrete Society, \Concrete society; guidance on radar testing of concrete structures," Tech. Rep., Vol. 48, 88, 1997.

Copur, H., Bilgin, N., Tuncdemir, H. & Balci, C. (2003). A set of indices based on indentation tests for assessment of rock cutting performance and rock properties. *Journal of the Southern African Institute* *of Mining and Metallurgy, 103*(9), 589-599.

Costa, F., Borgese, M., Degiorgi, M., & Monorchio, A. (2017). Electromagnetic characterisation of materials by using transmission/reflection (T/R) devices. *Electronics, 6*(4), 95.

Dang, L., Yang, H., & Teng, B. (2018). Detection imaging of impulse borehole well-logging radar. *EURASIP Journal on Image and Video Processing, 2018*(1), 1-14.

Davis, J. L., & Annan, A. P. (1989). Ground‐penetrating radar for high‐resolution mapping of soil and rock stratigraphy 1. *Geophysical prospecting, 37*(5), 531-551.

De Chiara, F., Fontul, S., & Fortunato, E. (2014). GPR laboratory tests for railways materials dielectric properties assessment. *Remote Sensing*, *6*(10), 9712-9728.

Deere, D. (1988). The rock quality designation (RQD) index in practice. In *Rock classification systems for engineering purposes*. ASTM International.

Di Meo, S., Iliopoulos, I., Pasian, M., Ettorre, M., Pasotti, L., Zhadobov, M., & Matrone, G. (2019, March). Tissue mimicking materials for breast phantoms using waste oil hardeners. In *2019 13th European Conference on Antennas and Propagation (EuCAP)* (pp. 1-4). IEEE.

Dominy, S. C., Annels, A. E., Camm, G. S., Wheeler, P., & Barr, S. P. (1997). Geology in the resource and reserve estimation of narrow vein deposits. Exploration and Mining Geology, 4(6), 317-333.

Dominy, S. C., Camm, G. S., & Phelps, R. F. (2020). Narrow vein mining—A challenge to the operator. In Mine Planning and Equipment Selection 1997 (pp. 125-132). CRC Press.

Dou, Q., Wei, L., Magee, D. R., & Cohn, A. G. (2016). Real-time hyperbola recognition and fitting in GPR data. *IEEE Transactions on Geoscience and Remote Sensing, 55*(1), 51-62.

Ebihara, S., Hideharu, H., & Takashi, O. (2010, June). Influence of feed line on DOA estimation with dipole array antenna for directional borehole radar. In *Proceedings of the XIII Internarional Conference on Ground Penetrating Radar* (pp. 1-6). IEEE.

Penetrating Radar (GPR2010), LECCE, Vol. I, pp. 810–815 Ellefsen, K. J., & Wright, D. L. (2005). Radiation pattern of a borehole radar antenna. *Geophysics*, *70*(1), K1-K11.

El-Said, M. A. H. (1956). Geophysical prospection of undergroundwater in the desert by means of electromagnetic interference fringes. *Proceedings of the IRE*, *44*(1), 24-30.

Feely, M., Wilton, D. H., Costanzo, A., Kollar, A. D., Goudie, D. J., & Joyce, A. (2019). Mineral Liberation Analysis and Scanning Electron Microscopy of Connemara Marble: New Mineral Distribution Maps of an Iconic Irish Gem Material. *Journal of Gemmology*, *36*(5).

Forte, E., & Pipan, M. (2017). Review of multi-offset GPR applications: Data acquisition, processing and analysis. *Signal processing, 132*, 210-220.

Forte, E., Dossi, M., Pipan, M., & Colucci, R. R. (2014). Velocity analysis from common offset GPR data inversion: theory and application to synthetic and real data. *Geophysical Journal International, 197*(3), 1471-1483.

Francke, J. (2012). A review of selected ground penetrating radar applications to mineral resource evaluations. *Journal of Applied Geophysics, 81*, 29-37.

García-Baños, B., Catalá-Civera, J. M., Canós, A. J., & Peñaranda-Foix, F. (2005). Design rules for the optimization of the sensitivity of open-ended coaxial microwave sensors for monitoring changes in dielectric materials. *Measurement Science and Technology, 16*(5), 1186.

Ghodgaonkar, D. K., Varadan, V. V., & Varadan, V. K. (1989). A free-space method for measurement of dielectric constants and loss tangents at microwave frequencies. IEEE Transactions on Instrumentation and measurement, 38(3), 789-793.

Gilson, E. W., Redman, J. D., Pilon, J., & Annan, A. P. (1996, January). Near surface applications of borehole radar. In *Symposium on the Application of Geophysics to Engineering and Environmental Problems 1996* (pp. 545-553). Society of Exploration Geophysicists.

Gnirk, P. F., & Cheatham, J. B. (1965). An experimental study of single bit-tooth penetration into dry rock at confining pressures 0 to 5,000 psi. *Society of Petroleum Engineers Journal*, *5*(02), 117-130.

Goldstein, J. I., Newbury, D. E., Echlin, P., Joy, D. C., Fiori, C., & Lifshin, E. (1981). Coating Techniques for SEM and Microanalysis. In *Scanning Electron Microscopy and X-Ray Microanalysis* (pp. 461-494). Springer, Boston, MA.

Grant, D. C., Goudie, D. J., & Baird, E. (2018). Analysis of 98 individual− 200 mesh iron ore samples in a single scanning electron microscope-automated mineralogy session. *Applied Earth Science*, *127*(1), 38-43.

Grant, D. C., Goudie, D. J., & Baird, E. (2018). Analysis of 98 individual− 200 mesh iron ore samples in a single scanning electron microscope-automated mineralogy session. *Applied Earth Science, 127*(1), 38-43.

Grant, D. C., Goudie, D. J., & Baird, E. (2018). Analysis of 98 individual− 200 mesh iron ore samples in a single scanning electron microscope-automated mineralogy session. *Applied Earth Science, 127*(1), 38-43.

Grant, D. C., Goudie, D. J., Shaffer, M., & Sylvester, P. (2016). A single-step trans-vertical epoxy preparation method for maximising throughput of iron-ore samples via SEM-MLA analysis. *Applied Earth Science*, *125*(1), 57-62.

Grasmueck, M., Weger, R., & Horstmeyer, H. (2005). Full-resolution 3D GPR imaging. *Geophysics*, *70*(1), K12-K19.

Gregoire, C., Joesten, P. K., & Lane Jr, J. W. (2006). Use of borehole radar reflection logging to monitor steam-enhanced remediation in fractured limestone—Results of numerical modeling and a field experiment. *Journal of applied geophysics, 60*(1), 41-54.

Grote, K., Anger, C., Kelly, B., Hubbard, S., & Rubin, Y. (2010). Characterization of soil water content variability and soil texture using GPR groundwave techniques. *Journal of Environmental & Engineering Geophysics*, *15*(3), 93-110.

Gueting, N., Vienken, T., Klotzsche, A., van der Kruk, J., Vanderborght, J., Caers, J., ... & Englert, A. (2017). High resolution aquifer characterization using crosshole GPR full-waveform tomography:

Comparison with direct-push and tracer test data. *Water Resources Research*, *53*(1), 49-72.

Guo, C., Ling, B., Mavko, G., & Liu, R. (2019). Effect of microgeometry on modeling accuracy of fluid-saturated rock using dielectric permittivity. *IEEE Transactions on Geoscience and Remote Sensing, 57*(9), 7294-7299.

Haftani, M., Bohloli, B., Moosavi, M., Nouri, A., Moradi, M., & Javan, M. R. M. (2013). A new method for correlating rock strength to indentation tests. *Journal of Petroleum Science and Engineering*, *112*, 24-31.

Haftani, M., Bohloli, B., Nouri, A., Javan, M. R. M., Moosavi, M., & Moradi, M. (2015). Influence of penetration rate and indenter diameter in strength measurement by indentation testing on small rock specimens. *Rock Mechanics and Rock Engineering, 48*(2), 527-534.

Hamid, M. H. A., Ishak, M. T., Din, M. M., Suhaimi, N. S., & Katim, N. I. A. (2016, November). Dielectric properties of natural ester oils used for transformer application under temperature variation. In *2016 IEEE International Conference on Power and Energy (PECon)* (pp. 54-57). IEEE.

He, X. Q., Zhu, Z. Q., Liu, Q. Y., & Lu, G. Y. (2009, March). Review of GPR rebar detection. In *PIERS proceedings* (pp. 804-813).

Hiscock, K. M., & Bense, V. F. (2021). *Hydrogeology: principles and practice*. John Wiley & Sons.

Hood, M. and Roxborough, F.F. 1992. Rock breakage: mechanical. *SME Mining Engineering Handbook.* Society for Mining, Metallurgy and Exploration, Littleton, Colorado. pp. 680-721.

Huang, H., & Detournay, E. (2013). Discrete element modeling of tool‐rock interaction II: rock indentation. *International Journal for Numerical and Analytical Methods in Geomechanics, 37*(13), 1930-1947.

Huang, H., Damjanac, B., & Detournay, E. (1998). Normal wedge indentation in rocks with lateral confinement. *Rock Mechanics and Rock Engineering, 31(*2), 81-94.

Hubbard, S. S., Rubin, Y., & Majer, E. (1997). Ground‐penetrating‐radar‐assisted saturation and permeability estimation in bimodal systems. *Water Resources Research, 33*(5), 971-990.

Huisman, J. A., Hubbard, S. S., Redman, J. D., & Annan, A. P. (2003). Measuring soil water content with ground penetrating radar: A review. *Vadose zone journal, 2*(4), 476-491.

Huo, J., Zhou, B., Zhao, Q., & Mason, I. (2018). Suppressing reflected guided waves from contaminated borehole radar data. *IEEE Geoscience and Remote Sensing Letters, 16*(5), 736-740.

Igel, J., Günther, T., & Kuntzer, M. (2013). Ground-penetrating radar insight into a coastal aquifer: the freshwater lens of Borkum Island. *Hydrology and Earth System Sciences, 17*(2), 519-531.

ISRM (International Society for Rock Mechanics), Commission on standardization laboratory and field results. Suggested Method on Uniaxial Compressive Strength and Deformability of Rock Materials (2018 revised version)

Jacob, R. W., & Hermance, J. F. (2004). Assessing the precision of GPR velocity and vertical two-way travel time estimates. *Journal of Environmental & Engineering Geophysics, 9*(3), 143-153.

Jacob, R. W., & Urban, T. M. (2016). Ground‐penetrating radar velocity determination and precision estimates using common‐midpoint (CMP) collection with hand‐picking, semblance analysis and cross‐correlation analysis: A case study and tutorial for archaeologists. Archaeometry, 58(6), 987-1002.

Jannin, G., Kefi, S., & Legendre, F. (2014). Dielectric properties of nonaqueous drilling fluids from 1 MHz up to 20 GHz. *IEEE Transactions on Dielectrics and Electrical Insulation*, *21*(1), 217-224.

Jeannin, M., Garambois, S., Grégoire, C., & Jongmans, D. (2006). Multiconfiguration GPR measurements for geometric fracture characterization in limestone cliffs (Alps). *Geophysics*, *71*(3), B85-B92.

Jiang, J. H., & Wu, D. L. (2004). Ice and water permittivities for millimeter and sub-millimeter remote sensing applications. *Atmospheric Science Letters, 5*(7), 146-151.)

Jol, H. M. (Ed.). (2008). *Ground penetrating radar theory and applications*. Elsevier.

Jolliffe, I. T., & Cadima, J. (2016). Principal component analysis: a review and recent developments. *Philosophical transactions of the royal society A: Mathematical, Physical and Engineering Sciences, 374*(2065), 20150202.

Kahraman, S. A. İ. R., & Gunaydin, O. (2008). Indentation hardness test to estimate the sawability of carbonate rocks. *Bulletin of Engineering Geology and the Environment*, *67*(4), 507-511.

Kahraman, S. A. İ. R., Balcı, C., Yazıcı, S., & Bilgin, N. (2000). Prediction of the penetration rate of rotary blast hole drills using a new drillability index. *International Journal of Rock Mechanics and Mining Sciences*, *37*(5), 729-743.

Kahraman, S. A. İ. R., Fener, M., & Kozman, E. (2012). Predicting the compressive and tensile strength of rocks from indentation hardness index. *Journal of the Southern African Institute of Mining and Metallurgy*, *112*(5), 331-339.

Kahraman, S., Bilgin, N., & Feridunoglu, C. (2003). Dominant rock properties affecting the penetration rate of percussive drills. *International Journal of Rock Mechanics and Mining Sciences, 40*(5), 711-723.

Kalyan, B., Murthy, C. S., & Choudhary, R. P. (2015). Rock indentation indices as criteria in rock excavation technology–A critical review. *Procedia Earth and Planetary Science, 11*, 149-158.

Karaman, K. A. D. İ. R., Cihangir, F. E. R. D. İ., Ercikdi, B. A. Y. R. A. M., Kesimal, A. Y. H. A. N., & Demirel, S. (2015). Utilization of the Brazilian test for estimating the uniaxial compressive strength and shear strength parameters. *Journal of the Southern African Institute of Mining and Metallurgy, 115*(3), 185-192.

Keller, G. V. (2017). Electrical properties of rocks and minerals. In *Handbook of physical properties of rocks* (pp. 217-294). CRC Press.

Khodja, M., Khodja-Saber, M., Canselier, J. P., Cohaut, N., & Bergaya, F. (2010). Drilling fluid technology: performances and environmental considerations. *Products and services; from R&D to final solutions*, 227-256.

Kikuta, K., Yi, L., Zou, L., & Sato, M. (2019, July). Robust subsurface velocity change detection method with Yakumo multistatic GPR system. In IGARSS 2019-2019 *IEEE International Geoscience and Remote Sensing Symposium* (pp. 3582-3585).

Klein, O., Donovan, S., Dressel, M., & Grüner, G. (1993). Microwave cavity perturbation technique: Part I: Principles. *International Journal of Infrared and Millimeter Waves, 14*(12), 2423-2457.

Kovacs, A., & Morey, R. M. (1983). Detection of cavities under concrete pavement. *CRREL report*; 83-18, Cold Regions Research and Engineering Laboratory (U.S.)

Kumar, O. P., Kumar, P., Ali, T., Kumar, P., & Vincent, S. (2021). Ultrawideband antennas: Growth and evolution. *Micromachines, 13*(1), 60.

Kyzym, I. (2018). *Cuttings analysis in drilling performance evaluation and formation identification* (Doctoral dissertation, Memorial University of Newfoundland).

Latif, S. I.,, Tapia DF, Herrera DR, Nepote MS, Pistorius S, Shafai L. A directional antenna in a matching liquid for microwave radar imaging. *Int J Antennas Propag.* 2015;2015:1–8.

Lazaro, A., Lorenzo, J., Villarino, R., & Girbau, D. (2014). Backscatter transponder based on frequency selective surface for FMCW radar applications. Radioengineering, 23(2), 632-641.

Lazzari, M., De Giorgi, L., Ceraudo, G., & Persico, R. (2018). Geoprospecting survey in the archaeological site of Aquinum (Lazio, central Italy). *Surveys in Geophysics, 39*(6), 1167-1180.

Leão, T. P., Perfect, E., & Tyner, J. S. (2015). Evaluation of Lichtenecker's mixing model for predicting effective permittivity of soils at 50 MHz. Transactions of the ASABE, 58(1), 83-91.

Li, X. F., Li, H. B., Liu, Y. Q., Zhou, Q. C., & Xia, X. (2016). Numerical simulation of rock fragmentation mechanisms subject to wedge penetration for TBMs. *Tunnelling and Underground Space Technology, 53*, 96-108.

Li, Z., Xiao, Y., Pilgrim, R., Royce, J., and Butt, S. (2019). Subsurface rock interface imaging with Ground Penetrating Radar (GPR). In *the 72nd Canadian Geotechnical Conference*. Canadian Geotechnical Society (CGS)

Liu, H. (2004). *Numerical modelling of the rock fragmentation process by mechanical tools* (Doctoral dissertation, Luleå tekniska universitet).

Liu, Mao, Jhe-yu Lin, Cheng Lu, Kiet Anh Tieu, Kun Zhou, and Toshihiko Koseki. "Progress in indentation study of materials via both experimental and numerical methods." *Crystals* 7, no. 10 (2017): 258.

Liu, S., & Sato, M. (2006). Subsurface water-filled fracture detection by borehole radar: A case history. *Journal of Environmental & Engineering Geophysics, 11*(2), 95-101.

Liu, S., Wang, W., Fu, L., & Lu, Q. (2019). Linear prediction-based DOA estimation for directional borehole radar 3-D imaging. *IEEE Transactions on Geoscience and Remote Sensing, 57*(8), 5493-5501.

Liu, S., Wang, W., Fu, L., & Lu, Q. (2019). Linear prediction-based DOA estimation for directional borehole radar 3-D imaging. *IEEE Transactions on Geoscience and Remote Sensing, 57*(8), 5493-5501.

Lou, W., Zhang, D., & Bayless, R. C. (2020). Review of mineral recognition and its future. *Applied Geochemistry, 122*, 104727.

Lunt, I. A., Hubbard, S. S., & Rubin, Y. (2005). Soil moisture content estimation using ground-penetrating radar reflection data. J*ournal of hydrology, 307*(1-4), 254-269.

Ma, H., Yin, L., & Ji, H. (2011). Numerical study of the effect of confining stress on rock fragmentation by TBM cutters. *International Journal of Rock Mechanics and Mining Sciences*, *48*(6), 1021-1033.

Mansour, K., Basheer, A. A., Rabeh, T., Khalil, A., Eldin, A. E., & Sato, M. (2014). Geophysical assessment of the hydraulic property of the fracture systems around Lake Nasser-Egypt: In sight of polarimetric borehole radar. *NRIAG Journal of Astronomy and Geophysics, 3*(1), 7-17.

Mao, L., & Zhou, B. (2017). Simulation and analysis of conductively guided borehole radar wave. *IEEE Transactions on Geoscience and Remote Sensing, 55*(5), 2646-2657.

Maser, K. R., Scullion, T., & Briggs, R. C. (1991). Use of radar technology for pavement layer evaluation. *NASA STI/Recon Technical Report N, 93*, 21744.

Mateus, J., Saavedra, N., Carrillo, Z. C., & Mateus, D. (2007). Correlation development between indentation parameters and unaxial compressive strength for Colombian sandstones. *CT&F-Ciencia, Tecnología y Futuro*, *3*(3), 125-136.

Metsalu, T., & Vilo, J. (2015). ClustVis: a web tool for visualizing clustering of multivariate data using Principal Component Analysis and heatmap. *Nucleic acids research, 43*(W1), W566-W570.

Miorali, M., Slob, E., & Arts, R. (2011). A feasibility study of borehole radar as a permanent downhole sensor. *Geophysical Prospecting, 59*(1), 120-131.

Mishnaevsky, L. L. (1995). Physical mechanisms of hard rock fragmentation under mechanical loading: a review. *International journal of rock mechanics and mining & geomechanics abstracts*, *32*(8).

Monnier, S., & Kinnard, C. (2013). Internal structure and composition of a rock glacier in the Andes (upper Choapa valley, Chile) using borehole information and ground-penetrating radar. *Annals of Glaciology, 54*(64), 61-72.

Morte, M., & Hascakir, B. (2019). Characterization of complex permittivity for consolidated core samples by utilization of mixing rules. *Journal of Petroleum Science and Engineering, 181*, 106178.

Nakashima, Y., Zhou, H., & Sato, M. (2001). Estimation of groundwater level by GPR in an area with multiple ambiguous reflections. *Journal of applied geophysics, 47*(3-4), 241-249.

Narayanan, R. M., Hudson, S. G., & Kumke, C. J. (1998, May). Detection of rebar corrosion in bridge decks using statistical variance of radar reflected pulses. In *Proceedings of the Seventh International Conference on Ground-Penetrating Radar* (Vol. 98, pp. 27-30).

Neal, A. (2004). Ground-penetrating radar and its use in sedimentology: principles, problems and progress. *Earth-science reviews, 66*(3-4), 261-330

Neal, A., & Roberts, C. L. (2000). Applications of ground-penetrating radar (GPR) to sedimentological, geomorphological and geoarchaeological studies in coastal environments. *Geological Society, London, Special Publications, 175*(1), 139-171.

Nicolson, A. M., & Ross, G. F. (1970). Measurement of the intrinsic properties of materials by time-domain techniques. *IEEE Transactions on instrumentation and measurement, 19*(4), 377-382.Olhoeft, G. R. (1992, April). Geophysical Detection of Hydrocarewn and Organic Chemical Contamination. In *5th EEGS Symposium on the Application of Geophysics to Engineering and Environmental Problems* (pp. cp-210). European Association of Geoscientists & Engineers.

Oloumi, D., Pettersson, M. I., Mousavi, P., & Rambabu, K. (2015). Imaging of oil-well perforations using UWB synthetic aperture radar. *IEEE Transactions on Geoscience and remote sensing, 53*(8), 4510-4520.

Olsson, O., Falk, L., Forslund, O., Lundmark, L., & Sandberg, E. (1992). Borehole radar applied to the characterization of hydraulically conductive fracture zones in crystalline rock 1. *Geophysical prospecting, 40*(2), 109-142.

Osumi, N., & Ueno, K. (1988, August). Detection of buried plant. In *IEE Proceedings F (Communications, Radar and Signal Processing*) (Vol. 135, No. 4, pp. 330-342). IET Digital Library.

Paluszny, A., Zimmerman, R. W., Potjewyd, J., & Jarvis, B. (2014, June). Finite element-based numerical modeling of fracture propagation due to the plunge of a spherical indenter. In *48th US Rock Mechanics/Geomechanics Symposium*. OnePetro.

Parizad, A., & Shahbazi, K. (2016). Experimental investigation of the effects of SnO2 nanoparticles and KCl salt on a water base drilling fluid properties. *The Canadian Journal of Chemical Engineering, 94*(10), 1924-1938.

Patil, P. A., Gorek, M., Folberth, M., Hartmann, A., Forgang, S., Fulda, C., & Reinicke, K. M. (2010). Experimental study of electrical properties of oil-based mud in the frequency range from 1 to 100 MHz. *SPE Drilling & Completion, 25*(03), 390-390.

Pipan, M., Baradello, L., Forte, E., & Prizzon, A. (2000, April). GPR study of bedding planes, fractures, and cavities in limestone. In *Eighth International Conference on Ground Penetrating Radar* (Vol. 4084, pp. 682-687). SPIE.

Potyondy, D. O. (2017, June). Simulating perforation damage with a flat-jointed bonded-particle material. In *51st US Rock Mechanics/Geomechanics Symposium*. OnePetro.

Povey-White, S. (2021, October 5). Carbon coatings: What are their applications and how are they characterized? *Quorum Technologies Ltd.* Retrieved November 22, 2022, from https://www.quorumtech.com/2021/10/05/carbon-coatings-what-are-their-applications-and-how-are-they-characterized/

Puritch, E. and Buck, M. 2010: Mining and Economic Analysis Stog'er Tight Project Baie Verte Newfoundland. *Unpublished report Tenacity Cold Mining Company Limited*, 21 pages.

Quan, W. (April 23, 2021). *Material Characterization of Natural and Synthetic Rocks*. Master thesis, Memorial University of Newfoundland. Memorial University of Newfoundland.

Robert, A. (1998). Dielectric permittivity of concrete between 50 MHz and 1 GHz and GPR measurements for building materials evaluation. *Journal of applied geophysics, 40*(1-3), 89-94.

Robinson, D. A., & Friedman, S. P. (2003). A method for measuring the solid particle permittivity or electrical conductivity of rocks, sediments, and granular materials. *Journal of Geophysical Research: Solid Earth, 108*(B2).

Robinson, D. A., Binley, A., Crook, N., Day-Lewis, F. D., Ferré, T. P. A., Grauch, V. J. S., ... & Slater, L. (2008). Advancing process-based watershed hydrological research using near-surface geophysics: A vision for, and review of, electrical and magnetic geophysical methods. *Hydrological Processes: An International Journal, 22*(18), 3604-3635

Santarelli, F. J., Zaho, S., Burrafato, G., Zausa, F., & Giacca, D. (1996, March). Wellbore stability analysis made easy and practical. In *IADC/SPE drilling conference*. OnePetro.

Sato, M., & Takayama, T. (2007). A novel directional borehole radar system using optical electric field sensors. *IEEE Transactions on Geoscience and Remote Sensing, 45*(8), 2529-2535.

Schunnesson, H. (1996). Probing ahead of the face with percussive drilling. In *International Journal of Rock Mechanics and Mining Sciences and Geomechanics Abstracts* (Vol. 6, No. 33, p. 278A).

Seleznev, N. V., Fellah, K., Phillips, J., Zulkipli, S. N., & Fournie, B. (2019). Matrix permittivity measurements for rock powders. SPE Reservoir Evaluation & Engineering, 19(02), 214-225.

Serzu, M. H., Kozak, E. T., Lodha, G. S., Everitt, R. A., & Woodcock, D. R. (2004). Use of borehole radar techniques to characterize fractured granitic bedrock at AECL's Underground Research Laboratory. Journal of Applied Geophysics, 55(1-2), 137-150.

Shah, M. (2020). *Investigation of drilling performance and penetration mechanism using passive vibration assisted rotary drilling technology* (Doctoral dissertation, Memorial University of Newfoundland).

Shau, Y. H., Peacor, D. R., & Essene, E. J. (1990). Corrensite and mixed-layer chlorite/corrensite in metabasalt from northern Taiwan: TEM/AEM, EMPA, XRD, and optical studies. *Contributions to Mineralogy and Petrology*, *105*(2), 123-142.

Sheen, J. (2007). Amendment of cavity perturbation technique for loss tangent measurement at microwave frequencies. *Journal of applied physics, 102*(1), 014102.

Shihab, S., & Al-Nuaimy, W. (2005). Radius estimation for cylindrical objects detected by ground penetrating radar. Subsurface sensing technologies and applications, 6, 151-166.

Singh, T. N., Kainthola, A., & Venkatesh, A. (2012). Correlation between point load index and uniaxial compressive strength for different rock types. *Rock Mechanics and Rock Engineering, 45*(2), 259-264.

Swain, M. V., & Lawn, B. R. (1976, November). Indentation fracture in brittle rocks and glasses. In *International Journal of Rock Mechanics and Mining Sciences & Geomechanics Abstracts* (Vol. 13, No. 11, pp. 311-319). Pergamon.

Sylvester, P. J. (2012). Use of the mineral liberation analyzer (MLA) for mineralogical studies of sediments and sedimentary rocks. *Mineralogical Association of Canada Short Course, 42*, 1-16.

Szwedzicki, T. (1998). Indentation hardness testing of rock. *International Journal of Rock Mechanics and Mining Sciences*, *35*(6), 825-829.

Tan, X. C., Kou, S. Q., & Lindqvist, P. A. (1998). Application of the DDM and fracture mechanics model on the simulation of rock breakage by mechanical tools. *Engineering Geology*, *49*(3-4), 277-284.

Thiercelin, M., and J. Cook. "Failure mechanisms induced by indentation of porous rocks." In *The 29th US Symposium on Rock Mechanics (USRMS)*. One Petro, 1988.

Tosti, F., Patriarca, C., Slob, E., Benedetto, A., & Lambot, S. (2013). Clay content evaluation in soils through GPR signal processing. Journal of Applied Geophysics, 97, 69-80. Grote, K., Anger, C., Kelly, B., Hubbard, S., & Rubin, Y. (2010). Characterization of soil water content variability and soil texture using GPR groundwave techniques. *Journal of Environmental & Engineering Geophysics, 15*(3), 93-110.

Trickett, J. C., Stevenson, F., Vogt, D., Mason, I. M., Hargreaves, J. E., Eybers, H., ... & Meyering, M. (2000, April). Application of borehole radar to South Africa's ultradeep gold mining environment. In *Eighth International Conference on Ground Penetrating Radar* (Vol. 4084, pp. 676-681). SPIE.

Uboldi, V., Civolani, L., & Zausa, F. (1999, October). Rock strength measurements on cuttings as input data for optimizing drill bit selection. In *SPE Annual Technical Conference and Exhibition*. OnePetro.

Umar, S., Abdelmalik, A. A., & Sadiq, U. (2018). Synthesis and characterization of a potential bio-based dielectric fluid from neem oil seed. *Industrial Crops and Products*, *115*, 117-123.

van Dongen, K. W., van Waard, R., van der Baan, S., van den Berg, P. M., & Fokkema, J. T. (2002). A directional borehole radar system. *Subsurface Sensing Technologies and Applications, 3*(4), 327-346.

van Waard, R., van der Baan, S., & van Dongen, K. W. (2004, June). Experimental data of a directional borehole radar system for UXO detection. In *Proceedings of the Tenth International Conference on Grounds Penetrating Radar, 2004. GPR 2004*. (Vol. 1, pp. 225-228). IEEE.

Vogt, D. (2004, June). The effect of conductive borehole water on borehole radar. In *Proceedings of the Tenth International Conference on Grounds Penetrating Radar*, 2004. GPR 2004. (Vol. 1, pp. 217-220). IEEE.

Von Hippel, A. R. (Ed.). (1958). *Dielectric materials and applications*. Published jointly by the Technology Press of MIT and Wiley.

Waldron, R. A. (1960). Perturbation theory of resonant cavities. *Proceedings of the IEE-Part C: Monographs, 107*(12), 272-274.

Wang, W., Liu, S., Shen, X., & Zheng, W. (2021). 3D imaging algorithm of directional borehole radar based on root-MUSIC. *Remote Sensing, 13*(15), 2957.

Wänstedt, S., Carlsten, S., & Tirén, S. (2000). Borehole radar measurements aid structure geological interpretations. *Journal of Applied Geophysics*, *43*(2-4), 227-237.

Warren, C., Giannopoulos, A., & Giannakis, I. (2016). gprMax: Open source software to simulate electromagnetic wave propagation for Ground Penetrating Radar. *Computer Physics Communications, 209*, 163-170.

West, L. J., Rippin, D. M., Murray, T., Mader, H. M., & Hubbard, B. (2007). Dielectric permittivity measurements on ice cores: implications for interpretation of radar to yield glacial unfrozen water content. *Journal of Environmental & Engineering Geophysics, 12*(1), 37-45.

Wold, S., Esbensen, K., & Geladi, P. (1987). Principal component analysis. *Chemometrics and intelligent laboratory systems, 2*(1-3), 37-52.

Wrigley, C. W., Corke, H., Seetharaman, K., & Faubion, J. (Eds.). (2015). *Encyclopedia of food grains*. Academic Press.

Xiao, Y., Hurich, C., & Butt, S. D. (2018). Characterization of rotary-percussion drilling as a seismic-while-drilling source. *Journal of Applied Geophysics, 151*, 142-156.

Xu, Z. H., Wang, W. Y., Lin, P., Xiong, Y., Liu, Z. Y., & He, S. J. (2020). A parameter calibration method for PFC simulation: Development and a case study of limestone. *Geomechanics and Engineering*, 22(1), 97-108.

Xuefeng, L., Shibo, W., Shirong, G., Malekian, R., & Zhixiong, L. (2018). Investigation on the influence mechanism of rock brittleness on rock fragmentation and cutting performance by discrete element method. *Measurement*, *113*, 120-130.

Yagiz, S. (2009). Assessment of brittleness using rock strength and density with punch penetration test. *Tunnelling and Underground Space Technology*, *24*(1), 66-74.

Yang, S. Q., Huang, Y. H., Jing, H. W., & Liu, X. R. (2014). Discrete element modeling on fracture coalescence behavior of red sandstone containing two unparallel fissures under uniaxial compression. *Engineering Geology, 178*, 28-48.

Yang, X. X., & Qiao, W. G. (2018). Numerical investigation of the shear behavior of granite materials containing discontinuous joints by utilizing the flat-joint model. *Computers and Geotechnics*, *104*, 69-80.

Zaki, N. F. M., Ismail, M. A. M., Abidin, M. H. Z., & Madun, A. (2018, April). Geological Prediction Ahead of Tunnel Face in the Limestone Formation Tunnel using Multi-Modal Geophysical Surveys. In *Journal of Physics: Conference Series* (Vol. 995, No. 1, p. 012114). IOP Publishing.

Zhai, S. F., Cao, S. H., Gao, M., & Feng, Y. (2019). The effects of confining stress on rock fragmentation by TBM disc cutters. *Mathematical Problems in Engineering*, 2019.

Zhang, X. P., Ji, P. Q., Liu, Q. S., Liu, Q., Zhang, Q., & Peng, Z. H. (2018). Physical and numerical studies of rock fragmentation subject to wedge cutter indentation in the mixed ground. *Tunnelling and Underground Space Technology*, *71*, 354-365.

Zhang, Z., & Zhang, F. (2019, August). Three dimensional DEM simulation of rock indentation by flat-joint model. In *ARMA-CUPB Geothermal International Conference*. OnePetro.

Zhang, Zhen (2017) *Development and characterization of synthetic rock-like materials for drilling and* *geomechanics experiments.* Masters thesis, Memorial University of Newfoundland.

Zhen, Z., Xi, T. F., & Zheng, Y. F. (2015). Surface modification by natural biopolymer coatings on magnesium alloys for biomedical applications. In *Surface Modification of Magnesium and Its Alloys for Biomedical Applications* (pp. 301-333). Woodhead Publishing.

Zheng, Y., Wang, S., Feng, J., Ouyang, Z., & Li, X. (2005). Measurement of the complex permittivity of dry rocks and minerals: application of polythene dilution method and Lichtenecker's mixture formulae. *Geophysical Journal International*, 163(3), 1195-1202.

Zhou, W., Brossier, R., Operto, S., & Virieux, J. (2015). Full waveform inversion of diving & reflected waves for velocity model building with impedance inversion based on scale separation. *Geophysical Journal International, 202*(3), 1535-1554.

Zhou, X., Liu, D., Bu, H., Deng, L., Liu, H., Yuan, P., ... & Song, H. (2018). XRD-based quantitative analysis of clay minerals using reference intensity ratios, mineral intensity factors, Rietveld, and full pattern summation methods: A critical review. *Solid Earth Sciences, 3*(1), 16-29.

Zhou, Y., Wu, S., Jiao, J. and Zhang, X. (2011), “Research on mesomechanical parameters of rock and soil mass based on BP neural network”, *Rock Soil Mech., 32*(12), 3821-3826. https://doi.org/10.16285/j.rsm.2011.12.010.

Zhu, X., Liu, W., & He, X. (2017). The investigation of rock indentation simulation based on discrete element method. *KSCE Journal of Civil Engineering, 21*(4), 1201-1212.

Zou, J., Han, J., Zhang, T., & Yang, W. (2020). Experimental investigation and numerical analyses for red sandstone rock fragmentation. *International Journal of Geomechanics, 20*(12), 04020222.